Low-Mach Number Effects and Late-Time Treatment of Richtmyer-Meshkov and Rayleigh-Taylor Instabilities

Tommaso Oggian

Cranfield University
School of Engineering

Cranfield University

Tommaso Oggian

Low-Mach Number Effects and Late-Time Treatment of Richtmyer-Meshkov and Rayleigh-Taylor Instabilities

School of Engineering

Ph.D. Thesis

Accademic Year: 2010-2011

Supervisor: Professor Dimitris Drikakis

Abstract

The Richtmyer-Meshkov instability appears when the mixing between two fluids is triggered by the passage of a shock wave. It occurs in a range of different applications, such as astrophysics, inertial confinement fusion and supersonic combustion. Due to the extreme complexity of this phenomenon to be reproduced in a controlled environment, its study heavily relies on numerical methods. The presence of a shock wave as a triggering factor requires the use of compressible solvers, but once the shock has started the mixing process, the flow field freely decays and becomes incompressible.
The dynamics of this instability is still to be fully understood, especially its long-time behaviour. One of the hypothesis is that the mixing layer achieves a self-similar development at some point during its evolution. However, the low-Mach flow at late-times does not always allow to push compressible simulations so far in time and when it is possible, they become extremely demanding from a computational point of view. In fact, it is known that standard compressible methods fail when the Mach number of the numerical field is low and moreover they lose time-marching efficiency.
In this thesis, a new approach to the study of the very late-stage of the instability through the use of ILES is presented. The technique consists in starting the simulation by using the compressible model and to initialise the incompressible solver when the compressibility of the numerical field becomes sufficiently low. This allows to bypass the issues previously mentioned and study the very late-stage of the instability at reasonable computational costs. For this purpose, a new incompressible solver that employs high-resolution methods and which is based on the pressure-projection technique is developed. A number of different Riemann-solvers and reconstruction schemes are tested against experiments using the incompressible, impulsive version of RMI as test case. Two alternative methods are considered for triggering the mixing: velocity impulse and gravity pulse. Excellent results were obtained by using the former, whereas discrepancies were noticed when the latter was employed. Comparisons against numerical simulations in the literature allowed to identify the inviscid nature of the solver as the cause of these differences. However, this did not affect the capability of the solver to correctly compute multi-mode cases, in which viscosity is negligible. A preliminary study on the compressibility of the numerical field in time proved the feasibility of the numerical transition and a switching criterion based on the Mach number was established. The approach was therefore tested on a single-mode perturbation case and compared against compressible simulation. Very good agreement was found in the prediction of the growth of the instability and the analysis of the divergence of velocity of the numerical field proved the incompressibility of the solution generated by the hybrid solver. Finally, the approach was applied to multi-mode test cases. Excellent agreement with the theory was found. The turbulent kinetic energy presented a modified subinertial range and the growth exponent was very close to fully compressible predictions and experiments. Deeper results analysis showed against compressible simulations showed very good agreement on the flow physics. In fact, the instability settled to a self-similar regime with the same time-scale predicted by compressible analysis, but the simulated time reached by the hybrid solver was three times longer. The results obtained proved the applicability of the approach, opening to new possibilities for the study of the instability.

Acknowledgments

I have spent some of the best time of my life here at Cranfield University during these three years. I have met extraordinary people and I will try to thank as many of them as I can. Surely the ones who unquestionably left a stamp on this chapter of my life.

First I would like to thank Prof. Drikakis for having given me the opportunity of working here at Cranfield and for his guidance throughout these three years. His help and his experience have been fundamental for the success of this work. My gratitude goes also to David L. Youngs and Robin J.R. Williams for sharing their knowledge in numerical methods and flow physics and for supervising the progress of the project during our meetings once every three months. The financial support from AWE Plc throughout the course of this study is also greatly acknowledged.
After three years of sharing office together, discussing about numerical methods and dreaming about our lives, I have to give considerable thanks to Mathis Dahlqvist. I also thank Adrian Mihaiescu, Ben Thornber and Laszlo Konozsy for all the discussions and suggestions about CFD.
Nothing could have been the same during my staying at Cranfield if I had not met all my beloved fellows of our Flat-8 and my Italian crew during my first year: Romain, Carmen, Anne, Michaela, Elodie, Magnus and Anja, Sofia, Andrea, Francesca M., Francesco G., Francesco F. and Alessandro. Certainly the first three names of the list stand out, but all of you guys rock! Knowing you was a terrific gift and every day we have been living together is like a treasure to me. Unforgettable experience. A thank goes also to the Spanish crew: Juan-Carlos, Laura, Jesica, Pilar, Alfonso, Miguel and all the others. Partying with you guys was amazing. Tommaso, Francesca M., Paula, Nacho and Enzo surely deserve to be cited and thanked. Your company during my second year was certainly very precious. I cannot not remember a couple of persons involved in the basketball club over these years: Sandra and Fabio. To Fabio I am especially grateful since the friendship which still runs between us. A special thank goes to my current housemate Francesco B.. Apart from shared dinners and everything else, there is a very precise reason why I am infinitely grateful to him. How could I forget to thank Guido for all the philosophical and technical discussions we had? A special thank goes also to Daniele for all the coffee breaks we shared. Apart from new friends, Cranfield gave me also back my old friend Leonardo. That was a truly apreciated gift.
A special 'thank you' goes to all my family in Italy which has supported me during these years and which has always welcomed me with a lot of love whenever I went back home. Moreover, I would like to cite some of my friends back in Italy which surely played an important role in this adventure: Elio, Federico, Monica V. and Marco.
During the endless days of coding and debugging, a considerable amount of music went through my ears. Frank Zappa, Nile and Devin Townsend are surely the artists whose music captured me the most and helped me in these moments. Thank you guys.
Finally, a huge thank goes to my girlfriend Tanja for all the help, support and patience. Putting up with me has never been an easy task, especially during the last months of the PhD.

Tommaso Oggian

Faith is a firm blade of grass.

E.Caredda

Contents

List of Figures

List of Tables

List of Symbols

Latin symbols

a	perturbation amplitude
$\mathbf{A}$	matrix of the coefficients
$\widehat{\mathbf{A}}$	reduced $\mathbf{A}$
A_t	Atwood number
$\mathbf{b}$	vector of the known terms
c	speed of sound
C	CFL number
C_K	universal Kolmogorov constant
Dn_m	element of the n-th diagonal in the m-th row of $\mathbf{A}$
$D_{i,j,k}$	discrete divergence operator
e	internal energy
$E(k)$	energy spectrum function
$\mathbf{E}$, $\mathbf{F}$, $\mathbf{G}$	vectors of convective fluxes along x, y and z direction
$F(k)$	Fourier transform
$\mathbf{Fv}$	volume forces source term

$\widetilde{F}(x)$	Fourier inverse transform
$\mathbf{f}$	position vector
g	gravitational acceleration
$G_{i,j,k}$	discrete gradient operator
h_b, h_s	height of spikes and bubbles
k	wave number
K	turbulent kinetic energy
$L_{i,j,k}$	discrete Laplacian operator
M	Mach number
p	pressure
q	generic scalar quantity
Q	heat flux
r	residual
$\boldsymbol{r}$	residuals vector
$R_{i,j}$	correlation function
S	wave speed
$\overline{S}$	fictitious wave speed
t	time
T	temperature
$\mathbf{T}$	stress tensor
u, v, w	velocity compunents along x, y and z directions
Δu	velocity impulse
$\mathbf{u}$	velocity vector

$\mathbf{U}$	vector of conserved variables
v	volume
V_f	volume fraction
W	integral length of the mixing zone
Z	number of diagonals

Greek symbols

γ	ratio of specific heats
Γ	circulation
δ_D	Dirac impulse
Δ	difference
$\overline{\Delta}$	filter width
ϵ	error
$\epsilon_{i,j}$	strain rate tensor element
ε	dissipation rate
θ	Richtmyer-Meshkov instability growth exponent
Θ	molecular mixing fraction
κ	thermal conductivity
λ	eigenvalue
ν	kinematic viscosity
Ξ	mixing parameter
ρ	density
τ	time scale

$\tau_{i,j}$	stress tensor element
$\mathbf{\Phi}_{i,j}$	velocity-spectrum tensor
ϕ	potential function
$\mathbf{\Psi}_{i,j}$	compensated Kolmogorov spectrum function
ω	vorticity

Acronyms

BC	Boundary Condition
BiCGSTAB	Bi-Conjugate Gradients Stabilised
CB	Characteristic Based
CFD	Computational Fluid Dynamics
CFL	Courant-Friedrichs-Lewy
DNS	Direct Numerical Simulation
ENO	Essentially Non-Oscillatory
FD	Finite Differences
FV	Finite Volumes
GCI	Grid Convergence Index
HLL	Harten-Lax-Van Leer
HLLC	Harten-Lax-Van Leer Contact
H-L	Heavy-to-Light
ICF	Inertial Confinment Fusion
ILES	Implicit Large-Eddy Simulation
LES	Large-Eddy Simulation
LF	Lax-Friedrichs

L-H	Light-to-Heavy
M2	MUSCL second order
M3	MUSCL third order
M5	MUSCL fifth order
MM	Multi-Mode
MPI	Message Passing Interface
MUSCL	Monotone Upstream-centred Scheme for Conservation Laws
NS	Navier-Stokes
PLIF	Planar Laser-Induced Fluorescence
PP	Pressure-Projection
RANS	Reynolds Averaged Navier-Stokes
R&D	Research and Development
RK	Runge-Kutta
RMI	Richtmyer-Meshkov Instability
RTI	Rayleigh-Taylor Instability
RU	Rusanov
SGS	Sub-Grid Scale
SM	Single-Mode
SSP	Strong Stability Preserving
TKE	Turbulent Kinetic Energy
VIC	Vortex-In-Cell
W5	WENO fifth order
W9	WENO ninth order

WENO	Weighted Essentially Non-Oscillatory

Subscripts

0	initial value
i, j, k	cell-centred values
$i \pm \frac{1}{2}, j \pm \frac{1}{2}, k \pm \frac{1}{2}$	interface values
I	incompressible quantity
L	left quantity
min	minimum value of the quantity
R	right quantity

Superscripts

n	n-th time-step
$+$	post-shocked quantity
$'$	fluctuating component
$\overline{(.)}$	averaged quantity

Other symbols

ℓ	eddies length scale
$\mathcal{L}$	length scale
$\mathcal{N}$	number of elements of a given array
$\mathcal{U}$	mean velocity

1 Introduction

1.1 Turbulence and computational fluid dynamics

Scientists and philosophers have always built models which try to describe our world. As time has passed and new knowledge has been acquired, these representations of reality filtered by our mind have come through, renewed or revisited. Nevertheless, despite all the efforts made, the complexity of some phenomena still eludes our mental grasp, representing a real challenge to our intellects. This surely concerns a vast range of fields, but a single day does not pass without new gained knowledge. This thesis aims at bringing a small contribution to a very vast area which has always captured the attention of researchers since the ancient times: the fluid dynamics, i.e. the science which investigates how a fluid in motion behaves.
Although the first studies on fluids were carried out by Archimedes during the III century BC, this is a very important field of research still today, since fluids play an important role in our everyday lives. Knowing how a fluid behaves and how it interacts with the surrounding environment makes it possible to use it for our purposes, literally transforming our world and our lifestyle. Building waterworks, forecasting the weather and flying are just a few examples. Normally, before exploiting nature to our scopes and needs, the physics behind a certain phenomenon is supposed to be understood, but this field is so complex that, in the end, we are not completely sure about the very reason why the air moving around a wing makes an airplane fly.
The first word which scientists associate fluid dynamics with is 'turbulence': "The most important unsolved problem in classical physics" (L.R. Feynman, 1918-1988). This concept was firstly introduced by the work of Stokes (1851) and by the experimental observations of Reynolds (1883). Thanks to their studies, we know that when a fluid is flowing, it evolves in either one of two possible manners. At low speeds, the flow is smooth and it behaves like it is formed by foils that are sliding one over the other and which interact only by shear stress. On the contrary, when the velocity increases, the flow behaves chaotically, involving a broad range of both temporal and spatial scales, with a strong three dimensional pattern and a high amount of mixing. The former is called 'laminar flux' and it is portrayed on the left side of Figure 1.1, whereas the latter is called 'turbulent flux', visible on the right side of the same figure. The parameter that act as an indicator of the flow regime is the 'Reynolds number', which is derived

FIGURE 1.1: Transition to turbulence of the water flowing in a channel. Photography by J.M. Phelps (`http:www.flickr.com`).

from the dimensional analysis of the governing equations and which expresses the ratio of inertial to viscous force acting within the fluid:

$$Re = \frac{\text{Inertial force}}{\text{Viscous force}} = \frac{\mathcal{U}\mathcal{L}}{\nu}\,, \tag{1.1}$$

where $\mathcal{U}$ is the mean velocity of the flow, $\mathcal{L}$ is a characteristic linear dimension and ν is the kinematic viscosity. Although the turbulent regime is typical of high-Re flows, if we suppose to somehow move a fluid at such speed that the interactions within the media are dominated by inertial forces, turbulence does not manifest itself unless the flux is disturbed. Various are the means of triggering turbulent motion, e.g. by using an object or an obstacle to deviate a flow stream (Figure 1.1), but also by the interaction between two fluids flowing one over the other with different velocities (Kelvin-Helmholtz instability, Figure 1.2a) or, more ideally, by superposing a heavy fluid over a light fluid both of which are subjected to the gravity force (Rayleigh-Taylor instability, Figure 1.2b).

(a) 'Billow' clouds generated by Kelvin-Helmholtz instability (`http:www.moolf.com`).

(b) Revolved mushrooms generated by Rayleigh-Taylor instability. Photography by D. Jewitt (`https://picasaweb.google.com`).

FIGURE 1.2: Instabilities which trigger turbulence in nature.

In the past, the approaches to study the turbulence, and more in general fluid dynamics, were substantially two: mathematical analysis and experiments. Both the methods

have important constraints. Due to the complexity of the governing equations of fluids, the Navier-Stokes (NS) equations, an analytical solution in closed form can be found only for very simple cases which are too basic for industrial applications. On the other hand, the possibility of carrying out experiments is limited by the capability of reproducing the flow of interest in a controlled environment (wind, water or plasma tunnels). During the XX century, when the first computers started to appear, a third approach was born: the Computational Fluid-Dynamics (CFD). This new path for the study of the subject links the mathematical aspects with the experimental side of the matter, since it numerically solves the governing equations. Its great advantage lies on the fact that, in theory, it can be applied to all the possible flows. Although this method seems to overcome all the limitations typical of the analytical treatment and of the tests, a range of new issues arose. In fact, the use of computers and numbers brings about three main problems. The first is the passage from a continuous formulation of the equations to a discrete one, which automatically implies a loss of information due to the finite nature of numeric representation. Moreover, solving the model numerically requires a certain amount of operations between numbers which sometimes is so big that even modern computers cannot cope with it. Lastly, the 'perfect algorithm' for the computation of the solution does not exist and a variety of methods, with their pros and cons, have been created.

At present, CFD is still a very active field of research, where scientists are always trying to create better, more efficient algorithms and faster computers in order to reduce the effects of the issues above mentioned as much as possible and to allow numerical methods to be trusted more each day. Having at disposal reliable and robust algorithms for resolving the NS equations is of fundamental importance. Simulations allow to sensibly cut down costs and time for R&D process in industries and they also allow to study phenomena which are impossible to be replicated and/or measured in laboratories. In fact, another great advantage of CFD over the experiments is that there is no need to use invasive probes or sensors inside the numerical field and the resolution of the points of the domain where the flow variables are known is limited only by computational power and storage capability.

Turbulence plays a key role in CFD. The approaches available for solving the NS equations are divided into three distinct classes, which depend upon the way turbulence is taken into consideration. The 'Direct Numerical Simulation' (DNS) fully resolves the turbulent structures included in the domain. This is the most accurate and expensive method in terms of computational power because turbulence is formed by a vast range of temporal and spatial scales and the smallest detail needs to be captured. A much less demanding method is the 'Reynolds Averaged Navier-Stokes Simulation' (RANS). In this case, a mean flow field is computed and the effects of turbulence on the numerical domain are estimated by a 'turbulence model'. A solution in-between DNS and RANS, where the large scales of the turbulence are resolved and the small scales are modelled by a 'Sub-Grid Scale' (SGS) model, is called 'Large-Eddy Simulation' (LES). Over the past two decades, it has been proved that the use of SGS models can be avoided by carefully designing the numerics. It is in fact possible to embed some physical features in the construction of the numerical schemes, therefore obtaining an implicit modelling of the turbulence. The methods which use this strategy fall into the class of 'Implicit' LES (ILES).

1.2 The Richtmyer-Meshkov instability

Among the events which cause the appearance of turbulence, the Richtmyer-Meshkov Instability (RMI) is surely one of the most complex and less understood phenomena. RMI, which receives its name from the analytical and numerical work of Richtmyer (1960) and Meshkov (1969) respectively, occurs when a shock wave hits the interface between two different fluids, enhancing the mixing between them. It is closely related to the Rayleigh-Taylor instability (RTI) (Rayleigh, 1900; Taylor, 1950) and it is often referred as the impulsive or shock-induced RTI (Kull, 1991). RMI is of great interest in physics and fluid mechanics as it has been attributed as a source of turbulent mixing in man-made applications and natural events. In supernovae explosions, the instability is believed to occur when an outward shock wave generated by the collapsing core of the star hits the interface between the layer of helium and hydrogen. Arnett et al. (1989) noticed that the outer regions of the supernovae 1987A presented a higher mixing than expected and they attributed to RMI the cause of lack of stratification of the products (Figure 1.3a). In addition, Almgreen et al. (2006) showed how RMI, together with RTI, is the cause of the loss of spherical symmetry in the supernovae remnants. The instability is very important also to Inertial Confinement Fusion (ICF) (Lindl et al., 1992). Here, it appears between the ablated shell of the capsule containing deuterium-tritium fuel and the fuel itself. The ablation of the capsule surface is provoked by a laser and the resulting gas accelerates the fuel inwardly (Figure 1.4). RMI causes the mixing between the capsule material and the fuel within, diluting and cooling the fuel with a significant loss of compression and reaction efficiency. On the contrary, the instability enhances the mixing between fuel and oxidizer in scram-jet engines, improving the combustion process (Markstein, 1957; Yang et al., 1993).

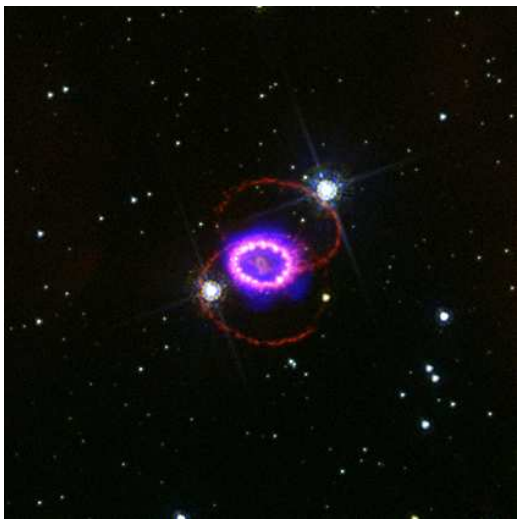

(a) Composite X-ray/optical picture of the Supernova 1987A (Zehekov et al., 2005).

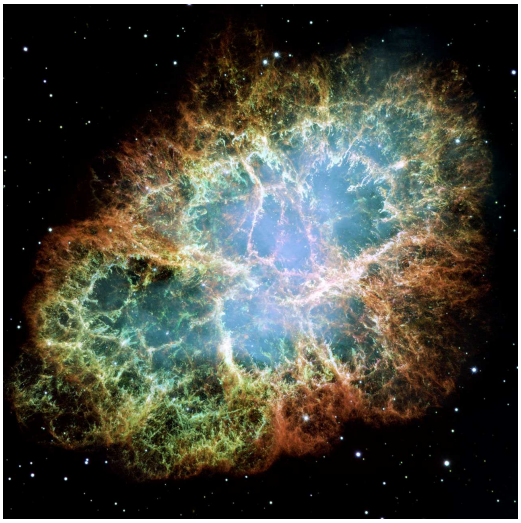

(b) Crab nebula (`http://www.spacetelescope.org`).

FIGURE 1.3: Astronomical events where RMI manifests.

The key point which allows RMI to manifest itself is that the interface between the fluids is never perfectly flat, but perturbations and protuberances are always present,

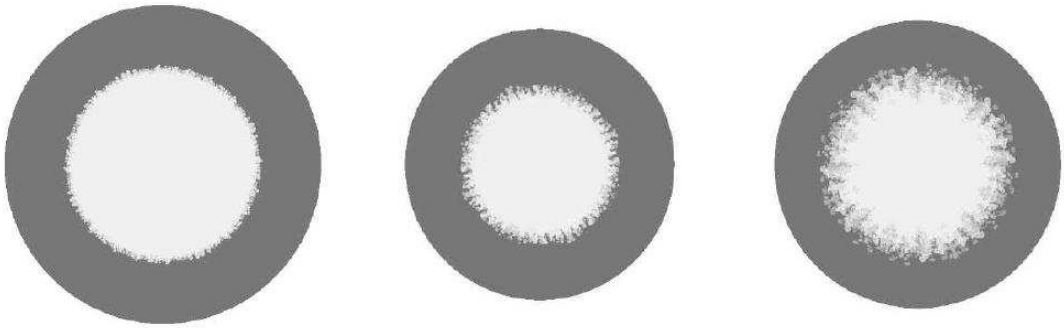

FIGURE 1.4: Numerical simulation of RMI at the interface between the ablated capsule material and nuclear fuel (Youngs and Williams, 2007).

even on a micro-scale level. Supposing the initial perturbation of the interface between two miscible fluids to be sinusoidal and extremely small, RMI, as shown in Figure 1.5, evolves through four phases (Brouillette, 2002). Initially, the incident shock wave impacts the interface and it bifurcates into a reflected and a transmitted wave, both of which pick up the disturbance and move away. The interface accelerated by the shock starts to grow linearly forming spikes and bubbles. Successively, spikes become mushroom-like and the growth rate of the instability decays with time. During the late-stage of the evolution, Kelvin-Helmholtz and Rayleigh-Taylor instabilities at the interface and three-dimensional effects become important, with the appearance of small-scale structures and turbulent mixing.
According to the two-dimensional compressible vorticity equation:

$$\rho \frac{D}{Dt}\left(\frac{\omega}{\rho}\right) = \frac{1}{\rho^2}\nabla\rho \times \nabla p\,, \tag{1.2}$$

where ρ is the density, ω is the vorticity and p is the pressure, the mechanism primarily involved in the process is the deposition of baroclinic vorticity[1] at the interface, which causes the increasing of the circulation in this area with time. In fact, the collision of the shock deposits clockwise vorticity on the right side of the perturbation and counterclockwise vorticity on the left side. Thus, an unstable sheet of vortex which leads to the deformation of the interface is created.

1.3 Compressible and incompressible flow models

Once RMI is triggered, it evolves through a number of phases which are characterized by different velocity ranges. At the beginning, the shock wave produces a high-speed motion flow field, which freely evolves towards zero-velocity with time. This fact brings issues in terms of models employed when RMI is numerically simulated.
Classical fluid mechanics rely on the very basic assumption that fluids are deformable

[1]Vorticity produced by the misalignment of the pressure and the density gradient, $\nabla\rho \times \nabla p \neq 0$. As shown in Figure 1.5(a), the shock wave is the sources of a pressure gradient and the interface is the source of a density gradient.

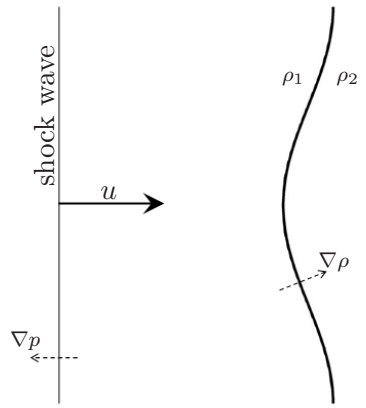

(a) First phase: the shock collides with the interface between two fluids of density ρ_1 and ρ_2 respectively.

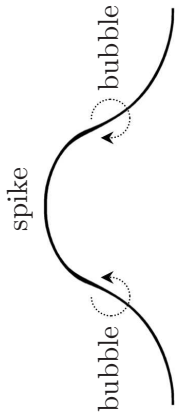

(b) Second phase: the baroclinic vorticity deposited at the interface causes the perturbation to grow linearly. Spikes and bubbles appear.

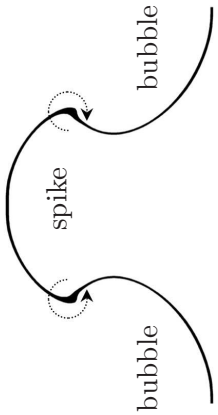

(c) Third phase: the circulation around the interface increases. Spikes and bubbles become mushroom-like.

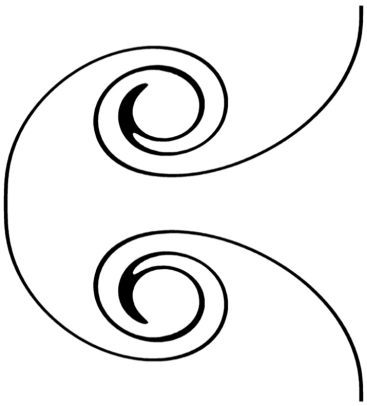

(d) Fourth phase: roll-ups on the sides of the mushroom and secondary instabilities start to manifest causing turbulent mixing.

FIGURE 1.5: Growth of Richtmyer-Meshkov instability.

and continuous media (Kundu and Cohen, 2008). This implies that the shape of a given control volume of fluid can be modified in various manners while it is flowing (compressed, stretched, etc). Nevertheless, in the fluid dynamics community a distinction is commonly made. Even though in reality a fluid in motion always carries within itself the effect of its compressibility, a flow field can be classified into two different categories depending on the ratio between its mean velocity and the corresponding speed of sound (Mach number, M), that is compressible or incompressible. Considering the

total-to-static relation for an isoentropic compression:

$$\frac{\rho_0}{\rho} = \left(1 + \frac{\gamma - 1}{2} M^2\right)^{\frac{1}{\gamma - 1}} , \tag{1.3}$$

where γ is the ratio of the specific heats, it is possible to find that for $0 \leq M \leq 0.32$, the ratio ρ_0/ρ decreases by approximately 5%. Applying the well-known rule of thumb which states that if a parameter varies by less than 5% then the variation is negligible, the incompressibility assumption is made for those fluxes which present $M < 0.3$. This threshold is commonly accepted, even though, from a strictly physical point of view, a flux characterized by $M = 0.29$ does not significantly differ from the same flux with $M = 0.31$. The incompressible flow model is a subset of the compressible model and the difference is that the density of an incompressible fluid remains constant, without changing neither in space nor in time. This distinction yields to two different sets of governing equations with different properties and which require different numerics for their resolution.
On the base of this distinction, it is possible to realise how RMI involves both the flow regimes: compressible at the early-stage and incompressible at late-time. In terms of modelling and numerical methods, this represents a real challenge. In fact, as shock waves are typical features of compressible flow fields, the use of such solvers would seem an automatic choice for RMI simulations. Nevertheless, as Volpe (1993) demonstrated, compressible methods fail when the Mach number of the flow is low, with the implication that the late-stage of RMI cannot be simulated consistently if no modifications to the solver are brought.

1.4 Shock-driven and impulsive RMI

The very first analytical study of the instability was carried out by Richtmyer (1960) under the fundamental assumption of incompressible flow, replacing the incident shock wave with an impulse of velocity applied to the interface. His study finds its roots in the work of Taylor (1950), who developed an expression for the growth of irregularities on the interface between fluids of different densities under the action of the gravity force, with the heavy fluid superposed over the light one:

$$\frac{d^2 a(t)}{dt^2} = k g(t) a(t) \frac{\rho_h - \rho_l}{\rho_h + \rho_l} . \tag{1.4}$$

Here, $a(t)$ is the length of the perturbation in time, k is the wavenumber of the perturbation, $g(t)$ is the gravity acceleration and the quantity:

$$A_t = \frac{\rho_h - \rho_l}{\rho_h + \rho_l} , \tag{1.5}$$

is called Atwood number. The subscript $(.)_q$, with $q = h, l$, indicates the heavy or the light fluid respectively. Richtmyer replaced the gravitational acceleration $g(t)$ in Equation (1.4) with an impulse $g = \Delta u \delta_D(t)$, where $\delta_D(t)$ is the Dirac function and

Δu is the increment of velocity induced by the incident shock wave. Substituting these terms and integrating the formula with respect to time, it yields to:

$$\frac{da(t)}{dt} = k\Delta u a_0 \frac{\rho_h - \rho_l}{\rho_h + \rho_l} \,, \tag{1.6}$$

with a_0 initial amplitude of the perturbation. This is known in the literature as Richtmyer's impulsive or linear model. If the post-shocked quantities A_t^+ and a_0^+ are used, Equation (1.6) correctly describes the early linear stage of the instability within a $5\% - 10\%$ of tolerance. Experiments have been found to be in excellent agreement with the Richtmyer's model. Grove et al. (1993) considered the interface between air and SF_6 for a weak shock ($M = 1.2$) and the growth rates measured during the experiments matched very well with the impulsive model. These results were confirmed also by Jones and Jacobs (1997). Moreover, Collins and Jacobs (2002) demonstrated that for a two-dimensional weak shock and for an Atwood number of 0.604, the amplitude of the perturbation grows linearly up to $ka(t) \approx 1$. This relation was also verified in the three-dimensional case by Chapman and Jacobs (2006) and in the case of strong driven shocks by Holmes et al. (1999).
Instead of looking at the instability strictly as it is observable in nature, the key feature of Richtmyer's work was the adoption of an alternative point of view. Considering RMI as an impulsive limit of RTI has repercussions also on the numerical simulations, offering a second modelling strategy which entails the use of the incompressible flow model. The main constraint in his work is represented by the assumption that the interface has a sinusoidal shape of constant wavelength (also referred to as 'Single-Mode', SM, perturbation) and it needs to be pointed out that this is definitely a simplified case of what it is possible to find in real events. Therefore, his theory is not applicable to more complex situations. In reality, the perturbation of the interface is always formed by a range of modes with different wavelengths ('Multi-Mode', MM, perturbation), which cause the interface to be very irregular, with protuberances of different amplitudes all of which produce a mushroom that interacts with the surrounding structures, hence making the instability much more complicated to be understood. Moreover, linear compressible flow analysis (Fraley, 1986) demonstrated that the incompressible assumption represents just an approximation to the compressible case. In fact, in the initial linear stage of RMI the velocity perturbation decays as $\sim e^{-k|x|}$ away from the interface in the incompressible assumption, whereas it decays more slowly in the compressible case: $\sim |x|^{3/2}$ for weak shocks and $\sim |x|^{1/2}$ for strong shocks. From a numerical point of view, the production of correct initial conditions for MM cases is possible for both compressible and incompressible simulations. In the former case, as it occurs in reality, the interface between the fluids is properly shaped so that the passage of the shock triggers the mixing process. On the other hand, for incompressible models the interface at the start is perfectly flat and the protuberances are emulated by a specifically computed velocity field. This difference in the initialisation introduces a level of uncertainty into the comparison between compressible and incompressible simulations, making the quantitative correspondence between the models dependent upon a scaling factor (Thornber et al., 2010). Up to the present, numerical simulations of MM-RMI rely entirely on compressible methods. In one of the first works published where the initial interface was formed by multiple wavelengths (Youngs, 1984), two-dimensional test cases were

presented. More recently, thanks to the increasing computational power, various authors used hydrodynamic codes to simulate three-dimensional MM-RMI (Youngs, 1991; Oron et al., 2001; Thornber et al., 2010). Due to the reasons previously mentioned, fully incompressible simulations have been much less employed than the compressible option and they have been used mainly for simpler SM test cases which are useful in code validation (Holmes et al., 1999; Mueschke et al., 2005b; Cotrell and Cook, 2007). To author's knowledge, the only multi-mode simulation with an incompressible numerical model was carried out by Youngs (1989) for a two-dimensional test case.
As it will be presented in more detail in the following chapter, the nonlinear dynamics of MM-RMI at late-times is still not fully understood. In fact, different models have been built and tested against numerical and experimental results in order to quantify the growth of the instability in time, but the range of values proposed by the models and found by simulations and experiments is very broad. Comparison of the numerical data against experimental results is uncertain as the generation of controlled MM initial condition in experiments is very difficult. Moreover, most of the simulations and experiments do not transit completely to a turbulent regime, therefore not allowing the study of the very late-time growth (Abarzhi, 2008).

1.5 Thesis objectives

The main aim of this thesis is to present a new numerical technique for the study of the flow physics underlying the Richtmyer-Meshkov instability at very late-times. This approach is intended to overcome all the inconvenients concerned with the use of compressible solvers for low-Mach number flows. In the literature it is possible to find several corrections to the compressible numerical model so that low-speed flows can be computed, but the technique here presented does not follow any of the previous paths which have been investigated so far. From a conceptual point of view it is much simpler, even though much more drastic than the solutions available. The main idea which underlies it is to employ the most appropriate numerical model depending on the situation of the field. The simulation starts with a compressible code which allows the shock wave to trigger the instability and at a precise moment during the simulation a literal switch to an incompressible solver is done and the compressible solution becomes the new initial condition. This allows to push the simulations to very late-times which have never been reached before with standard compressible simulations.
The framework used to achieve the objectives is Hirecom, a code developed within the Fluid Mechanics and Computational Science group (FMaCS) at Cranfield University which solves the governing equations with the ILES technique and which already comprised the compressible flow model. Therefore, in order to achieve the objectives, the code was provided of a new incompressible solver, which had to include the capability of running in parallel on computational clusters in order to take advantage of the speed-up of the simulations offered by these facilities. Message Passing Interface (MPI) calls were included so that parallel execution is allowed. All the three-dimensional simulations which are presented in the thesis were run on Cranfield's HPC facility Astral.

1.6 Summary of the content

The thesis commences with the review of turbulence and turbulent flows. Firstly, attention will be given to the Kolmogorov's hypotheses and to the spectrum of turbulent kinetic energy, which are fundamental in order to understand ILES methods. Successively the focus is moved towards the modifications to the spectrum needed for shock-induced turbulent mixing and to the theories which try to predict the growth of Richtmyer-Meshkov instability. Moreover, a quick presentation of the methods available in CFD to compute turbulence is also included.
Chapter 3 presents the mathematical and numerical models involved in this work. Godunov-type method and high-resolution schemes are discussed in the framework of compressible and incompressible simulations, with a detailed explanation of the new incompressible solver based on ILES technique and on the pressure-projection method.
Chapter 4 presents the numerical simulations on the incompressible, impulsive RMI. A variety of formulations for the numerical fluxes coming from the compressible methods and adapted for incompressible flows are tested and the results are compared against experiments and numerical simulations available in the literature.
Chapter 5 presents the applications of the hybrid compressible-incompressible solver. The first part is dedicated to the single-mode perturbation, whereas the second part is concerned with the more complex multi-mode perturbation and with the very-long time behaviour of the instability predicted by the new technique. Differences against the compressible analyses are highlighted and investigated.
Chapter 6 concludes the thesis with the final considerations and suggestions for future research.

1.7 Publications

The following journal paper inspired by this thesis has been submitted for publication to Communications on Computational Physics.

- T.Oggian, D.Drikakis, D.L. Youngs and R.J.R. Williams, 'Numerical uncertainty in incompressible, variable-density flows due to reconstruction schemes and Riemann solvers'.

The following journal papers are currently being written. Their submission is planned to happen soon.

- T. Oggian, D. Drikakis, D.L. Youngs and R.J.R. Williams. 'A hybrid compressible-incompressible solver for multi-component flows'. For Journal of Computational Physics.

Moreover, the the results in this work were accepted to be presented at the 13^{th} International Workshop on the Physics of Compressible Turbulent Mixing. 16-20 July 2012, Woburn (UK).

2

Notes on turbulence

Synopsis

In order to understand the evolution of the Richtmyer-Meshkov instability, it is of fundamental importance to introduce some aspects regarding turbulence. This chapter reviews some of the concepts of turbulent flows, providing the basis for interpreting the results obtained from the numerical simulations. After a brief introduction on the physical features of turbulence, the concept of 'energy cascade' and the Kolmogorov's theory is explained in general lines, with the derivation of the energy spectrum for homogeneous and isotropic turbulence. Since RMI does not fall into this category of fluxes, the corrected spectrum for shock-driven flows is reported and explained. Successively, the focus is moved onto the theories which have been developed to predict the growth of the instability, with a revision of the approaches and methodologies available at present in the literature. It needs to be pointed out that every time that RMI is implicated in this chapter, it is intended to refer to the multi-mode RMI (see §1.2), since the evolution of single-mode RMI follows different principles and furthermore it mainly represents a simplified numerical/experimental test case rather than a real physical event. Since turbulent mixing is the very final product of RMI, the problem of numerically simulating turbulent flows and the methodologies at disposal of CFD are introduced and explained in the context of Kolmogorov's theory. A very brief review of DNS, RANS and LES methods is done in order to introduce the ILES technique employed for the simulations presented in this thesis. Since the broadness and the complexity of the topics touched in this chapter, more detailed information can be found in classical textbooks such as Pope (2000), Mathieu and Scott (2000), Davidson (2004), Drikakis and Rider (2004), Toro (2009) and in the citations throughout the chapter.

2.1 Physical features of turbulence

Even though turbulence is part of our everyday life, it can be very difficult to try to find a universal and clear definition for it. For instance, we can directly observe turbulence when we look at smoke coming out from a chimney or at the water falling from a waterfall. Otherwise, we can just observe just its consequences, like a flag fluttering in the wind. Surely, there are some physical features which belong to turbulence:

- *Turbulence is present at high Reynolds number.* Increasing the Re of a flow, the inertial forces become more and more important than the viscous forces, causing the instability of the laminar boundary layer and the transition to turbulence. Experimentally, turbulence is detected when the flow variables fluctuate randomly and jerkily around a mean value.

- *Turbulence is an apparently random process.* Lorentz (1963) showed that some types of system of non-linear equations, such as the NS equations, are strongly dependent on initial conditions and even a small change in these can lead to a completely different evolution of the flow field, thus causing an apparent randomness. Due to their great complexity, turbulent flows are substantially unpredictable in detail and only their statistical properties can be reproduced.

- *Turbulence involves a broad range of scales.* Vortices of various sizes that interact among each other and with the entire flow field are formed, leading to the coexistence of different spatial and temporal scales. Small scales hide inside large scales, producing again new scales which evolve with their own properties in space and time, creating very complex flow structures.

- *Turbulence is a self-sustained phenomenon leading to energy dissipation.* Once the turbulent motion is started, it initiates a process of continuous formation of new vortices. The large scales feed the small scales which are responsible for the dissipation of the kinetic energy through viscous interactions according to the 'energy cascade' principle.

- *Turbulence is intrinsically three-dimensional.*

In order to describe the mechanics of turbulence, the concept of 'energy cascade' was firstly introduced by Richardson (1922). The main idea is summarised by the author in this short poem:

> Big whorls have little whorls,
> which feed on their velocity;
> and little whorls have lesser whorls,
> and so on to viscosity.

He proposed that the kinetic energy enters the turbulence at the largest scales of motion through a production mechanism. This energy is then transferred to smaller and smaller scales through an inviscid process until it is finally dissipated by viscous actions at the smallest scales.

2.1.1 Kolmogorov's theory

Kolmogorov (1941) was the first who used the ideas of Richardson to investigate further into turbulence, extending and quantifying the picture. His work represents a scientific milestone for understanding this complex phenomenon which still challenges the intellects of the scientific community.
For a given high Reynolds number flow with characteristic velocity $\mathcal{U}$ and lengthscale $\mathcal{L}$, the eddies present in the flow field are characterised by a size ℓ, velocity $u(\ell)$, time scale $\tau(\ell) = \ell/u(\ell)$ and Reynolds number $Re = u(\ell)\ell/\nu$. Assigning to the largest structures a characteristic length ℓ_l and characteristic velocity $u_l(\ell_l)$, where $\ell_l \sim \mathcal{L}$ and $u_l \sim \mathcal{U}$, it is possible to state that the rate of transfer of energy u_l^2 contained in these structures scales as $u_l^2/\tau_l = u_l^3/\ell_l$. Therefore, in free-shear flows and according with experiments, it is possible to assume that the dissipation rate, ε, has order of magnitude:

$$\varepsilon \sim \frac{u_l^3}{\ell_l} \,. \tag{2.1}$$

Initially, Kolmogorov considered the small scales in the flow, formulating his hypothesis of local isotropy:

> At sufficiently high Reynolds number, the small scale turbulent motions ($\ell \ll \ell_l$) are statistically isotropic.

Considering ℓ_E as the characteristic length which separates the small isotropic scales from the large anisotropic eddies, with $\ell_E \approx \ell_l/6$, the direct consequence of this statement is that under a certain lengthscale ℓ_E, all the information about the geometry of the larger eddies are lost and the statistics of the small scales motions are substantially universal and similar in every high Reynolds number flow. Kolmogorov focused on these lengthscales, formulating his first similarity hypothesis:

> In every turbulent flow at sufficiently high Reynolds number, the statistics of the small scale motions ($\ell < \ell_E$) have a universal form that is uniquely determined by the viscosity ν and the dissipation rate ε.

This introduces the concept of 'universal equilibrium range' for the eddies of scale $\ell < \ell_E$. Using ν and ε, it is possible to form unique length, velocity and time scales by which these eddies are characterised:

$$\ell_\eta \equiv (\nu^3/\varepsilon)^{1/4} \,, \tag{2.2}$$

$$u_\eta \equiv (\nu\varepsilon)^{1/4} \,, \tag{2.3}$$

$$\tau_\eta \equiv (\nu/\varepsilon)^{1/2} \,. \tag{2.4}$$

These scales, known as 'scales of Kolmogorov', are the smallest present in the flow field. Consistently with the energy cascade concept, the kinetic energy is transmitted from the large to the Kolmogorov's scales, where the energy is dissipated by the viscous forces. The Reynolds number of the Kolmogorov's scale Re_η is in fact of the order of

unity. Proceeding further with his work, Kolmogorov noticed that, inside the universal equilibrium range, a distinction could still be made. It exists in the flow a range of scales ℓ which is significantly smaller than ℓ_l and yet very large if compared to ℓ_η. This implies that the Reynolds number of these scales is not small enough for the viscosity to be effective. Kolmogorov summarised this further distinction in his second similarity hypothesis:

> In every turbulent flow at sufficiently high Reynolds number, the statistics of the motion scale ℓ in the range of $\ell_\eta \ll \ell \ll \ell_E$ have a universal form that is uniquely determined by ε, independent of ν.

Defining a new lengthscale $\ell_I \approx 60\ell_\eta$, the universal equilibrium range can be split into two subranges: the 'dissipation range' ($\ell < \ell_I$) and the 'inertial subrange' ($\ell_I < \ell < \ell_E$). According to the second similarity hypothesis, in the former the viscosity plays a significant role, whereas in the latter, the motion is dominated by inertial forces with a characteristic velocity and time scales determined uniquely by ε:

$$u(\ell) = (\varepsilon\ell)^{1/3} , \tag{2.5}$$

$$\tau(\ell) = (\ell^2/\varepsilon)^{1/3} . \tag{2.6}$$

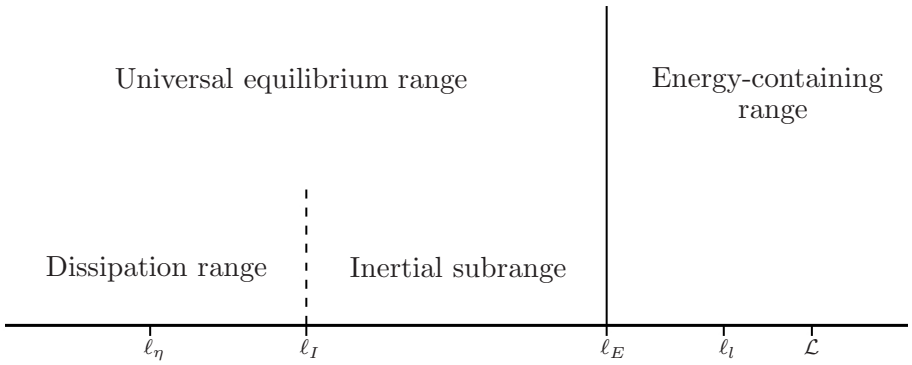

FIGURE 2.1: Size and ranges of turbulent structures according to Kolmogorov (1941) at high Reynolds number.

It needs to be pointed out that Kolmogorov's theory is valid on a global level. In fact, the energy cascade from the large to the small scales is true overall, but it does happen locally that smaller scales feed large scales. This is known as 'backscatter' and it occurs, for instance, in rarefaction waves.

2.1.2 Self-similarity

In the framework of turbulent flows and Richtmyer-Meshkov instability, it is very important to introduce the concept of self-similarity, which is widely used to develop theories that try to predict the growth of the instability in time.
A self-similar object is an object which is exactly or approximately similar to a part of itself. Clear visual illustrations of this idea are given by some of the famous operas of M.C. Escher (1898-1972), two of which are reported in Figure 2.2.

(a) Smaller and Smaller, 1956. (b) The Limit of the Circle IV, 1960.

FIGURE 2.2: Visual examples of self-similarity by M.C. Escher (1898-1972).

In mathematical terms, self-similarity can be defined by considering a quantity $q(x, y)$, where x and y are independent variables (Pope, 2000). Supposing that $\ell_q(x)$ and $\ell_y(x)$ are the characteristic spatial scales of $q(x, y)$ and y respectively, it is possible to define the scaled variables as:

$$\tilde{y} \equiv \frac{y}{\ell_y(x)} \,, \tag{2.7}$$

$$\tilde{q}(\tilde{y}, x) \equiv \frac{q(x, y)}{\ell_q(x)} \,. \tag{2.8}$$

$q(x, y)$ is defined self-similar if a function $f(\tilde{y})$ exists such that $f(\tilde{y}) = \tilde{q}(\tilde{y}, x)$. Hence, in this case, $q(x, y)$ can be expressed as function of $\ell_q(x)$, $\ell_y(x)$ and $f(\tilde{y})$. Self-similarity can also be found in time and not just in space, that is the same flow field at two instants in time fits the same function by good choice of the scaling parameters.

2.2 The turbulent kinetic energy spectrum

The turbulent kinetic energy spectrum is fundamental to the study of the mechanisms which govern turbulence in terms of energy cascade process. Moreover, it is very important also for the analysis of the behaviour of numerical methods, since it provides information on the distribution of the energy among the eddies of different sizes.
Unmasking the turbulence from the governing equations can be done by using the Reynolds decomposition, which splits the flow variables into the sum of a mean and of a fluctuating component. For example, the x-velocity component u becomes:

$$u = \overline{U} + u' \,, \tag{2.9}$$

where the average term $\overline{U}$ is defined as:

$$\overline{U} = \int_{-\infty}^{+\infty} UP(U)dU \ , \tag{2.10}$$

with $P(U)$ the probability distribution of U which satisfies the identity:

$$\int_{-\infty}^{+\infty} P(U)dU = 1 \ . \tag{2.11}$$

The main concept for the calculation of the energy spectrum is to use the Fourier transform:

$$\widetilde{F}(k) = \frac{1}{2\pi} \int_{-\infty}^{+\infty} F(x)e^{-ikx}dx \ , \tag{2.12}$$

and its inverse:

$$F(x) = \int_{-\infty}^{+\infty} \widetilde{F}(k)e^{ikx}dk \ , \tag{2.13}$$

in order to transform the fluctuating component of the velocity u', v' and w' into sinusoidal components and study the distribution of Turbulent Kinetic Eenergy (TKE):

$$K = \frac{1}{2}(\overline{u'u'} + \overline{v'v'} + \overline{w'w'}) \ , \tag{2.14}$$

among the different wavelengths, which represent the different scales of turbulent motion. During the derivation of the spectrum, only the main points will be highlighted in order to give the reader an idea of the process. More detailed information can be found in the textbooks cited in the synopsis of this chapter.
The correlation function for the velocity fluctuations is defined as:

$$R_{i,j}(\mathbf{x}, \mathbf{x}^*, t) = \overline{u_i'(\mathbf{x}, t)u_j'(\mathbf{x}^*, t)} \ . \tag{2.15}$$

Considering the turbulence homogeneous[1] and isotropic[2], the statistical properties of u do not vary under an arbitrary and constant displacement in space, therefore it is possible to write:

$$R_{i,j}(\mathbf{r}, t) = \overline{u_i'(\mathbf{x}, t)u_j'(\mathbf{x}^*, t)} \ . \tag{2.16}$$

[1]The turbulence is locally homogeneous in the domain Ω, if for every fixed N and $\mathbf{x}_n$ (with $n = 1, ..., N$), the N-point probability density function f_N is independent of $\mathbf{x}_0$ and $\mathbf{u}(\mathbf{x}_0, t)$ (Pope, 2000).

[2]The turbulence is locally isotropic in the domain Ω, if it is locally homogeneous and if in addition to the probability density function f_N is invariant with respect to the rotations and reflections of the coordinate axes (Pope, 2000).

where $\mathbf{r} = \mathbf{x} - \mathbf{x}^*$ and with the property that:

$$R_{i,j}(\mathbf{r}, t) \to 0 \,, \quad \text{as} \quad \mathbf{r} \to \infty \,. \tag{2.17}$$

Using the correlation function $R_{i,j}$, the velocity-spectrum tensor is defined as the Fourier transform of the velocity fluctuations correlation function:

$$\mathbf{\Phi}_{i,j}(\mathbf{k}, t) = \frac{1}{(2\pi)^3} \iiint_{-\infty}^{+\infty} R_{i,j}(\mathbf{r}, t) e^{-i\mathbf{k}\cdot\mathbf{r}} d\mathbf{r} \,, \tag{2.18}$$

with the inverse function defined as:

$$R_{i,j}(\mathbf{r}, t) = \iiint_{-\infty}^{+\infty} \mathbf{\Phi}_{i,j}(\mathbf{k}, t) e^{i\mathbf{k}\cdot\mathbf{r}} d\mathbf{k} \,, \tag{2.19}$$

The final step to derive the spectrum is to express the turbulent kinetic energy as an integral over $\mathbf{k}$ and this can be done by setting $\mathbf{r} = 0$ and $i = j$:

$$\frac{1}{2}\overline{u_i' u_i'} = \frac{1}{2} R_{i,i}(0, t) = \frac{1}{2} \iiint_{-\infty}^{+\infty} \mathbf{\Phi}_{i,i}(\mathbf{k}, t) d\mathbf{k} \,. \tag{2.20}$$

Thus, the function $\mathbf{\Phi}_{i,i}(\mathbf{k}, t)/2$ can be interpreted as the distribution of turbulent kinetic energy over the different wavenumbers. Considering the turbulence homogeneous and isotropic allows to make some simplifications and to remove all the directional information from $\mathbf{\Phi}_{i,i}(\mathbf{k}, t)$, thus introducing the energy spectrum function:

$$E(k, t) = \frac{1}{2} \iiint_{-\infty}^{+\infty} \mathbf{\Phi}_{i,i}(\mathbf{k}, t) \delta(|\mathbf{k}| - k) d\mathbf{k} \,, \tag{2.21}$$

2.2.1 The Kolmogorov spectrum

The consequences of the Kolmogorov hypotheses, §2.1.1, on the shape of the energy spectrum are very important. Recalling that the lengthscales to which Kolmogorov's work refer are the ones included in the universal equilibrium range ($\ell < \ell_E$), in the Fourier space these correspond to the wavenumbers $k > k_E$, where $k_E \equiv 2\pi/\ell_E$. According to the first similarity hypothesis, the energy spectrum function has a universal form for all the wavenumbers $k > k_E$. Using ε and k in order to non-dimensionalise $E(k)$, the energy spectrum function becomes:

$$E(k) = \varepsilon^{2/3} k^{-5/3} \mathbf{\Psi}(k\eta) \,, \tag{2.22}$$

where $\mathbf{\Psi}(k\eta)$ is the 'compensated Kolmogorov spectrum function'. Considering also the second similarity hypothesis, which states that the form of the scales included in the subinertial range are only determined by ε and taking into account that the viscosity ν enters in Equation (2.22) only through $\mathbf{\Psi}(k\eta)$, the argument of the compensated

Kolmogorov spectrum function tends to zero, with the consequence that $\mathbf{\Psi}(k\eta)$ tends to a constant C_k:

$$E(k) = C_k \varepsilon^{2/3} k^{-5/3} \, . \tag{2.23}$$

This is the famous Kolmogorov subinertial range spectrum, which states that the turbulent kinetic energy in the subinertial range decays as $k^{-5/3}$. The universal Kolmogorov constant was determined experimentally to be $C_k = 0.53 \pm 0.055$ (Sreenivasan, 1995).

2.2.2 The spectrum for shock-induced turbulent mixing

Kolmogorov's spectrum is valid under very precise assumptions, i.e. homogeneous and isotropic turbulence and sufficiently high Reynolds number. Under these hypotheses, the $k^{-5/3}$ decay of the turbulent kinetic energy is obtained. In the study of Richtmyer-Meshkov instability, the flow along the direction of the propagation of the shock cannot be considered neither homogeneous nor isotropic, therefore a modification of the Kolmogorov's theory is required. The recent work of Zhou (2001) aimed at extending the classic Kolmogorov phenomenology to fluxes where external time scales, i.e. other time scales than the original nonlinear cascade time scale, are present and play a significant role in the evolution of the turbulence in the flow field (Kraichnan, 1965). In particular, his work regarded gravity- (RTI) and shock- (RMI) driven fluxes.
The starting point for Zhou's extention is to observe that the energy transfer within the subinertial range is not affected even if the energy-containing scales are excited. Using the dimensional analysis, it is therefore possible to find a universal expression for the rate of energy dissipation:

$$\varepsilon = C^2 \tau_T(k) k^4 E^2(k) \, , \tag{2.24}$$

where C is a constant and τ_T is the time scale for the decay of the transfer function correlation, which is responsible for introducing turbulent spectral transfer. The following step is to take into consideration the physical case of interest. RMI flow can be considered isotropic and homogeneous only in the directions different from the one along which the shock propagates, therefore the wavenumber k is defined as $k = \sqrt{k_y^2 + k_z^2}$ (with x the direction of shock propagation). From Richtmyer's impulsive model Equation (1.6), it is possible to derive the external time scale associated to the instability:

$$\tau_{RMI}(k) = \frac{1}{k A_t \Delta u} \, . \tag{2.25}$$

An expression for the energy spectrum function in the subinertial range which takes into account the driven nature of the flow is found by replacing τ_{RMI} into Equation (2.24), yielding to:

$$E(k, x) = C_{RMI} k^{-3/2} \sqrt{A_t \Delta u \varepsilon(x)} \, , \tag{2.26}$$

with C_{RMI} constant. As it is possible to notice, the decaying of turbulent kinetic energy for shock-driven turbulent mixing is $k^{-3/2}$, which is slightly different from the classical Kolmogorov $k^{-5/3}$ scaling valid for homogeneous and isotropic turbulence. It needs to

be pointed out that Equation (2.26) is valid only if a quasi-stationary fully-turbulent state is achieved.
Considering that in the turbulent flow generated by RMI both the characteristic time scale associated to RMI itself, τ_{RMI}, and the local dynamic time scale which is normally present when no external excitations are introduced in the flux, τ_n, coexist, it needs to be taken into consideration that these two components will assume a different weight during the evolution of the flow field in time. Assuming therefore the governing time scale τ_T as a contribution of both τ_n and τ_{RMI}:

$$\tau_T = \left[\frac{1}{\tau_n(k,x)} + \frac{1}{\tau_{RMI}(k)} \right]^{-1} , \tag{2.27}$$

and substituting it in Equation (2.24), Zhou found the generalised formulation for the subinertial range energy spectrum:

$$E(k,x) = C^{-4/3}[Z_0(k,x)]^2 \varepsilon(x)^{2/3} k^{-5/3} , \tag{2.28}$$

where:

$$Z_0(k,x) = C^{2/3} \frac{1}{\tau_{RMI}[\varepsilon(x)k^2]^{1/3}} , \tag{2.29}$$

represents the influence of the shock-driven nature of the flow. When $\tau_{RMI} \ll \tau_n$, the spectrum will assume the form Equation (2.26), whereas long after the passage of the shock, the turbulent flow will tend again to the Kolmogorov's $k^{-5/3}$ decay, that is of incompressible freely decaying homogeneous and isotropic turbulence.

2.3 Growth of shock-induced mixing layer

The study of the growth of Richtmyer-Meshkov instability in time is a relatively young field (Abarzhi, 2008). In this paragraph, the methodologies presented in the literature will be reviewed in order to provide a solid background for the interpretation of the numerical results presented in this thesis. Several approaches based on different ideas have been considered so far in order to study the shock-induced turbulent mixing:

- Self-similarity hypothesis;
- Potential flow models;
- Momentum-drag formulation.

2.3.1 Self-similar growth

Self-similar growth of RMI at late-stage is an hypethesis that has been widely assumed in order to create models which attempt to predict the late-time growth of the instability. These can be split into two main categories. The first one assumes that the instability has gone past the initial phase and that the modes present in the initial problem have already saturated, thus developing in a fully turbulent manner. On the other hand, the second class considers that the initial modes are not yet linearly saturated and that the evolution is still governed by the longer wavelengths present in the field.

Fully developed turbulence

Barenblatt et al. (1983) was the first to use the concept of temporal self-similarity in order to derive a model for the propagation of turbulence from an instantaneous plane source. The starting point of his theory was to consider an infinite space filled with incompressible, homogeneous fluid. At $t = 0$, the flow field presents a turbulent layer that expands for $t > 0$. The flow is shearless, therefore no turbulent energy is generated, but it is dissipated into heat and it decays in time. Supposing that the layer expands along the x-direction and that $\mathcal{U}$ and $\mathcal{L}$ are the characteristic velocity and characteristic lengthscale respectively, the equation of turbulent kinetic energy variation is governed by turbulent energy turbulent diffusion together with turbulent energy dissipation into heat and it is of the form:

$$\frac{\partial K}{\partial t} = -\frac{\partial(\overline{Ku' + p'u'/\rho})}{\partial x} - \varepsilon \, . \tag{2.30}$$

Introducing the turbulent energy diffusion coefficient K_q and using the dimensional analysis, it is possible to find:

$$K_q = l\sqrt{K} \, , \tag{2.31}$$

$$\varepsilon = \frac{cK^{3/2}}{\mathcal{L}} \, , \tag{2.32}$$

with c constant of the model. Substituting Equation (2.31) and Equation (2.32) into Equation (2.30) and supposing that the function which assigns the initial distribution of turbulent kinetic energy is symmetric with respect to the middle plane of the mixing layer and null outside the interval $-a \leq x \leq a$, where $2a$ is the initial depth of the mixing layer, Barenblatt obtained the following Cauchy problem for the case considered:

$$\left.\begin{aligned} &\frac{\partial K}{\partial t} = \frac{\partial[cW(t)\sqrt{K}]}{\partial x}\frac{\partial K}{\partial x} - \frac{bK^{3/2}}{cW(t)} \, , \\ &K(x,0) = \frac{Q}{a}u(\tau) \, , \end{aligned}\right\} \tag{2.33}$$

where Q is the bulk intensity of the instantaneous turbulence source, $u(\tau)$ is an even dimensionless function of its dimensionless argument τ, b and c are constants and $W(t)$ is the length of the turbulent mixing layer. Supposing the limiting case of no dissipation ($b = 0$), The solution of the problem Equation (2.33) is found by dimensional analysis:

$$K = Q^{2/3}t^{-2/3}f(\xi) \, , \quad \xi = \frac{x}{Q^{1/3}t^{2/3}} \, , \quad W(t) = \xi_0(c)Q^{1/3}t^{2/3} \, , \tag{2.34}$$

with $\xi_0(c)$ positive constant. In case of presence of dissipation, Barenblatt found the asymptotic solution:

$$K = A^2t^{-2\mu}\Phi\left(\frac{x}{At^\theta}\right) \, , \quad W = At^\theta \, . \tag{2.35}$$

where A is a coefficient of the model and $\theta = 1-\mu$. In both the cases, $W(t)$ evolves as t^θ and the conclusion of the author was that the growth exponent θ is $2/3$ if no dissipation

is present. On the other hand, if $b \neq 0$, the solution is not completely self-similar and it is a function of b, with $\theta < 2/3$.
Gauthier and Bonnet (1990) calibrated the k-ε turbulence model against shock-tube experiments in order to analyse the growth of the instability. Analysing the diffusion term of the turbulent kinetic energy equation and assuming self-similar growth, they found $W \propto t^{1/3}$, in line with Barenblatt's work when dissipation is considered.
Youngs (1994) applied self-similarity considerations by starting from the Kolmogorov process and the scaling law of the dissipation rate Equation (2.1) in order to formulate the following model equations:

$$\begin{aligned} &\text{kinetic energy dissipation:} && \frac{d}{dt}(\mathcal{L}\mathcal{U}^2) = -a\mathcal{U}^3 \ , \\ &\text{growth of the mixing layer:} && \frac{dW}{dt} = \mathcal{U} \ , \\ &\text{lengthscale:} && \mathcal{L} = bW + c\lambda_{min} \ , \end{aligned} \tag{2.36}$$

where a, b and c are model constants and $\lambda_{\min}$ is the shortest wavelength included in the perturbed interface. For initial values $W = \mathcal{U} = 0$, the growth of the mixing layer is:

$$\frac{W}{\lambda_{\min}} = A\left[\left(1 + \frac{\mathcal{U}_0 t}{pA\lambda_{\min}}\right)^{\theta} - 1\right] \tag{2.37}$$

Here, A and p are constants of the model. Consistently with Barenblatt's outcome, Youngs predicts an exponential growth for the instability: $W(t) \propto t^{\theta}$, but he also showed the dependency of the growth of $W(t)$ from the initial conditions through $\mathcal{U}_0$. The value of the growth exponent θ were found to be $\theta = 2/3$ in case of no dissipation or $\theta < 2/3$ otherwise, again in perfect agreement with Barenblatt's work. Another investigation which produced an outcome in line with Barenblatt and Youngs's results was conducted by Ramshaw (1998), who used a Lagrangian formulation for the energy to obtain an equation for the evolution of the mixing layer. For low Reynolds number, a different value for the growth exponent was found by Huang and Leonard (1994), who obtained $\theta = 1/4$ by applying Saffman (1967) hypothesis, which bounds the integral moments of vorticity distribution for the large scales. Zhou (2001) assumed a turbulent kinetic energy spectrum of the form:

$$E(k,x) = \begin{cases} a(x)k^m & \text{if} \quad k < k_{\text{peak}} \\ C^{-4/3}[Z_0(k,x)]^2\varepsilon(x)^{2/3}k^{-5/3} & \text{if} \quad k > k_{\text{peak}} \end{cases} \ , \tag{2.38}$$

in order to derive a turbulence model and consequently an estimation for θ. Depending on the slope m of the energy-containing range of the spectrum, the author proposed 2/3, 5/8 and 7/12 as possible values for the growth exponent assuming $m = 1$, 2 and 4 respectively. The upper bound value agrees with the analysis of Barenblatt et al. (1983) and Youngs (1994) previously mentioned. A study based on analogies with weakly anisotropic turbulence was proposed by Clark and Zhou (2006) with the result that the θ was found to be included between 2/7 and 2/5. More recently, Llor (2006) investigated the behaviour of a freely decaying slab of turbulence with respect to the

invariance of angular momentum. The author showed that for self-similar decay the kinetic energy decays as t^{-n}, where n depends on the range of wave numbers involved in the problem. Using the impulsive field (Saffman and Meiron, 1989) as initial condition, he found that for $n = 4/3$ and $n = 10/7$ the exponent θ assumes the value of $1/3$ and $2/7$ respectively. Poujade and Peybernes (2010) found a similar range of value using the foliated turbulent spectra analysis: $1/4 \leq \theta \leq 2/7$.

Just-saturated mode

Just-saturated mode analysis has been much less looked at than the fully saturated assumption and it was firstly taken into consideration by Dimonte et al. (1995). The authors considered the amplitudes of the just-saturated mode as:

$$a \approx \frac{C_R}{k} \,, \tag{2.39}$$

where C_R is of order 1. Considering that the modes grow linearly up to this amplitude according to Richtmyer's model, substituting Equation (2.39) in Equation (1.6) and considering the mixing layer $W = 2a$, the authors proposed the following equation to predict the growth of the instability:

$$\frac{d[W(t)^2]}{dt} = 4C_R A_t \Delta u W_0 \,, \tag{2.40}$$

which has solution:

$$W(t) \approx [W_0^2 + 4C_R A_t \Delta u (t - t_0)]^{1/2} \,, \tag{2.41}$$

This result predicts the exponent $\theta = 1/2$, in line with the results presented for the fully saturated turbulent mixing layer. Assuming a power-spectrum for the initial perturbation of the form $P(k) = Ck^m$ and from dimensional considerations, Youngs (2004) found:

$$W(t) \approx (C^{1/2} A_t \Delta u t)^\theta \,. \tag{2.42}$$

with $\theta = 2/(m + 5)$. This result confirms what was previously found by Inogamov (1999). Since it was found that $\theta = 0.24$ for initial short wavelength perturbations, Youngs also showed the dependency of the growth of the mixing layer from the initial condition in the case that $2/(m + 5) < 0.24$, i.e. $m < 3.3$. Inogamov (2006) explored the case of initial perturbation with a power-spectrum which is constant at low wavenumbers. Examining the difference in velocity fluctuations at a given length scale, the author obtained the following equation for the growth of the mixing layer:

$$\frac{dW(t)}{dt} \propto \frac{u'_{\lambda_i} \lambda_i^2}{W^2} \tag{2.43}$$

where λ_i is the characteristic average perturbation length, u'_{λ_i} the relative velocity fluctuation. Inogamov's model has solution $W \propto t^{1/3}$ for three-dimensional cases, which is again in line with the results obtained with the fully-saturated modes approach.

2.3.2 Potential flow models

A different point of view to study the late-stage of RMI is to use the so-called potential flow models, which look at the evolution of the mixing layer as a competition between bubbles $(.)_b$ and spikes $(.)_s$ of different sizes and velocities, assuming $W = W_b + W_s$ and assuming two separate growth exponents $W_b \propto t^{\theta_b}$, $W_s \propto t^{\theta_s}$. This approach is often referred in the literature as Layzer-type model since Layzer (1955) was the first to propose this approach. The author considered a SM-RMI test case, assuming irrotational ($\nabla \times \mathbf{u} = 0$), potential ($\mathbf{u} = -\nabla\phi$) and incompressible ($\nabla^2\phi = 0$) flow, therefore seeking a solution which satisfies the Bernoulli's equation in cylindrical coordinates:

$$\frac{\partial \phi}{\partial t} - \frac{1}{2}\left(\frac{\partial \phi}{\partial x} + \frac{\partial \phi}{\partial r}\right) - gx = a(t) \,, \tag{2.44}$$

with x axial coordinate, r radial coordinate and a arbitrary function. The main outcome from this method is that the asymptotic velocity to which the bubbles tend scales as $1/t$, resulting in a logarithmic growth of the turbulent mixing layer for multi-mode cases. Using this approach, Alon et al. (1995) employed the potential flow model by Hecht et al. (1994) in order to compute the growth exponent of bubbles and spikes for a two-dimensional case. The authors estimated that $\theta_b \approx 0.4$ for a range of Atwood numbers and they found that the relation $\theta_s/\theta_b \approx 1 + A_t^+$ well fits the spikes penetration. Oron et al. (2001) proposed sensibly lower values $\theta_b \approx 0.24$ and $\theta_s \approx 0.3$ for three-dimensional case.

2.3.3 Momentum-drag models

The third class of models which try to describe the growth of RMI at late time is the momentum-drag models (Youngs, 1991). This method comes from Youngs' analytical work carried out for the Rayleigh-Taylor instability, which looks at the evolution of the mixing zone as governed by a balance of inertia, buoyancy and Newtonian drag forces:

$$\left[(\rho_1 + \kappa\rho_2)\frac{du_i}{dt} - \beta(\rho_2 - \rho_1)g\right] \mathrm{V} = -C\rho_i u_i^2 \mathrm{S} \,, \tag{2.45}$$

where V is the volume, S is the cross-section of the volume, β is the buoyancy coefficient, C is the drag coefficient, κ is the coefficient of added mass, u_i, with $i = 1, 2$, is defined as dW_i/dt and where the subscripts $(.)_i$ with $i = 1, 2$ indicates the heavy and the light fluid. Adapting the model for impulsive acceleration without gravity (Dimonte and Schneider, 1996) leads to:

$$\frac{du_i}{dt} = -C\frac{\rho_i}{\rho_1 + \rho_2}\frac{u_i^2}{L_i} \,, \tag{2.46}$$

with L_i longitudinal scale of the mixing zone. Once again, this model yields to an exponential growth of the mixing layer $W \propto t^\theta$, with the coefficient analytically defined:

$$\theta = \frac{1}{1 + C\dfrac{\rho_i}{\rho_1 + \rho_2}} \,. \tag{2.47}$$

2.3.4 Experiments and numerical simulations

Obtaining reliable data from experiments where the perturbation at the interface is formed by a range of modes with different wavelengths is not a straightforward task. Youngs (1994) showed how the development of RMI is affected by the initial conditions through Equation (2.37), therefore the generation of an interface with well-defined properties is vital for the production of reliable data. Significant breakthough on RMI experiments were achieved in two occasions. First, Castilla and Redondo (1993) adopted a new solution in order to generate the impulse which triggers the instability, therefore allowing to produce data for incompressible simulations. Instead of using the classic shock-tube, the authors impulsively accelerated a box containing the fluids by allowing it to fall onto a cushioned surface. Later, Jacobs and Sheeley (1996) perfected the technique by using coil springs instead of cushions. The other important contribution on experimental RMI was given by Jones and Jacobs (1997) concerning the formation of the interface between the fluids in shock-tubes. The authors found a way of generating the interface without using any solid membrane. The technique employed up to that moment entailed the use of a solid membrane to separate the fluids and the main drawback was that the membrane was shredded by the passage of the shock and the remnants were being transported in the flow field, heavily affecting the results of the experiment and not allowing any proper comparison with numerical simulations.
Dimonte (1999) used the falling box technique to conduct some tests on RMI, obtaining a range of values with a trend which can be summarised by:

$$\theta_s = \theta_b \left(\frac{\rho_h}{\rho_l} \right)^{0.22 \pm 0.05} , \tag{2.48}$$

for a range of Atwood numbers between 1.15 and 0.96. Dimonte and Schneider (2000) successivly confirmed the results giving an exponent for the formula (2.48) of 0.21 ± 0.05. Studying separately the evolution of bubbles and spikes, the authors found that θ_s is substantially independent from the Atwood number and it assumes a value of 0.25 ± 0.05, whereas the spikes exponent has a very similar value as θ_b only for $A_t < 0.8$. For $0.9 < A_t < 0.96$ in fact, θ_s drastically increases from 0.35 to 0.85, indicating that the experiment self-similar growth is not achieved. A possible explanation is given by Thornber et al. (2010) who, using numerical simulations, showed how for high Atwood number ($A_t = 0.9$) the self-similar regime is achieved later in time in comparison with cases with lower A_t.
Detailed numerical simulations of the late-time behaviour of RMI were presented only recently by Thornber et al. (2010). The authors used two multi-mode perturbations with different power spectra and combinations of fluids with different Atwood number in order to investigate the influence of initial conditions in the growth on the instability. When the interface is characterised by a constant power spectrum of a combination of narrowband wavenumbers, $\theta \approx 0.235$ ($A_t = 0.5$) and $\theta \approx 0.264$ ($A_t = 0.9$) were computed, therefore in agreement with Dimonte and Schneider (2000). On the other hand, $\theta \approx 0.62$ was found in the case that the interface is formed by a broadband of modes with a power spectrum proportional to k^{-2}, which is close to the upper bound limit calculated by theoretical analysis presented in §2.3.1.

2.4 Numerical approaches for simulating turbulent flows

Correctly capturing the turbulence is the main concern in CFD. The broadness of temporal and spatial scales involved in the fluxes puts a very serious requirement on the computational power needed for the calculations. There are three main approaches for simulating flows and they are characterised by how the turbulence is taken into account:

- *Direct Numerical Simulation* (DNS). The turbulence is computed directly from the governing equations;
- *Reynolds-Averaged Navier-Stokes Simulation* (RANS). All the turbulent scales are modeled by using a 'turbulence model';
- *Large-Eddy Simulation* (LES). It represents a compromise between DNS and RANS since only the large scales of the flows are resolved, whereas the remaining scales are modeled by using a 'Sub-Grid Scale' (SGS) model.

2.4.1 Direct Numerical Simulation

DNS is the most demanding method in terms of computational costs. Resolving the whole turbulent spectrum implies the use of a grid with spacing $\Delta x, \Delta y, \Delta x < \ell_\eta$ in order to capture the scales of Kolmogorov. Recalling the scaling laws for ε Equation (2.1) and ℓ_η Equation (2.2), it is possible to estimate the scaling factor of the number of cells necessary for fully resolving the turbulence inside the numerical domain. For a three-dimensional grid, the estimation is (Pope, 2000):

$$N_{xyz} > Re^{9/4} \,. \tag{2.49}$$

Moreover, the unsteady nature of turbulence requires the equations to be solved in time and, likewise the spatial discretisation, the Kolmogorov scales determine the time-step size Δt. Considering that for stability of the computational process, it is not possible to allow a particle to move more than one cell during a single time-step, the number of time-steps required is:

$$N_t \sim \frac{T}{\Delta t} \sim \frac{\mathcal{L}}{\ell_\eta} \sim Re^{3/4} \,. \tag{2.50}$$

where T is the total time of the simulation. Therefore, the scaling of the CPU time can be estimated as $N_t N_{xyz}$. Considering a flux with a modest Reynolds number of 10^4, the amount of CPU hours needed on a Gflop machine would be on the order of magnitude of 10^3. In engineering, flows typically present Reynolds numbers higher that 10^6, which means that DNS of such flows are unfeasible even for the state-of-the-art computational cluster[3]. These relations are valid for free-shear flows but the scaling factor becomes much 'worse' for flows where the combustion process is involved. In fact, the reaction time is faster than τ_η, with the consequence that an even finer grid and a higher number of time-steps are required.

[3] At the moment when this thesis is written, the most powerful computational facility is the GPUs cluster Tianhe-1A in the National Supercomputing Centre in Tianjin (China) with 2.566 Pflops of computational power (`www.top500.org`).

2.4.2 Reynolds-Averaged Navier-Stokes Simulation

The RANS technique uses the Reynolds decomposition in order to split the mean and the turbulent component of the flow-field from the governing equations. Considering $\mathbf{U}$ the vector of the flow variables, the split is given by:

$$\mathbf{U}(\mathbf{x},t) = \overline{\mathbf{U}}(\mathbf{x}) + \mathbf{u}'(\mathbf{x},t) \,, \tag{2.51}$$

where the average operator $\overline{(.)}$ refers to the time average:

$$\overline{\mathbf{U}}(\mathbf{x}) = \lim_{T\to\infty} \frac{1}{T} \int_{t}^{t+T} \mathbf{U}(\mathbf{x},t)dt \,. \tag{2.52}$$

Applying the decomposition to the governing equations, it is possible to obtain a new set of equations for the mean flow-field which present an extra-term if compared to the original NS equation, that is the correlation of the fluctuating velocities $-\overline{\rho u_i' u_j'}$, or the 'Reynolds stress tensor'. This term represents the influence of the turbulence on the mean field and it needs to be estimated by a 'turbulence model' in order to close the system (Wilcox, 2006). The estimation of the Reynolds stresses does not follow a unique way and, at present, a vast range of empirical or semi-empirical turbulence models, tailored for specific flows, are available in the literature (e.g. k-ε, k-ω, RSM, etc). The situation complicates further considering that many coefficients can be included in the models and that they need to be estimated by means of experiments and/or DNS. All these factors of uncertainty in the art of turbulence modelling make the RANS technique the least refined among the three types of simulations. Nevertheless, the low computational load which it requires make this method the most widely used in industries. In fact, even though all the imprecision carried by turbulence models, it is possible to obtain a good estimation of the flow variables and their trends are almost always correctly captured.

2.4.3 Large-Eddy Simulation

The last approach to the computation of turbulence lies in between the computationally costly DNS and the low accurate RANS. That is the Large-Eddy Simulation, where only the larger scales of turbulence are resolved by filtering the velocity in the governing equations, whereas the remaining ones are modeled. In order to derive the equations for LES, it is necessary to define a filtering operation for the flow variables:

$$\widehat{\mathbf{U}}(\mathbf{x}) = \iiint_{\Omega} \mathbf{U}(\mathbf{x}')G(\mathbf{x}',\mathbf{x},\overline{\Delta})d\mathbf{x}' \,, \tag{2.53}$$

where $G(\mathbf{x}',\mathbf{x},\overline{\Delta})$ is the filtering function and $\overline{\Delta}$ is the filter width. The higher the width of the filter, the more scales are removed from the velocity field. The main function of G is that of providing the dissipation for the unresolved scales and keeping the solution stable. Filtering the governing equations by using Equation (2.53) yields to the appearance of the extra-term $\tau_{ij}^{SGS} = \widehat{u_i u_j} - \hat{u}_i \hat{u}_j$ which, like in the RANS formulation, needs to be estimated in order to close the system. This additional term

represents the 'Sub-Grid Scale' (SGS) stresses and its weight on the system is directly linked to the choice of $\overline{\Delta}$. In fact, increasing the size of the filter implies that the range of scales which are modeled is wider. Hence, the weight of the subgrid stresses in the equations is higher.
Form a general point of view, SGS models can be diveded into two classes: structural and functional models. The former category attempts to directly calculate the subgrid scale stresses from the filtered field and it is the most complex between the two. A simpler approach is represented by the latter class of models, which are often referred to as 'eddy viscosity models' as they recover the effect of the unresolved scales through the use of a forcing term which is supposed to provide energy dissipation at a physically correct rate. Historically, the first eddy viscosity model is the Smagorinsky-Lilly model (Smagorinsky, 1963), developed for high-Re[4], incompressible flows. Decomposing the subgrid shear stresses as follows:

$$\tau_{ij}^{SGS} = \tau_{ij}^{r} + \frac{2}{3} K_r \delta_{i,j} \ , \tag{2.54}$$

where τ_{ij}^{r} is the anisotropic residual-stress tensor and K_r is the residual kinetic energy (Pope, 2000), the Smagorinsky model assumes that:

$$\tau_{i,j}^{r} = -2\nu_t \overline{S}_{i,j} \ . \tag{2.55}$$

Here, $\overline{S}_{i,j}$ is the filtered rate-of-strain tensor and the coefficient of proportionality $\nu_t = \nu_t(\mathbf{x}, t)$ is the eddy viscosity of the unresolved motions:

$$\nu_t = \ell_S^2 \overline{\mathcal{S}} = (C_S \overline{\Delta})^2 \overline{\mathcal{S}} \ , \tag{2.56}$$

where ℓ_S is the Smagorinsky length scale, $\overline{\mathcal{S}} = (2\overline{S}_{i,j}\overline{S}_{i,j})^{1/2}$ is the characteristic filtered rate-of-strain and C_S is the Smagorinsky constant, which is taken to be proportional to the filter width.
As for turbulence models, there is not a universal filter which can resolve all the flows and also subgrid modelling can be considered an art. For instance, the Smagorinsky model needs to be adeguately modified when a very large or a very small size of the filter is employed since Equation (2.56) is valid when $\overline{\Delta}$ is taken inside the subinertial range. For the same reason, the model fails also in the viscous near-wall region.
LES is mainly used for incompressible applications, since there are only a few models which can capture shock-waves. Similarly to RANS, as it is possibel to notice from Equation (2.56), also SGS models present empirical coefficients which need to be determined and it was shown that their optimum choice is not only problem-dependent but also grid-dependent (Geurts, 2003).
Thanks to the continuous increase of computational power and to the parallel-processing, LES approach is starting to be used also for industrial problems and it is believed to be in common use within the next 5-10 years (Fureby, 2008).

[4] A Re sufficiently high to satisfy Kolmogorov's hypotheses (see §2.1.1).

Implicit LES

A particular class of LES is that of Implicit LES (ILES). The term 'implicit' indicates that no explicit subgrid model is employed to solve the governing equations and the dissipation necessary for keeping the solution stable is produced by the numerical schemes themselves. This is made possible by the use of Riemann-solvers (Toro, 2009) and high-resolution methods (Drikakis and Rider, 2004; Grinstein et al., 2007). Classical LES use SGS filters which are artfully constructed in order to produce results which are consistent with the theory. This means that some constraints to the solutions are imposed through the use of the filter to 'drive' the calculations towards a precise outcome, i.e. the solution has to be consistent with the Kolmogorov's spectrum. In ILES, this process is overturned. Firstly, the formulation of the governing equation solved are not the filtered equations for LES, but the original Euler equations, like in DNS. Secondly, the numerical schemes used for the purpose are built in such a way that it takes into account the physical aspects, thus imposing physically realisable behaviour of the results. High-resolution methods are intrinsically nonlinear and not strictly dissipative. This means that the energy backscatter is taken into account during the computation of the solution. Contrarily to the classical LES, in ILES the production of results which are in line with the Kolmogorov's spectrum is a consequence of the design of the numerics. Embedding the physics in the numerics presents both advantages and disadvantages. The possibility of avoiding the use of filters and of obtaining good results even on coarse grids are surely advantages, but the main drawback is that it is not possible to know exactly how the numerics behave in terms of turbulence computation and it is not possible to have a direct control on the solution. The success of implicit modelling of turbulence has been widely proven for many different applications (Margolin and Rider, 2002; Drikakis, 2003; Bagabir and Drikakis, 2004; Drikakis et al., 2009) and the simulations which are presented in the next chapters fall into this category. A deeper insight into high-resolution methods for compressible and incompressible flows is left to the following chapter.

3
Numerical methods

Synopsis

Numerical simulations of fluids in motion imply the use of computers/HPC facilities in order to solve the Navier-Stokes equations. Specialised softwares implement algorithms which compute the numerical solutions of the governing equations with the appropriate initial and boundary conditions depending on the case of interest. The achievements of this project were made possible by the use of Hirecom, a code entirely developed by Cranfield's Fluid Mechanics and Computational Science group which is written in Fortran90/95 and which makes use of MPI libraries for parallel computation. Throughout the project, a great amount of coding was done in order to give the code a new incompressible solver based on the ILES techniques. This chapter presents the numerical schemes which were used for simulating the Richtmyer-Meshkov instability. The first part introduces the governing equations, the Riemann-problem and the numerics used for solving compressible flows. These techniques were already available in the code at the start of the project. Successively, the new improvements carried out for this thesis are introduced. The pressure-projection technique is presented in the framework of ILES with an insight on incompressible Riemann solvers and a detailed explanation of the solution procedure for the elliptic equation for the pressure is also included.

3.1 The governing equations

The governing equations of a fluid in motion, i.e. the Navier-Stokes equations or Euler equations for inviscid fluids, are derived from very basic physical considerations.

- Mass can neither be created nor destroyed, or *principle of mass conservation*:

$$\frac{\partial \rho}{\partial t} + \nabla \cdot (\rho \mathbf{u}) = 0 \,, \tag{3.1}$$

  where $\mathbf{u}$ is the vector of the cartesian velocity components (u, v, w);

- Force equals the rate of change of momentum in time (Newton's second law), or *principle of momentum conservation*:

$$\frac{\partial \rho \mathbf{u}}{\partial t} + \nabla \cdot (\rho \mathbf{u} \otimes \mathbf{u}) = \nabla \cdot \mathbf{T} + \mathbf{F_v} \,. \tag{3.2}$$

  where $\mathbf{T} = \tau_{i,j}$ is the stress tensor and $\mathbf{F_v}$ is a source terms which represents the volume forces such as gravity;

- Energy increases as work and heat are added to the system (first law of thermodynamics), or *principle of energy conservation*:

$$\frac{\partial \rho E}{\partial t} + \nabla \cdot (\rho \mathbf{u} E + p\mathbf{u}) = \nabla \cdot Q + \nabla \cdot (\mathbf{T}\mathbf{u}) \,, \tag{3.3}$$

  where $Q = \kappa \nabla T$ is the heat flux, with κ and T thermal conductivity and temperature respectively, and E is the total energy per unit volume:

$$E = \rho e + \frac{1}{2}\rho(u^2 + v^2 + w^2) \,. \tag{3.4}$$

  Here, e specific internal energy.

Considering a Newtonian fluid[1], Stokes (1845) related the elements of the stress tenson $\tau_{i,j}$ to the elements of the strain rate tensor $\epsilon_{i,j}$ through the following deformation law:

$$\tau_{i,j} = -\left(p + \frac{2}{3}\mu \nabla \cdot \mathbf{u}\right)\delta_{i,j} + 2\mu\epsilon_{i,j} \,, \tag{3.5}$$

where μ is the coefficient of viscosity and

$$\epsilon_{i,j} = \frac{1}{2}\left(\frac{\partial u_i}{\partial x_j} + \frac{\partial u_j}{\partial x_i}\right) \,. \tag{3.6}$$

[1] A newtonian fluid is a fluid which respects the three postulates of Stokes (1845): 1) The fluid is continuous and $\tau_{i,j}$ is a linear function of $\epsilon_{i,j}$; 2) The fluid is isotropic; 3) If the fluid is at rest, the deformation law is reduced to the hydrostatic pressure $\tau_{i,j} = -p\delta_{i,j}$, where $\delta_{i,j}$ is the Kronecker delta function.

Substituting the stress relations (3.5) into the momentum and energy equations (3.2), (3.3) and specialising the result for inviscid fluids ($\mu = 0$), it is possible to obtain the Euler equations, which in conservative form can be written:

$$\frac{\partial \mathbf{U}}{\partial t} + \frac{\partial \mathbf{E}}{\partial x} + \frac{\partial \mathbf{F}}{\partial y} + \frac{\partial \mathbf{G}}{\partial z} = 0 \,, \tag{3.7}$$

where:

$$\begin{cases} \mathbf{U} = (\rho, \rho u, \rho v, \rho w, E)^{\mathrm{T}} \\ \mathbf{E} = \mathbf{E}(\mathbf{U}) = (\rho u, \rho u^2 + p, \rho uv, \rho uw, (E+p)u)^{\mathrm{T}} \\ \mathbf{F} = \mathbf{F}(\mathbf{U}) = (\rho v, \rho uv, \rho v^2 + p, \rho vw, (E+p)v)^{\mathrm{T}} \\ \mathbf{G} = \mathbf{G}(\mathbf{U}) = (\rho w, \rho uw, \rho vw, \rho w^2 + p, (E+p)w)^{\mathrm{T}} \end{cases} . \tag{3.8}$$

The system of equations is closed by the equation of state for ideal gases:

$$p = \rho e(\gamma - 1) \tag{3.9}$$

where γ is the ratio of the specific heats. The nature of the Euler equations is strongly non-linear and the system is of hyperbolic type.

3.1.1 The incompressible limit

If the fluid is assumed to be of constant density both in space and time, then ρ can be taken out from the differential operators of the continuity equation (3.1), thus obtaining the divergence-free constraint which characterises an incompressible fluid:

$$\nabla \cdot \mathbf{u} = 0 \,. \tag{3.10}$$

Substituting Equation (3.10) into the deformation law (3.5) and then again Equation (3.5) into (3.2), the incompressible limit of the Euler equations is obtained:

$$\begin{cases} \dfrac{\partial u}{\partial x} + \dfrac{\partial v}{\partial y} + \dfrac{\partial w}{\partial z} = 0 \\ \dfrac{\partial \mathbf{U}_{\mathrm{I}}}{\partial t} + \dfrac{\partial \mathbf{E}_{\mathrm{I}}}{\partial x} + \dfrac{\partial \mathbf{F}_{\mathrm{I}}}{\partial y} + \dfrac{\partial \mathbf{G}_{\mathrm{I}}}{\partial z} = -\dfrac{1}{\rho}\nabla p \end{cases} , \tag{3.11}$$

with:

$$\begin{cases} \mathbf{U}_{\mathrm{I}} = \mathbf{u} = (u, v, w)^{\mathrm{T}} \\ \mathbf{E}_{\mathrm{I}} = \mathbf{E}_{\mathrm{I}}(\mathbf{u}) = (u^2, uv, uw)^{\mathrm{T}} \\ \mathbf{F}_{\mathrm{I}} = \mathbf{F}_{\mathrm{I}}(\mathbf{u}) = (uv, v^2, vw)^{\mathrm{T}} \\ \mathbf{G}_{\mathrm{I}} = \mathbf{G}_{\mathrm{I}}(\mathbf{u}) = (wu, wv, w^2)^{\mathrm{T}} \end{cases} . \tag{3.12}$$

Differently from the compressible case, these equations are entirely uncoupled from the energy equation and the system is closed by just the conservation of mass and of momentum laws. The energy equation can be solved for the temperature, if needed, in a successive phase. Moreover, also pressure and velocity are not coupled anymore and the system (3.11) has become parabolic-elliptic in nature. This causes troubles when the system is solved numerically as the instantaneous propagation of the information across

the domain requires the use of implicit iterative solvers. Looking at the incompressible model, it is also possible to notice that the pressure p has lost its physical sense when it is considered in terms of absolute value as only its gradients must be respected. This opens to the possibility of designing numerical methods which use p as a Lagrange multiplier to satisfy the incompressible constraint represented by the solenoidal condition (3.10). More detailed description of the use of the pressure to enforce incompressibility is provided later in this chapter (§3.5).
For a variable-density problem, e.g. incompressible multi-species flows, the density varies in space, therefore it has to be taken inside the differential operators in the system (3.11), thus obtaining:

$$\begin{cases} \mathbf{U}_\mathrm{I} = (\rho u, \rho v, \rho w)^\mathrm{T} \\ \mathbf{E}_\mathrm{I} = \mathbf{E}_\mathrm{I}(\mathbf{U}_\mathrm{I}) = (\rho u^2, \rho uv, \rho uw)^\mathrm{T} \\ \mathbf{F}_\mathrm{I} = \mathbf{F}_\mathrm{I}(\mathbf{U}_\mathrm{I}) = (\rho uv, \rho v^2, \rho vw)^\mathrm{T} \\ \mathbf{G}_\mathrm{I} = \mathbf{G}_\mathrm{I}(\mathbf{U}_\mathrm{I}) = (\rho wu, \rho wv, \rho w^2)^\mathrm{T} \end{cases} . \tag{3.13}$$

3.2 The discrete problem

The numerical solution of the governing equations is found by reformulating the continuous problems (3.7) and (3.11) in a set of discrete equations. This is accomplished by means of a computational grid, which divides the domain of interest in a finite number of sub-volumes (or computational cells). If one regards the discrete values as averages over each cell, then the resulting approach is called Finite Volumes (FV) (Figure 3.1), in contrast with Finite Differences (FD) which considers the discrete values as point values.
In fluid mechanics, the former method is usually preferred since it allows to respect the conservation hypotheses under which the governing equations are derived. For FV methods, the problem is solved by computing the fluxes $\mathbf{E}$, $\mathbf{F}$, $\mathbf{G}$ across the boundaries of each cell. Taking advantage of the directional-split, i.e. the possibility of splitting the three-dimensional problem as the superposition of three one-dimensional problems, from now on the equations and the methods will be presented in one dimension. This sensibly simplifies the writing of the equations and it makes a clearer explanation possible, without neglecting any of the keypoints of the methods presented. Therefore, re-writing the governing equations Equation (3.7) for the x-direction, one obtains:

$$\frac{\partial \mathbf{U}}{\partial t} + \frac{\partial \mathbf{E}}{\partial x} = 0 \,, \tag{3.14}$$

with:

$$\begin{cases} \mathbf{U} = (\rho, \rho u, E)^\mathrm{T} \\ \mathbf{E} = \mathbf{E}(\mathbf{U}) = (\rho u, \rho u^2 + p, (E+p)u)^\mathrm{T} \end{cases} . \tag{3.15}$$

Godunov (1959) produced a conservative method for solving non-linear systems of hyperbolic conservation laws:

$$\mathbf{U}_i^{n+1} = \mathbf{U}_i^n + \frac{\Delta t}{\Delta x}(\mathbf{E}_{i-\frac{1}{2}} - \mathbf{E}_{i+\frac{1}{2}}) \,, \tag{3.16}$$

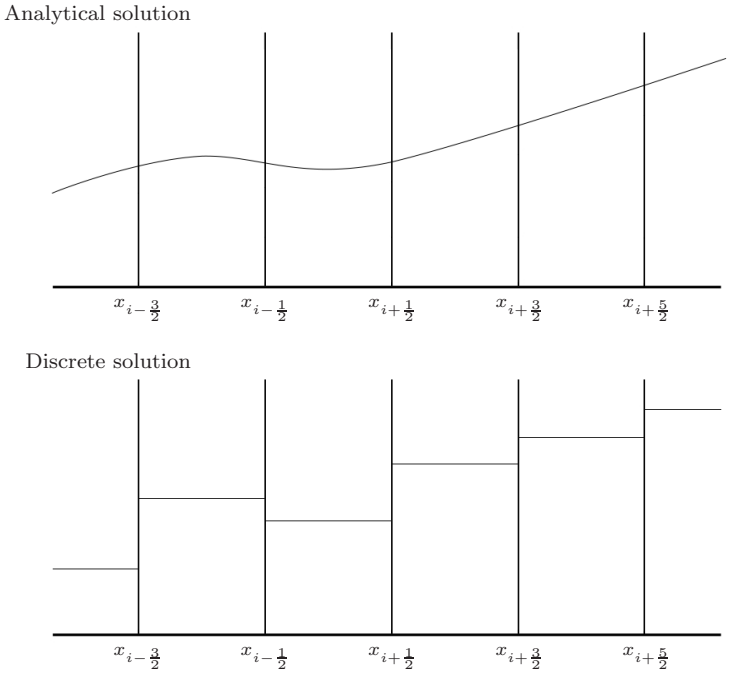

FIGURE 3.1: Original and discretised solution with FV technique. The discretisation assumes a piecewise constant distribution of the variable inside the computational cell.

where $\mathbf{E}_{i-\frac{1}{2}} = \mathbf{E}[\mathbf{U}_{i-\frac{1}{2}}(0)]$ and $\mathbf{E}_{i+\frac{1}{2}} = \mathbf{E}[\mathbf{U}_{i+\frac{1}{2}}(0)]$ are the numerical fluxes computed by solving the Riemann-problem at the cell interfaces. As presented in (3.16), the accuracy of the method is of the first-order, but it can be increased through the use of high-order and TVD methods, which are presented later in this chapter.

3.3 Time integration

The unsteady nature of the Euler equations requires to advance the system in time. Two different classes of Runge-Kutta (RK) methods are employed within this thesis. The first is the standard s-step RK method, which is defined by the following algorithm:

$$\begin{aligned} &\mathbf{U}_i^1 = \mathbf{U}_i^n \,, \\ &\mathbf{U}_i^k = \mathbf{U}_i^n + \alpha^{k-1}\Delta t \mathbf{E}_i^{k-1} \,, \qquad\qquad k = 2, ..., s \\ &\mathbf{U}_i^{n+1} = \mathbf{U}_i^n + \Delta t \sum_{k=1}^{s} \beta^k \mathbf{E}_i^{k-1} \,. \end{aligned} \tag{3.17}$$

Here, Δt is the time-step, α and β are coefficients depending on the order of accuracy of the scheme, which corresponds to the number of the intermediate steps performed. In this thesis, normally the scheme is used in its third-order accurate version, which

has the following coefficients:

$$\begin{aligned} &\alpha_1 = 1,\ \alpha_2 = \frac{1}{4}, \\ &\beta_1 = \beta_2 = \frac{1}{6},\ \beta_3 = \frac{2}{3}\ . \end{aligned} \tag{3.18}$$

In order to keep the solution stable, the use of this explicit method for marching the compressible governing equation in time and the use of Godunov-type methods for their spacial discretisation require the time-step size to be limited according to the following CFL condition:

$$\Delta t \leq \frac{\Delta x}{S^n_{\max}}\ , \tag{3.19}$$

where $S^n_{\max}$ is the maximum wave velocity present in the domain at t^n and Δx is the grid pace. The wave is therefore allowed to travel at most only for the length of a single cell Δx between two consecutive time steps[2]. In terms of CFL number, $C = S^n \Delta t/\Delta x$, the condition (3.19) corresponds to $0 < C \leq 1$.
It is possible to extend the stability of the computational process by a careful choice of the coefficients α and β. Spiteri and Ruuth (2002) produced a RK Strong-Stability-Preserving (SSP) scheme which allows a larger CFL number: $0 < C \leq 2$. In the method presented by the authors, the number of sub-step does not equal the order of accuracy p, like in the standard RK method, since the SSP class $s = p + 1$ is valid. The authors report that the additional computational cost increases the efficiency of the scheme because it allows the extention of the upper bound of the CFL number. In this thesis, the second-order accurate version of the RK-SSP scheme ($s = 3$) is typically employed:

$$\begin{aligned} &\alpha_1 = \alpha_2 = \frac{1}{2}, \\ &\beta_1 = \beta_2 = \beta_3 = \frac{1}{3}\ . \end{aligned} \tag{3.20}$$

3.4 Numerics for compressible flows

3.4.1 Solution of the Riemann problem

Godunov-type methods are based on the solution of the Riemann problem at the cell interfaces. Considering the discrete values as averages of the flow variables over a cell implies that the left and the right values at a given cell interface, $\mathbf{E}_L$ and $\mathbf{E}_R$, are different and thus a discontinuity is produced in correspondence of these points of the numerical domain (Figure 3.1). It is therefore necessary to resolve the associated Riemann problem in order to find a unique value for the intercell flux. The structure of the solution is represented in Figure 3.2 and it consists of three waves travelling with speeds determined by the eigenvalues of Equation (3.14): $\lambda_1 = u - a$, $\lambda_2 = u + a$, $\lambda_3 = u$.
The first two eigenvalues correspond to either shock or rarefaction waves, whereas the third one is a contact wave. Since the solutions to the left and to the right of the waves

[2]This is valid only under the assumption that no wave acceleration due to waves interaction takes place.

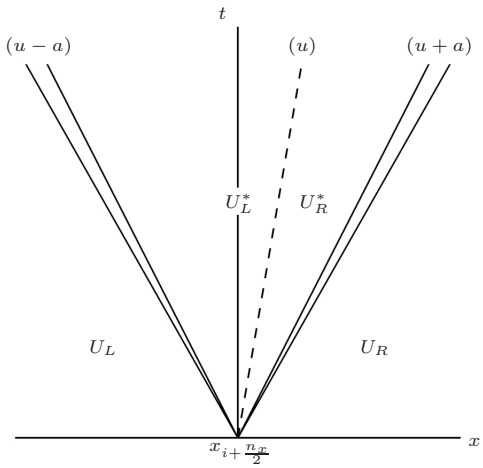

FIGURE 3.2: Structure of the solution of the Riemann problem for the one-dimensional Euler equations in the $x-t$ plane. The same pattern is found at every cell interface $x_{i+\frac{n_x}{2}}$ with $0 < n_x < N_x$ and N_x number of cells along the x direction.

λ_1 and λ_2 are known, the task of the Riemann solver is to find a solution inside the wedge between those waves, which is formally called 'star region'.
There are several schemes which either find the exact or approximate solution of the problem, as detailed by Toro (2009). In this thesis, the approximate solvers HLLC by Toro et al. (1994) and the Characteristic-Based (CB) by Eberle (1987) are employed, since both have been assessed to provide a good balance between accuracy and computational costs (Bagabir and Drikakis, 2004).

The HLLC solver

The HLLC scheme is an approximate solver. Harten et al. (1983) presented the original formulation and it was named HLL. This method assumes a wave configuration which consists of two waves separating three constant states, thus neglecting the contact wave. Toro et al. (1994) improved the method by restoring the third wave which is present in the original solution and which allows to solve physical features such as contact surfaces, material interfaces and shear waves. This formulaton is known as HLLC solver:

$$\mathbf{E}^{\mathrm{HLLC}}_{i+\frac{1}{2}} = \begin{cases} \mathbf{E}_L & \text{if} \quad 0 \leq S_L \\ \mathbf{E}^*_L = \mathbf{E}_L + S_L(\mathbf{U}^*_L - \mathbf{U}_L) & \text{if} \quad S_L \leq 0 \leq S^* \\ \mathbf{E}^*_R = \mathbf{E}_R + S_R(\mathbf{U}^*_R - \mathbf{U}_R) & \text{if} \quad S^* \leq 0 \leq S_R \\ \mathbf{E}_R & \text{if} \quad 0 \geq S_R \end{cases}, \tag{3.21}$$

where $\mathbf{U}^*_K$ (with $K = L, R$) are:

$$\mathbf{U}^*_K = \rho_K \left(\frac{S_K - u_K}{S_K - S^*} \right) \begin{bmatrix} 1 \\ S^* \\ v_K \\ w_K \\ \frac{E_K}{\rho_K} + (S^* - u_K)\left[S^* + \frac{p_K}{\rho_K (S_K - u_K)} \right] \end{bmatrix}, \tag{3.22}$$

and S^*, S_L, S_R are the wave speeds, which can be computed according to Batten et al. (1997).

The characteristic-based solver

Eberle (1987) introduced a Characteristic-Based (CB) method for calculating compressible Godunov fluxes.

$$\mathbf{E}^{\mathrm{CB}}_{i+\frac{1}{2}} = \begin{pmatrix} \widetilde{\rho u} \\ \widetilde{\rho u}^2/\tilde{\rho} + \tilde{p} \\ \widetilde{\rho u}\widetilde{\rho v}/\tilde{\rho} \\ \widetilde{\rho u}\widetilde{\rho w}/\tilde{\rho} \\ \widetilde{\rho u}(\tilde{E}+\tilde{p})/\tilde{\rho} \end{pmatrix} , \tag{3.23}$$

where the flow variables at the cell interfaces are given by the following:

$$\widetilde{\rho} = \rho_0 + r_1 + r_2 , \tag{3.24}$$
$$\widetilde{\rho u} = (\rho u)_0 + (u+c)r_1 + (u-c)r_2 , \tag{3.25}$$
$$\widetilde{\rho v} = (\rho v)_0 + (v+c)r_1 + (v-c)r_2 , \tag{3.26}$$
$$\widetilde{\rho w} = (\rho w)_0 + (w+c)r_1 + (w-c)r_2 , \tag{3.27}$$
$$\widetilde{E} = E_0 + (H + a\lambda_0)r_1 + (H - a\lambda_0)r_2 . \tag{3.28}$$

Here, H is the total enthalpy, c is the speed of sound and the coefficients r_1 and r_2 are defined in the following manner:

$$r_1 = \frac{1}{2\gamma}(q_1 - q_0) , \tag{3.29}$$
$$r_2 = \frac{1}{2\gamma}(q_2 - q_0) , \tag{3.30}$$

where q_n, with $n = 1, 2, 3$, are the values along the three characteristics defined as:

$$q_n = \frac{1}{2}([1 + \mathrm{sign}(\lambda_n)]U_L + [1 - \mathrm{sign}(\lambda_n)]U_R) , \tag{3.31}$$

with λ_n, $n = 0, 1, 2$ eigenvalues of the system, which along the x-direction are defined as:

$$\lambda_0 = u , \tag{3.32}$$
$$\lambda_1 = \lambda_0 + c , \tag{3.33}$$
$$\lambda_2 = \lambda_0 - c . \tag{3.34}$$

The quantities U_R and U_L are elements of the vector of the the right and left states of the conserved variables $\mathbf{U}_R$ and $\mathbf{U}_L$.

3.4.2 High-resolution methods

The use of Riemann-solvers requires the variable states at the left and right of the cell interface $\mathbf{U}_L$ and $\mathbf{U}_R$. Godunov (1959) assumed a piecewise constant distribution of the variables inside the cell, as shown in Figure 3.1. In this case, the right and left states simply correspond to the cell-centred values, $\mathbf{U}_i$ and $\mathbf{U}_{i+1}$ respectively. The work of Van Leer (1977) laid the foundations for the achievement of high-order accuracy, producing a new class of numerical schemes called high-resolution methods (Harten, 1983; Drikakis and Rider, 2004), which are the very inner core of ILES. These algorithms interpolate the values over a proper stencil of cells and they reconstruct the sought states $\mathbf{U}_L$ and $\mathbf{U}_R$. The main feature which distinguishes them from the standard methods is that they make use of their intrinsic nonlinearity in order to control the spurious oscillations, which classical methods are affected by, in proximity of discontinuities such as shock waves. Van Leer built his method using three keypoints: the idea of piecewise linear distribution of the variable inside the computational cell instead of piecewise constant distribution originally adopted by Godunov, the use of Total Variation Diminishing (TVD) property and the idea of monotone limiters[3]. A variety of different high-resolution methods are available today. A curious reader can find more detailed explanations in the papers and books which are cited in this section. In this work, the Monotone Upstream-centred Schemes for Conservation Laws (MUSCL) technique and the Weighted Essentially Non-Oscillatory (WENO) methods are employed.

MUSCL-type methods

With his innovative work, Van Leer (1977) introduced the MUSCL technique, which in its TVD variant is written:

$$\begin{aligned} \mathbf{U}_L &= \mathbf{U}_i + \frac{1}{2}\varphi(r_L)(\mathbf{U}_i - \mathbf{U}_{i-1}) \,, \\ \mathbf{U}_R &= \mathbf{U}_i + \frac{1}{2}\varphi(r_R)(\mathbf{U}_{i+2} - \mathbf{U}_{i+1}) \,, \end{aligned} \tag{3.35}$$

where:

$$\begin{aligned} r_L &= \frac{\mathbf{U}_{i+1} - \mathbf{U}_i}{\mathbf{U}_i - \mathbf{U}_{i-1}} \,, \\ r_R &= \frac{\mathbf{U}_i - \mathbf{U}_{i-1}}{\mathbf{U}_{i+1} - \mathbf{U}_i} \,, \end{aligned} \tag{3.36}$$

and $\varphi(r_K)$ $(K = R, L)$ is the limiter, which assigns the distribution of the interpolated variable inside the computational cells, i.e. piecewise linear, piecewise quadratic etc, allowing to achieve different orders of accuracy. Throughout the thesis, three different choices for $\varphi(r_K)$ are considered:

1. Van-Leer limiter, second-order accurate (M2) (Van Leer, 1977):

$$\varphi(r_K) = \frac{r_K + |r_K|}{1 + r_K} \,. \tag{3.37}$$

[3]Monotone limiters limit the piecewise profile in one cell to be bounded between the cell average value of the neighbouring cells.

2. Kim-Kim limiters (Kim and Kim, 2005):

$$\begin{aligned} \varphi(r_L) &= \max[0, \min(2, 2r_L, \beta_L)] \,, \\ \varphi(r_R) &= \max[0, \min(2, 2r_{R+1}, \beta_R)] \,. \end{aligned} \tag{3.38}$$

The order of accuracy of this limiter can be modified depending on the formulation used for β_{L} and β_{R}. Third-order (M3) is achieved imposing:

$$\begin{aligned} \beta_L &= \frac{1 + 2r_{L,i}}{3} \,, \\ \beta_R &= \frac{1 + 2r_{R,i+1}}{3} \,, \end{aligned} \tag{3.39}$$

whereas fifth-order (M5) is obtained using:

$$\begin{aligned} \beta_L &= \frac{-2/r_{L,i-1} + 11 + 24r_{L,i} - 3r_{L,i}r_{L,i+1}}{30} \,, \\ \beta_R &= \frac{-2/r_{R,i+2} + 11 + 24r_{R,i+1} - 3r_{R,i+1}r_{R,i}}{30} \,. \end{aligned} \tag{3.40}$$

WENO-type methods

The second class of high-resolution methods taken into consideration is that of WENO (Liu et al., 1994). This is a subset of the ENO schemes (E and Shu, 1994), which differs from the MUSCL approach because it does not make use of limiters to enforce monotonicity. The main idea behind ENO schemes is to control the total variation of the solution through the selection of an interpolating stencil where the solution is the 'smoothest'. On the other hand, WENO methods use a combination of all the possible convex polynomials $P_i(x)$, which represent the reconstructed solution $U(x)$, in order to achieve the essentially non-oscillatory property:

$$P_i(x) = \sum_{k=0}^{r-1} \frac{a_k^i p_{i+k}(x)}{\sum_{l=0}^{r-1} a_l^i} = U(x) + \mathcal{O}(\Delta x^r) \,, \tag{3.41}$$

where r is the order of accuracy and a_k^i, with $k = 1, ..., r-1$, are positive coefficients defined as:

$$a_k^i = \frac{C_k^i}{(\epsilon + IS_{i+k})^r} \,. \tag{3.42}$$

Here, ϵ is a small positive number which prevents the division by zero, IS is the smoothness indicator and $C_k^i = \mathcal{O}(1)$, with $C_k^i \geq 0$. In the present study, the fifth- (W5), $r = 4$, and ninth- (W9), $r = 8$, order accurate versions of this scheme are considered.

Low Mach Correction

It is known that the upwind behaviour of high-resolution, shock-capturing Godunov methods cause an anomalous dissipation of kinetic energy. Thornber et al. (2008a) demonstrated that the consequent excess in the increase of entropy is not physical, but it is due to the discrete nature of the system. This strongly affects the capability of the scheme in capturing low-Mach number features and it is thus a crucial issue for simulating Richtmyer-Meshkov instability. Thornber et al. (2008b) proposed a simple modification of the variable reconstruction process which significantly improves the resolution of the scheme. Once $\mathbf{U}_L$ and $\mathbf{U}_R$ are computed by the chosen high-resolution method, it consists in modifying the velocity jump at the cell interface as follows:

$$\begin{aligned} \mathbf{U}_L &= \frac{\mathbf{U}_L + \mathbf{U}_R}{2} + z\frac{\mathbf{U}_L - \mathbf{U}_R}{2} , \\ \mathbf{U}_R &= \frac{\mathbf{U}_L + \mathbf{U}_R}{2} + z\frac{\mathbf{U}_R - \mathbf{U}_L}{2} . \end{aligned} \tag{3.43}$$

The authors investigated different forms for z and they found that $z = \min(M_{local}, 1)$, with $M_{local} = \max(M_L, M_R)$, gives the best results and it is therefore adopted for the simulations presented in this thesis.

3.5 The pressure-projection method

As previously mentioned, high-resolution methods were initially designed to avoid spurious oscillations which afflict standard numerical methods when they are used to compute discontinuities, such as shock waves, present in compressible numerical fields. With their pioneer work, Bell and Colella (1989) adapted these methods, with remarkable results, also for the purpose of computing incompressible fluxes, taking advantage of the fact that the effects of the unsolved subgrid scales are implicitly modeled by the numerics and neither turbulence model nor SGS model is therefore needed. The authors developed a second-order high-resolution incompressible solver for the constant-density Navier-Stokes equations based on the Pressure-Projection (PP) technique already introduced by Chorin (1968, 1969). This work was successively extended to incompressible variable-density flows by Bell and Marcus (1992). Here, the convection-diffusion terms of the equations were treated using the Godunov-type method and the projection operator was approximated by discrete Galerkin approach. In this work, the authors successfully proved the applicability of high-resolution methods to different incompressible problems such as Poiseuille flow and Rayleigh-Taylor instability. In E and Shu (1994) the work of Bell and Marcus was extended through the use of ENO schemes for the advection in conjunction with spectral methods for the pressure. Another attempt was successfully done in Andrews (1995), where the fractional-step approach based on the Van Leer (1977) method was employed to solve a two-phase incompressible flow. Recently, an innovative characteristic-based approach was also developed by Shapiro and Drikakis (2005a). Here, the authors used high-resolution methods to solve the incompressible flow model in its artificial-compressibility formulation, presenting three possible variants which are characterised by a different formulation of the transport equation for the total density and by the use of the divergence-free condition. Diffusion

broadening studies and 2D KHI simulations showed good agreement with analytical and experimental results, especially when second- and third-order reconstruction at cell interfaces was employed (Shapiro and Drikakis, 2005b).
In this thesis, the PP method is considered in order to develop a new solver which makes use of high-resolution methods. Particular attention is given to the Riemann solver for the intercell fluxes.
The main idea behind the projection methods is to make use of the Hodge decomposition to overcome the pressure-velocity decoupling in the incompressible formulation of the governing equations (3.11). This decomposition splits a given vector field, $\widetilde{\mathbf{U}}$, into the sum of its divergence-free part, $\mathbf{U}_\mathrm{I}$, and its curl-free part $\nabla\phi$. For a varible-density incompressible flow:

$$\widetilde{\mathbf{U}} = \mathbf{U}_\mathrm{I} + \sigma\nabla\phi \,, \tag{3.44}$$

where $\sigma = 1/\rho$. The equation for the potential ϕ is found by taking the divergence of (3.44) and applying the incompressibility constraint $\nabla \cdot \mathbf{U}_\mathrm{I} = 0$. This yields to the Poisson-equation:

$$\nabla \cdot \widetilde{\mathbf{U}} = \nabla \cdot \sigma\nabla\phi \,. \tag{3.45}$$

Once ϕ is computed, the soultion can be found from Equation (3.44):

$$\mathbf{U}_\mathrm{I} = \widetilde{\mathbf{U}} - \sigma\nabla\phi \,. \tag{3.46}$$

From a global point of view, the PP method makes use of a projection operator $\mathcal{P}$ such that:

$$\mathbf{U}_\mathrm{I} = \mathcal{P}(\widetilde{\mathbf{U}}) \,, \tag{3.47}$$

where $\mathcal{P}$ can be written from the steps above as:

$$\mathcal{P} = \mathbf{I} - \sigma\nabla(\nabla \cdot \sigma\nabla)^{-1}\nabla\cdot \,, \tag{3.48}$$

After the application of the projection operator to the vector field $\widetilde{\mathbf{U}}$, this becomes divergence-free. For a more detailed explanation on the properties of $\mathcal{P}$, a curious reader can refer to Chorin and Marsden (1993). The application of this method to the Euler equations produces a Poisson equation for the pressure ($\phi \equiv p$) and depending on the discrete form of this equation, the PP method can be either exact or approximate. It is known that in the continuous case the following relation is always valid:

$$\nabla \cdot \nabla = \nabla^2 \,, \tag{3.49}$$

whereas in the discrete case, this equality does not hold. In fact, considering $\mathbf{G}_{i,j,k}$ the discrete gradient, $D_{i,j,k}$ the discrete divergence operator and $L_{i,j,k}$ the discrete Laplacian operator, it is easy to show that $D_{i,j,k}(\mathbf{G}_{i,j,k}) \neq L_{i,j,k}$. This represents the key difference between exact and approximate projection methods, i.e. the composition of $\mathbf{G}_{i,j,k}$ and $D_{i,j,k}$ to form the Laplacian which is inverted to accomplish the projection. Exact projection methods retain the form $\nabla \cdot \nabla$, which in the discrete case is $D_{i,j,k}(\mathbf{G}_{i,j,k})$. This allows to formally respect the definition of Laplacian and therefore

to obtain a discrete divergence of the velocity which is very close to zero depending on the residual imposed to the iterative process for the computation od the pressure and on the machine precision on which the simulations are run. On the contrary, in approximate projection approaches the operator $D_{i,j,k}(\mathbf{G}_{i,j,k})$ is directly replaced by $L_{i,j,k}$, following the continuous formulation. Hence, the divergence-free constraint is no longer rigorously respected and the value of the divergence of velocity becomes a function of the truncation error of the scheme used.
From a computational point of view, the exact projection is more expensive than the approximate projection which, on the other hand, is more difficult to implement because it requires the use of filters in order to cancel the 'checkerboard' effect which appears when compressible modes are still present in the incompressible field (Drikakis and Rider, 2004). For the method presented in this document, the exact projection technique is chosen since it does not need any filtering operation, allowing to fully respect the divergence-free constraint without any additional artifact.
From a practical point of view, the PP method proceeds as follows:

1. Advancing of the solution in time disregarding the solenoidal nature of the computational field;

2. Calculation of the pressure by solving a Poisson-equation for the pressure;

3. Use of p to recover the divergence-free solution through Equation (3.44).

Before proceeding with a more detailed explanation of the method, it is necessary to point out that the directional split used to present the compressible methods is not usually valid for the resolution of the incompressible flow model. This is due to the divergence-free constraint which requires the case to be defined at least in two dimensions. Hence, the complete three-dimensional equations should be marched in time in their complete form:

$$\widetilde{\mathbf{U}}_{\mathrm{I}}^{n+1} = \mathbf{U}_{\mathrm{I}}^{n} - \Delta t \left(\frac{\partial \mathbf{E}_{\mathrm{I}}}{\partial x} + \frac{\partial \mathbf{F}_{\mathrm{I}}}{\partial y} + \frac{\partial \mathbf{G}_{\mathrm{I}}}{\partial z} \right) . \tag{3.50}$$

The use of the PP method allows to bypass this issue since the incompressibility of the field is recovered at the end of the time-stepping loop. Therefore, the first phase of the solver can be explained once again taking advantage of the dimensional split. The extention to three dimensions is immediate.
The first step of the algorithm is to march in time the momentum equations in Equation (3.11) without taking into account the pressure term. In this way, a temporary tilda-solution, which is not physically meaningful, is obtained. The use of high-resolution methods is made possible by emplying Godunov-type methods for the discretisation of the governing equations. Neglecting the subscript $(.)_{\mathrm{I}}$:

$$\widetilde{\mathbf{U}}_{i}^{n+1} = \mathbf{U}_{i}^{n} - \frac{\Delta t}{\Delta x}(\mathbf{E}_{i+\frac{1}{2}} - \mathbf{E}_{i-\frac{1}{2}}) \tag{3.51}$$

where $\mathbf{E}_{i-\frac{1}{2}} = \mathbf{E}[\mathbf{U}_{i-\frac{1}{2}}(0)]$ and $\mathbf{E}_{i+\frac{1}{2}} = \mathbf{E}[\mathbf{U}_{i+\frac{1}{2}}(0)]$ are the incompressible solutions of the Riemann problem at the cell-interfaces. The time-stepping methods employed for this purpose are the RK methods presented in §3.3.

3.5.1 Riemann-solvers

The Riemann-solvers employed in compressible flows cannot be used for computing incompressible fluxes. Contrarily to the latter case where the information propagates instantaneously across the domain, in the former case the information travels with a speed which is the speed of the flow plus the speed of sound and parameters which are not included in the incompressible formulation of the equations (e.g. a, γ, etc) are required. This imples that Riemann-solvers must somehow be modified in order to take into account the nature of the flow. Here, three schemes originally formulated for compressible flows and adapted for incompressible fluxes are presented.

Lax-Friedrichs

The first and the simplest method employed for advecting the fluxes is the Lax-Friedrichs (LF) scheme. The original formulation was originally proposed by Lax (1954):

$$\mathbf{E}^{\mathrm{LF}}_{i+\frac{1}{2}} = \frac{1}{2}\left[(\mathbf{E}_L + \mathbf{E}_R) + \frac{1}{\alpha}\frac{\Delta x}{\Delta t}(\mathbf{U}_L - \mathbf{U}_R)\right] . \tag{3.52}$$

Here, α is set equal to the number of dimensions of the problem. Differently from the methods presented for compressible cases, the LF scheme does not require any parameters which are not available in the incompressible model, therefore no adaptation is necessary.

Rusanov

The second method considered is the Riemann-solver presented by Rusanov (1961):

$$\mathbf{E}^{\mathrm{RU}}_{i+\frac{1}{2}} = \frac{1}{2}\left[(\mathbf{E}_L + \mathbf{E}_R) - S(\mathbf{U}_R - \mathbf{U}_L)\right] , \tag{3.53}$$

where S is the highest wave speed computed in the cell:

$$S = \max\{|u_L - a_L|, |u_R - a_R|, |u_L + a_L|, |u_R + a_R|\} . \tag{3.54}$$

Since in the incompressible fluid model the information travels across the domain with infinite speed, it is not possible to directly apply Equation (3.54) and a new definition for S is required. The real wave speed of the compressible model is therefore replaced by a 'fictitious' wave speed, which assumes that the information travels across the cell with the same speed of the fluid. Therefore, the new $\overline{S}$ simply becomes:

$$\overline{S} = \max\{|u_L|, |u_R|\} . \tag{3.55}$$

HLL

The third and last method considered is the classic two-waves Riemann solver HLL by Harten et al. (1983):

$$\mathbf{E}^{\mathrm{HLL}}_{i+\frac{1}{2}} = \begin{cases} \mathbf{E}_L & \text{if} \quad 0 \leq S_L \\ \dfrac{S_R\mathbf{E}_L - S_L\mathbf{E}_R + S_R S_L(\mathbf{E}_R - \mathbf{E}_L)}{S_R - S_L} & \text{if} \quad S_L \leq 0 \leq S_R \\ \mathbf{E}_R & \text{if} \quad 0 \geq S_R \end{cases} . \tag{3.56}$$

The compressible wave speeds S_L and S_R are provided by Batten et al. (1997). For the incompressible model, the formulation of the solver remains unchanged, but, as for the Rusanov case, the wave speeds are revisited. The incompressible fictitious wave speeds $\overline{S_R}$ and $\overline{S_L}$ in Equation (3.56) are chosen as:

$$\begin{aligned} \overline{S_R} &= \max\{u_L, u_R, 0\} , \\ \overline{S_L} &= \min\{u_L, u_R, 0\} . \end{aligned} \tag{3.57}$$

The left and right states of the variables required in Equations (3.52), (3.53) and (3.56) are computed by the high-resolution schemes presented in §3.4.2.

3.5.2 The Poisson-equation for the pressure

The first step of the PP method is formally equal to the compressible algorithm. In fact, within a single RK step, firstly the right and left states of the variables are reconstructed and secondly the Riemann problem at the interface is solved. Hence, when the necessary number of RK steps is performed, in the compressible case it is possible to proceed to the next time-step, whereas in the incompressible case the variables have to go through the second phase of the algorithm in order to calculate the pressure which was neglected in the first place. As previously mentioned, the multi-dimensional nature of the incompressible fluxes requires the pressure equation to be presented in its complete three-dimensional form. According to the Hodge decomposition (3.44), in order to recover the divergence-free component of $\widetilde{\mathbf{U}}^{n+1}$, it is necessary to solve a Poisson equation for the scalar ϕ (3.45), which in this case it is the pressure p. In fact, considering variable-density flows, dividing both sides of Equation (3.50) by the density and imposing $\nabla \cdot \mathbf{U}^{n+1} = 0$, a Poisson-equation for the pressure is obtained:

$$\nabla \cdot \left(\frac{1}{\rho^{n+1}} \nabla p^{n+1} \right) = \frac{1}{\Delta t} \nabla \cdot \left(\widetilde{\mathbf{U}}^{n+1} \right) . \tag{3.58}$$

A variety of different discretisation schemes can be used for discretising the Laplacian operator in (3.58) and with different arrangements on the grid (i.e. collocated or staggered). For this solver, the arrangement of the pressure on the grid is chosen to be collocated and the exact projection deletes all the non divergence-free modes which would affect the solution. The Left Hand-Side (LHS) of the pressure equation is discretised using backward and forward differences for the gradient and the divergence

operators respectively. Considering $\sigma = 1/\rho$, the discrete gradient of the pressure, $\sigma \mathbf{G}_{i,j,k} p$, becomes:

$$\sigma \mathbf{G}_{i,j,k} p = \frac{1}{\rho_{i,j,k}} \begin{pmatrix} \dfrac{p_{i,j,k} - p_{i-1,j,k}}{\Delta x} \\ \\ \dfrac{p_{i,j,k} - p_{i,j-1,k}}{\Delta y} \\ \\ \dfrac{p_{i,j,k} - p_{i,j,k-1}}{\Delta z} \end{pmatrix} . \tag{3.59}$$

In order to obtain the discrete Laplacian, it is now necessary to take the discrete divergence, $D_{i,j,k}$, of (3.59). Considering $\mathbf{V} = \sigma \mathbf{G}_{i,j,k} p$, it is possible to write:

$$D_{i,j,k}\mathbf{V} = \frac{V^x_{i+1,j,k} - V^x_{i,j,k}}{\Delta x} + \frac{V^y_{i,j+1,k} - V^y_{i,j,k}}{\Delta y} + \frac{V^z_{i,j,k+1} - V^z_{i,j,k}}{\Delta z} , \tag{3.60}$$

where the superscript $(.)^k$ indicates the derivative of the term with respect to k. After some handling, the discrete form of the LHS of the pressure equation is:

$$\begin{aligned} D_{i,j,k}\mathbf{V} &= \frac{\sigma_{i+1,j,k}(p_{i+1,j,k} - p_{i,j,k}) - \sigma_{i-1,j,k}(p_{i,j,k} - p_{i-1,j,k})}{\Delta x^2} \\ &+ \frac{\sigma_{i,j+1,k}(p_{i,j+1,k} - p_{i,j,k}) - \sigma_{i,j-1,k}(p_{i,j,k} - p_{i,j-1,k})}{\Delta y^2} \\ &+ \frac{\sigma_{i,j,k+1}(p_{i,j,k+1} - p_{i,j,k}) - \sigma_{i,j,k-1}(p_{i,j,k} - p_{i,j,k-1})}{\Delta z^2} . \end{aligned} \tag{3.61}$$

Here, the value of the density is the one at the neighbouring cell-centres. To write the discretisation in a more consistent way, the density was shifted to the cell-interfaces:

$$\begin{aligned} D_{i,j,k}\mathbf{V} &= \frac{\sigma_{i+1/2,j,k}(p_{i+1,j,k} - p_{i,j,k}) - \sigma_{i-1/2,j,k}(p_{i,j,k} - p_{i-1,j,k})}{\Delta x^2} \\ &+ \frac{\sigma_{i,j+1/2,k}(p_{i,j+1,k} - p_{i,j,k}) - \sigma_{i,j-1/2,k}(p_{i,j,k} - p_{i,j-1,k})}{\Delta y^2} \\ &+ \frac{\sigma_{i,j,k+1/2}(p_{i,j,k+1} - p_{i,j,k}) - \sigma_{i,j,k-1/2}(p_{i,j,k} - p_{i,j,k-1})}{\Delta z^2} . \end{aligned} \tag{3.62}$$

Here, the values of the density at the edges $\sigma_{i\pm1/2,j,k}$, $\sigma_{i,j\pm1/2,k}$, $\sigma_{i,j,k\pm1/2}$ are calculated taking the average between the neighbouring cells: $\sigma_{i\pm1/2,j,k} = (\sigma_{i\pm1,j,k} + \sigma_{i,j,k})/2$, $\sigma_{i,j\pm1/2,k} = (\sigma_{i,j\pm1,k} + \sigma_{i,j,k})/2$ and $\sigma_{i,j,k\pm1/2} = (\sigma_{i,j,k\pm1} + \sigma_{i,j,k})/2$. This formulation has the exact structure of the one which is possible to find if central differences are used for computing either $\mathbf{G}_{i,j,k}$ and $D_{i,j,k}$. In this case, the combination of the two discrete operators yields:

$$\begin{aligned} D_{i,j,k}\mathbf{V} &= \frac{\sigma_{i+1,j,k}(p_{i+2,j,k} - p_{i,j,k}) - \sigma_{i-1,j,k}(p_{i,j,k} - p_{i-2,j,k})}{4\Delta x^2} \\ &+ \frac{\sigma_{i,j+1,k}(p_{i,j+2,k} - p_{i,j,k}) - \sigma_{i,j-1,k}(p_{i,j,k} - p_{i,j-2,k})}{4\Delta y^2} \\ &+ \frac{\sigma_{i,j,k+1}(p_{i,j,k+2} - p_{i,j,k}) - \sigma_{i,j,k-1}(p_{i,j,k} - p_{i,j,k-2})}{4\Delta z^2} . \end{aligned} \tag{3.63}$$

Comparing (3.62) with (3.63) it is possible to notice how the formulations are substantially identical, but the computational stencil of the former is halved with respect to the latter. Both formulations were tested during the development of the method and it was found that, as expected, the convergence process is much stabler for (3.62). In fact the reduced stencil allows to capture the gradients of the pressure better, thus giving a more accurate solution and easing the convergence process of the iterative solver.
The RHS of (3.58) is discretised using central differences to maintain the overall second-order of accuracy:

$$\mathrm{b}_{i,j,k} = \frac{1}{2\Delta t}\left(\frac{\widetilde{u}_{i+1,j,k} - \widetilde{u}_{i-1,j,k}}{\Delta x} + \frac{\widetilde{v}_{i,j+1,k} - \widetilde{v}_{i,j-1,k}}{\Delta y} + \frac{\widetilde{w}_{i,j,k+1} - \widetilde{w}_{i,j,k-1}}{\Delta z}\right) . \tag{3.64}$$

Considering $N = N_x N_y N_z$ the total number of cells, the final discrete form of the pressure equation yields to a linear system of equations:

$$\mathbf{A}\mathbf{p} = \mathbf{b} , \tag{3.65}$$

where $\mathbf{A}$ is the matrix of the coefficients of dimensions $N \times N$, $\mathbf{b}$ is the vector of the known terms of dimension N and $\mathbf{x}$ the vector of the unknown pressure distribution of dimension N. The general form of the linear problem can be written:

$$\begin{aligned} ap_{i+1,j,k} + bp_{i,j+1,k} + cp_{i,j,k+1} + dp_{i-1,j,k} \\ + ep_{i-1,j,k} + fp_{i,j-1,k} + gp_{i,j,k-1} = \mathrm{b}_{i,j,k} , \end{aligned} \tag{3.66}$$

where a, b, c, d, e, f, g, are coefficients of the problem included in matrix of the coefficients $\mathbf{A}$:

$$a = \frac{\sigma_{i+1/2,j,k}}{\Delta x^2} , \quad b = \frac{\sigma_{i,j+1/2,k}}{\Delta y^2} , \quad c = \frac{\sigma_{i,j,k+1/2,k}}{\Delta z^2} , \tag{3.67}$$

$$d = -\frac{\sigma_{i+1/2,j,k} + \sigma_{i-1/2,j,k}}{\Delta x^2} - \frac{\sigma_{i,j+1/2,k} + \sigma_{i,j-1/2,k}}{\Delta y^2} - \frac{\sigma_{i,j,k+1/2} + \sigma_{i,j,k-1/2}}{\Delta z^2} , \tag{3.68}$$

$$e = \frac{\sigma_{i-1/2,j,k}}{\Delta x^2} , \quad f = \frac{\sigma_{i,j-1/2,k}}{\Delta y^2} , \quad g = \frac{\sigma_{i,j,k-1/2}}{\Delta z^2} . \tag{3.69}$$

The implicit nature of the system of equations Equation (3.66) requires it to be solved iteratively using appropriate algorithms. Once the pressure is computed, is it possible to recover the sought incompressible solution projecting $\widetilde{\mathbf{U}}$ in the divergence-free space according to the Hodge decomposition:

$$\mathbf{U}^{n+1} = \widetilde{\mathbf{U}}^{n+1} - \Delta t \nabla p^{n+1} . \tag{3.70}$$

The solver is now ready to advance to the next time-step.

3.5.3 Solution of the pressure-equation

The creation of efficient and robust iterative methods for the solution of linear systems of equations has always been a topic of great discussion in scientific community since it is of interest in different fields. Nowadays, a variety of different solvers based on different techniques are available in the literature (Hirsch, 1988; Kelly, 1995; Saad, 1996; Beauwens, 2004). During the past twenty years, Krylov subspace methods (Arnoldi, 1951; Lanczos, 1952) has surely become the class of algorithms which defeated the other classes for robustness and efficiency. Defining the initial residual vector as:

$$\mathbf{r}_0 = \mathbf{b} - \mathbf{A}\mathbf{x}_0 \,, \tag{3.71}$$

where $\mathbf{x}_0$ is the initial guess for the vector of unknowns, Krylov subspace methods estimate the eigenvalues of $\mathbf{A}$ by picking off the largest and forming a polynomial basis for the solution defined as:

$$\{\mathbf{r}_0, \mathbf{r}_1, \mathbf{r}_2, ..., \mathbf{r}_I\} \,, \tag{3.72}$$

where I is the number of iterations. This sequence of polynomials forms an orthogonal basis for the Krylov subspace:

$$\{\mathbf{r}_0, \mathbf{A}\mathbf{r}_0, \mathbf{A}^2\mathbf{r}_0, ..., \mathbf{A}^{i-1}\mathbf{r}_0\} \,. \tag{3.73}$$

At every iteration, the gap between the largest and the lowest eigenvalues of the matrix of the coefficients becomes smaller and smaller and the contribution of each iteration to the solution decreases until convergence is reached. A variety of different methods which take advantage of this technique have been designed (Van der Vorst, 2000). The very first solver which made use of the Krylov subspace was the Conjugate Gradients (CG) method by Hestenes and Stiefel (1952), which solves symmetric positive defined problems. Even though this approach was presented in the early '50s, it did not gain much recognition for twenty years since the original scheme was lacking of exactness. Reid (1972) was the first to notice the potential in the work of Hestenes and Stiefel and succeeded in making the CG a proper iterative solver. The work of Kershaw (1978) improved the method by adding the possibility of preconditioning. Since then, a variety of different algorithms which take advantage of the Krylov subspace were created, e.g. Conjugate Gradients Squared (CGS) (Sonneveld, 1989), Bi-Conjugate Gradients (BiCG) (Fletcher, 1975), Quasi Minimal Residual (QMR) (Freund and Nichitgal, 1991) and Generalised Minimal Residual (GMRES) (Saad and Schultz, 1986). In the present context, the Stabilised Bi-Conjugate Gradients method (BiCGSTAB) (Van der Vorst, 1992) is employed. This method was created as an alternative to the CGS method for non-symmetric linear systems. It was noticed that CGS suffers from irregular convergence behaviour when the first guess for the start of the iterative process is close to the final solution, leading to severe spoiling of the final outcome. In BiCGSTAB, this issue was solved and moreover the smooth convergence properties typical of BiCG were retained.

ALGORITHM OF STABILISED BI-CONJUGATE METHOD.

$\mathbf{x}_0$ is an initial guess of the solution; (1)
$\mathbf{r}_0 = \mathbf{b} - \mathbf{A}\mathbf{x}_0$; (2)
$\widehat{\mathbf{r}}_0$ is an arbitrary vector such that $(\widehat{\mathbf{r}}_0, \mathbf{r}_0) \neq 0$, e.g. $\widehat{\mathbf{r}}_0 = \mathbf{r}_0$; (3)
$\rho_0 = \omega_0 = \alpha = 1$; (4)
$\mathbf{v}_0 = \mathbf{p}_0 = 0$; (5)

for $i = 1, ..., N$
  $\rho_i = (\widehat{\mathbf{r}}_0, \mathbf{r}_{i-1})$; (6)
  $\beta = (\rho_i, \rho_{i-1})(\alpha/\omega_{i-1})$; (7)
  $\mathbf{p}_i = \mathbf{r}_{i-1} + \beta(\mathbf{p}_{i-1} - \omega_{i-1}\mathbf{v}_{i-1})$; (8)
  $\mathbf{v}_i = \mathbf{A}\mathbf{p}_i$; (9)
  $\alpha = \rho_i/(\widehat{\mathbf{r}}_0, \mathbf{v}_i)$; (10)
  $\mathbf{s} = \mathbf{r}_{i-1} - \alpha\mathbf{v}_i$; (11)
  $r = (\mathbf{s}, \mathbf{s})$; (12)
  if $r < \varepsilon$
    $\mathbf{x} = \mathbf{x}_i + \alpha\mathbf{p}_i$; (13)
    quit
  else
    $\mathbf{t} = \mathbf{A}\mathbf{s}$; (14)
    $\omega_i = (\mathbf{t}, \mathbf{s})/(\mathbf{t}, \mathbf{t})$; (15)
    $\mathbf{x}_i = \mathbf{x}_{i-1} + \alpha\mathbf{p}_i + \omega_i\mathbf{s}$; (16)
    $\mathbf{r} = \mathbf{s} - \omega_i\mathbf{t}$; (17)
  end
end

In this work, the BiCGSTAB method was implemented without the use of the preconditioner. For very stiff problems, the use of a preconditioning matrix is essential as the BiCGSTAB method alone would not achieve convergence when $A_t \to 1$ (e.g. water-air mixing).

Parallel solving of elliptic equations

Linear systems of equations which comes from the discretisation of elliptic equations, such as Equation (3.66), bring several issues when it comes to parallel solving. Poisson equations are particularly problematic since the information carried by the flow travels instantaneously across the domain and a change of condition in one part of the domain has an outright influence on the whole flow field. This requires continuous communication among the processors involved in the calculations in order to update each other on the status of the numerical domain. Moreover, the implicit nature of the solution needs the exchange of data to take place a number of times (strictly depending on the type of algorithm employed) at each iteration of the solving process. Therefore, MPI-calls at appropriate points of the code need to be included.
There are two ways with which an elliptic equation can be solved in parallel:

- *Decoupled*: Each processor creates its own linear subsystem of equations which

is solved independently and the communication between the nodes is carried out when every single system has reached a converged solution. After this update, the iterative process starts again until a new solution is reached and so on. This solution-update-new solution routine continues until the boundaries have converged. The main drawback of the decoupled method is the introduction of a delay in the propagation of the information across the domains, with the consequence that a converged solution may not always be found. Moreover there is a sensible increase of the total number of iterations needed and therefore of computational time. For line-by-line relaxation methods, the boundaries of the domains can be updated at the end of each iteration, reducing the delay artificially produced by the solver, but still the problem becomes even more evident and difficult to overcome when many processors are involved in the computation.

- *Coupled*: the processors continuously update each other during every single iteration without introducing any numerical delay on the propagation of the information. This way, the convergence process becomes independent from the number of processors used and it does not differ from the serial case. This requires a higher amount of communication between the processors, with the risk of communication overhead[4], but it is still convenient in terms of time necessary for reaching a converged solution.

The method adopted in this thesis is the latter since it presents clear advantages compared with the former and the amount of processors used for the simulations presented in this thesis was never high enough to cause communication overhead[5].
Splitting the domain over a number of processors implies that each process must be able to exchange data with the neighbouring nodes in order to correctly compute the evolution of the flow field. For this purpose, an 'overlap' Boundary Condition (BC) must be implemented. As an example, let us suppose to split a 6×3 grid in two blocks, or subdomains, along the x-direction. Referring to Figure 3.3, the computational domain Ω is divided into two subdomains Ω_1 and Ω_2 with the creation of ghost-cells g_i (with $i = 1, ..., 6$), where the overlap BC will be applied. The creation of these supplementary cells guarantees that the computations performed on the sub-domains are exactly the same as the original single-block domain Ω and the use of MPI libraries in strategic points of the solver allows the processes to exchange the data among each other.
Considering the case represented in Figure 3.3 and the linear system of equations arising from the discretisation of the pressure equation in two dimensions obtainable by simplifying Equation (3.66):

$$ap_{i+1,j} + bp_{i,j+1} + cp_{i,j} + dp_{i-1,j} + ep_{i,j-1} = \mathrm{b}_{i,j} \,, \tag{3.74}$$

[4]The time required for communications is higher than the time required for the calculations. This can happen for massively parallelised simulations.
[5]The highest number of processors involved in a single simulation was 64.

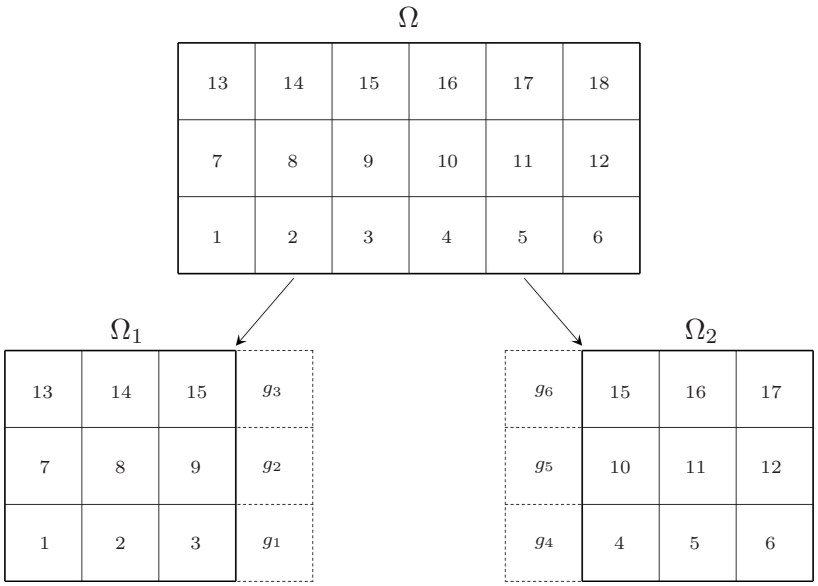

FIGURE 3.3: 6×3 computational grid split into two blocks. The splitting process requires the creation of ghost-cells g_i (with $i = 1, ..., 6$) to allow the communication between the blocks.

the matrix of the coefficients for Ω for the serial case has the following structure:

$$\begin{pmatrix}
c_1 & a_1 & & & & b_1 & & & & & & & & & & \\
d_2 & c_2 & a_2 & & & & b_2 & & & & & & & & & \\
 & d_3 & c_3 & a_3 & & & & b_3 & & & & & & & & \\
 & & d_4 & c_4 & a_4 & & & & b_4 & & & & & & & \\
 & & & d_5 & c_5 & a_5 & & & & b_5 & & & & & & \\
 & & & & d_6 & c_6 & a_6 & & & & b_6 & & & & & \\
e_7 & & & & & d_7 & c_7 & a_7 & & & & b_7 & & & & \\
 & e_8 & & & & & d_8 & c_8 & a_8 & & & & b_8 & & & \\
 & & e_9 & & & & & d_9 & c_9 & a_9 & & & & b_9 & & \\
 & & & e_{10} & & & & & d_{10} & c_{10} & a_{10} & & & & b_{10} & \\
 & & & & e_{11} & & & & & d_{11} & c_{11} & a_{11} & & & & b_{11} \\
 & & & & & e_{12} & & & & & d_{12} & c_{12} & a_{12} & & & \\
 & & & & & & e_{13} & & & & & d_{13} & c_{13} & a_{13} & & \\
 & & & & & & & e_{14} & & & & & d_{14} & c_{14} & a_{14} & \\
 & & & & & & & & e_{15} & & & & & d_{15} & c_{15} & a_{15} \\
 & & & & & & & & & e_{16} & & & & & d_{16} & c_{16} & a_{16} \\
 & & & & & & & & & & e_{17} & & & & & d_{17} & c_{17} & a_{17} \\
 & & & & & & & & & & & e_{18} & & & & & d_{18} & c_{18}
\end{pmatrix},$$

with unknowns and solution vectors respectively:

$$\begin{aligned}
\mathbf{x} &= \{p_1, ..., p_{18}\}, \\
\mathbf{b} &= \{u_1, ..., u_{18}\}.
\end{aligned} \tag{3.75}$$

On the other hand, the correspondent two-block problem presents two separate matrices for Ω_1 and Ω_2:

$$\mathbf{A}_1 = \begin{pmatrix}
c_1 & a_1 & & b_1 & & & & \\
d_2 & c_2 & a_2 & & b_2 & & & \\
 & d_3 & c_3 & a_3 & & b_3 & & \\
e_7 & & d_7 & c_7 & a_7 & & b_7 & \\
 & e_8 & & d_8 & c_8 & a_8 & & b_8 \\
 & & e_9 & & d_9 & c_9 & a_9 & \\
 & & & e_{13} & & d_{13} & c_{13} & a_{13} \\
 & & & & e_{14} & & d_{14} & c_{14} & a_{14} \\
 & & & & & e_{15} & & d_{15} & c_{15}
\end{pmatrix},$$

$$\mathbf{A}_2 = \begin{pmatrix}
c_4 & a_4 & & b_4 & & & & \\
d_5 & c_5 & a_5 & & b_5 & & & \\
 & d_6 & c_6 & a_6 & & b_6 & & \\
e_{10} & & d_{10} & c_{10} & a_{10} & & b_{10} & \\
 & e_{11} & & d_{11} & c_{11} & a_{11} & & b_{11} \\
 & & e_{12} & & d_{12} & c_{12} & a_{12} & \\
 & & & e_{16} & & d_{16} & c_{16} & a_{16} \\
 & & & & e_{17} & & d_{17} & c_{17} & a_{17} \\
 & & & & & e_{18} & & d_{18} & c_{18}
\end{pmatrix}.$$

with unknowns and solution vectors respectively:

$$\begin{aligned} \mathbf{x}_1 &= \{p_1, p_2, p_3, p_7, p_8, p_9, p_{13}, p_{14}, p_{15}\}, \\ \mathbf{b}_1 &= \{u_1, u_2, u_3, u_7, u_8, u_9, u_{13}, u_{14}, u_{15}\}, \end{aligned} \tag{3.76}$$

$$\begin{aligned} \mathbf{x}_2 &= \{p_4, p_5, p_6, p_{10}, p_{11}, p_{12}, p_{16}, p_{17}, p_{18}\}, \\ \mathbf{b}_2 &= \{u_4, u_5, u_6, u_{10}, u_{11}, u_{12}, u_{16}, u_{17}, u_{18}\}. \end{aligned} \tag{3.77}$$

Note that the coefficients for the two dimensional case do not follow their three dimensional definition reported in (3.67), (3.68) and (3.69), but they need to be modified accordingly to the reduced number of dimensions.
The issue which arises from the splitting of the domain can be understood by comparing the linear problem defined for cell 9 in the single-block and two-block case. The correct solution is represented by the former case:

$$a_9 p_{10} + b_9 p_{15} + c_9 p_9 + d_9 p_8 + e_9 p_3 = \mathrm{b}_9 \ . \tag{3.78}$$

In the split problem, the cell number 9 belongs to Ω_1 and here both the pressure p_{10} and the coefficient a_9 are not available since they are defined in cell 10, which is part of Ω_2. Therefore, the creation of the halo cells g_i in Figure 3.3 allows to recover the stencil required by the linear problem and makes the storage of the data coming from the neighbouring blocks possible. For the test case considered, the conditions:

$$\begin{aligned} g_1 &= 4, \\ g_2 &= 10, \\ g_3 &= 15, \\ g_4 &= 3, \\ g_5 &= 9, \\ g_5 &= 15, \end{aligned} \tag{3.79}$$

create an effective connection between the blocks allowing the coupled parallel solution of the system. The update through the MPI calls is done only for the ghost cells, which are not considered for the computation of the final solution. The same concepts here explained apply when the domain is split along the y and/or z direction for three dimensional cases.

Fully coupled BiCGSTAB

Considering the issues presented in the previous section, it is necessary to identify the points along the algorithm where the processors involved in the simulation need to exchange the data and update the ghost cells. Going through the BiCGSTAB method presented on page 47, there are two main points where communication is required:

- When a matrix-vector product is calculated, i.e. lines (2), (9) and (14). In these cases the processors exchange the information about the flux through the ghost cells, avoiding the production of artificial delay in the transmission of the information across the boundaries between blocks;

- When inner products for the coefficients ρ_i, α, ω_i and the residual r are computed, i.e. lines (6), (10), (15) and (12). These parameters in fact are defined on a global level. Following the definition of inner product:

$$(\mathbf{x}, \mathbf{y}) = \sum_{i=1}^{N} x_i y_i \tag{3.80}$$

  each processor calculates the partial inner product resulting from the cells which belong to the subdomain it was assigned. Successively, all the partial inner products are gathered and summed, thus obtaining the sought global value which is broadcasted back to all the processors.

3.5.4 Storage of the matrix of the coefficients

Another important issue arising from the linear problem due to the discretisation of the pressure equation (3.58) is the storage requirements of the matrix of the coefficients $\mathbf{A}$. Considering N as the number of the computational cells in the domain, the dimension of $\mathbf{A}$ is $N \times N$. Given an array of $\mathcal{N}$ elements, the amount of memory required for its storage is given by the following:

$$\text{Memory} = \frac{\mathcal{N} \times t}{1024^2} \text{ [MB]} , \tag{3.81}$$

where $t = 8$ if the elements of the array are real or $t = 4$ if they are integers. In Table 3.1, the formula was used to calculate the memory required by the matrix of the coefficients, with $\mathcal{N} = N^2$. Different grid sizes which can be found in three dimensional calculations were considered.

Number of elements	Memory required [MB]
10^4	7.63×10^2
10^5	7.63×10^4
10^6	7.63×10^6
10^7	7.63×10^8
10^8	7.63×10^{10}

TABLE 3.1: Memory requirements for the storage of an array of real numbers of different dimensions calculated with Equation (3.81).

It is possible to realise that the amount of memory scales quadratically with the number of elements of the array and that fulfilling the demand of memory is already impossible for a grid with 10^5 cells. A solution to the problem is found by taking into consideration that, in Equation (3.66), $\mathbf{A}$ is a banded matrix with five (two dimensional cases) or seven (three dimensional cases) diagonals. This structure implies that the number of zeros in the matrix is much higher than the non-zero elements, therefore it is possible to store the matrix in a much more efficient way if all the numbers out of the diagonals are not considered. The number of non-zero elements for each row are known and they equal the number of diagonals. Therefore, the dimension of the array containing only

the bands is $Z \times N$ (where Z represents the number of diagonals of the matrix) and not N^2. Equation (3.81) is modified as follows:

$$\text{Memory} = \frac{ZN \times t}{1024^2} \text{ [MB]} . \tag{3.82}$$

As it is possible to see from Table 3.2, storing only the bands of the matrix is potentially a great improvement.

Number of elements	Memory required [MB]	Memory saved [%]
10^4	5.34×10^{-1}	99.931
10^5	5.34×10^{0}	99.990
10^6	5.34×10^{1}	99.999
10^7	5.34×10^{2}	>99.999
10^8	5.34×10^{3}	>99.999

TABLE 3.2: Memory requirements for the storage of the seven bands of **A** for Equation (3.82) and memory saved compared to Equation (3.81) for different grid dimensions.

In this case the memory required is sensibly lower and it scales with the same order of magnitude of the number of elements.
Following from this alternative storage method, some of the operations involved in the BiCGSTAB method need to be modified accordingly. Particular attention is required in those points of the algorithm where matrix-vector multiplications are computed, i.e. lines (2) (9) and (14). In standard algebra the matrix-vector product is defined by:

$$p_i = \sum_{i=1}^{N} a_{i,j} x_j , \tag{3.83}$$

with the consequence that the position of the various elements $a_{i,j}$ inside the matrix **A** is of fundamental importance. Using the new storage method does not allow to directly apply the formula (3.83) as the position of the elements changes. In order to explain the new method, the two dimensional case is taken into consideration. The extention to three dimensions is immediate. The structure of **A** for a 2D problem is the following:

$$\begin{array}{c} \\ R1 \\ R2 \\ \vdots \\ RN_x \\ \vdots \\ \vdots \\ \vdots \\ \vdots \\ \vdots \\ RN \end{array}
\begin{array}{c}
\begin{array}{ccccccccccc} C1 & C2 & \dots & CN_x & \dots & \dots & \dots & \dots & \dots & CN \end{array} \\
\left(\begin{array}{ccccccccccc}
D3_1 & D4_1 & & D5_1 & & & & & & \\
D2_2 & \ddots & \ddots & & \ddots & & & & & \\
 & \ddots & \ddots & \ddots & & \ddots & & & & \\
D1_{N_x} & & \ddots & \ddots & \ddots & & \ddots & & & \\
 & \ddots & & \ddots & \ddots & \ddots & & \ddots & & \\
 & & \ddots & & \ddots & \ddots & \ddots & & \ddots & \\
 & & & \ddots & & \ddots & \ddots & \ddots & & D5_{N-N_x} \\
 & & & & \ddots & & \ddots & \ddots & \ddots & \\
 & & & & & \ddots & & \ddots & \ddots & D4_{N-1} \\
 & & & & & & D1_N & & D2_N & D3_N
\end{array}\right)
\end{array} .$$

First, the elements belonging to the diagonals $D1 - DZ$ of $\mathbf{A}$ are stored in a vector $\widehat{\mathbf{A}}$, which has consequently dimension ZN. The storage is done sweeping firstly through the columns of the matrix and then through the rows:

$$\widehat{\mathbf{A}} = \{D1_1, ..., DZ_1, D1_i, ..., DZ_i, D1_N, ..., DZ_N\} \, . \tag{3.84}$$

As it is possible to notice, some diagonals are missing some elements (e.g. $D1_1$, $D1_2$, $D1_3$, $D2_1$, etc), which can all be replaced by zeros.
The second step is to consider that it is necessary to map the elements of $\widehat{\mathbf{A}}$ in the original matrix $\mathbf{A}$ to be able to calculate the matrix-vector product. This can be achieved by creating an extra vector $\mathbf{f}$ of the same dimensions of $\widehat{\mathbf{A}}$. Following the same sweeping order adopted for building $\widehat{\mathbf{A}}$, the number of the column in which the non-zero elements $\widehat{a}_i$ are positioned in the original matrix is assigned to each f_i. Therefore, applying this to the example $\mathbf{f}$ becomes:

$$\begin{aligned} \mathbf{f} = \{ & \underbrace{0, 0, 1, 2, N_x}, \quad \underbrace{0, 1, 2, 3, N_x + 1} \quad , ..., \quad \underbrace{N-2, N-1, N, 0, 0}\} \, , \\ & \text{Column numbers of the non-zero elements of R1} \quad \text{Column numbers of the non-zero elements of R2} \quad \text{Column numbers of the non-zero elements of RN} \end{aligned} \tag{3.85}$$

The elements of the diagonals not comprised in the matrix are once again replaced by zeros. The last information that is needed to be taken into account in order to be able to redefine the matrix-vector product is the number of non-zero elements, Z, contained in each row of $\mathbf{A}$. Having at disposal $\mathbf{f}$ and Z, allows to map $\widehat{\mathbf{A}}$ onto $\mathbf{A}$ and therefore it is possible to define a new matrix-vector product which suits this storage method:

$$p_j = \sum_{i=1}^{Z} \widehat{a}_{Z(j-1)+i} \cdot x_{f_{Z(j-1)+i}} \, . \tag{3.86}$$

In conclusion, the amount of memory needed to store $\widehat{\mathbf{A}}$ has to be increased in order to take into account also the memory required by $\mathbf{f}$, which is a vector of integers. The improvements in terms of memory requirements brought by this method in comparison with the storage of the full matrix of the coefficients are reported in Table 3.3.

Number of elements	Storage of $\widehat{\mathbf{A}}$ and $\mathbf{f}$ [MB]	Memory saved [%]
10^4	8.01×10^{-1}	99.895
10^5	8.01×10^{0}	99.990
10^6	8.01×10^{1}	99.999
10^7	8.01×10^{2}	>99.999
10^8	8.01×10^{3}	>99.999

TABLE 3.3: Memory requirements for storing the vector of the coefficients $\widehat{\mathbf{A}}$ plus the vector $\mathbf{f}$ compared against the space needed for the full original matrix $\mathbf{A}$.

The use of this algorithm gives another advantage apart from the lower memory requirement. Since the operations are carried out only for the elements of the diagonals, the computation time is sensibly speeded-up.

The BiCGSTAB algorithm is adapted to the new formulation just by appropriately substituting the sum (3.86) to (3.83) in lines (2), (9) and (14) of the algorithm without any other change.

3.6 Multi-component model

Richtmyer-Meshkov instability needs the presence of two fluids in order to manifest itself, therefore a method which keeps track of the species propagation across the numerical field is required. Here, the fluids are supposed to be miscible and the tracking-method employed is mixture-based, which consists in adding $S-1$, with S number of species, advective equations for passive scalars q_i $(1 \leq i \leq S-1)$ to the systems Equation (3.7) and Equation (3.13):

$$\frac{\partial q_i}{\partial t} + \frac{\partial (u q_i)}{\partial x} + \frac{\partial (v q_i)}{\partial y} + \frac{\partial (w q_i)}{\partial z} = 0 \, . \tag{3.87}$$

These equations can be casted in different terms (e.g. density, mass fraction, volume fraction etc.) depending on the nature of the problem. For a two-fluid model, only one advection equation is needed to close the system. In the compressible flow model, if the fluids present the same values of γ and C_v (specific heat at constant volume), the additional transport equation is casted in terms of density multiplied by volume fraction, $q = \rho V_f$, where the latter is defined as the ratio of volume of a given fluid, V_i to the total volume of the cell:

$$V_f = \frac{\mathrm{V}_1}{\mathrm{V}_1 + \mathrm{V}_2} \, . \tag{3.88}$$

The volume fraction is bounded between the values of 0 (no fluid one inside the cell) and 1 (only fluid one inside the cell). Values between 0 and 1 indicate that a mixture of fluid one and fluid two is present inside the cell.
For the incompressible model, the transport equation is casted in terms of total density $\rho_{\mathrm{I}} = (\rho_1)_{\mathrm{I}} + (\rho_2)_{\mathrm{I}}$. The change of variable is due to the fact that in the compressible model, the volume fraction is just an artifact which allows to keep track of the species propagation without playing an active role in the model. The system Equation (3.7) is already closed and no additional equation is needed. On the contrary, the variable-density nature of the flow implies that the distribution of ρ_{I} due to the mixing of the fluids is no longer known when the fluids are incompressible, therefore an additional equation in order to close the system Equation (3.13) must be included. In this case, the transport equation is casted in terms of total density instead of volume fraction. This is the most efficient choice for two reasons: ρ_{I} is unknown and in addition it gives information about the propagation of the fluids. In fact, the densities of the two incompressible pure fluids $(\rho_1)_{\mathrm{I}}$ and $(\rho_2)_{\mathrm{I}}$ are assigned and they remain constant in both time and space. Therefore, it is possible to determine the portion of fluid 1 or of fluid 2 present inside a cell during the post-processing phase using the volume fraction:

$$(V_f)_i = \frac{\rho_i - (\rho_1)_{\mathrm{I}}}{(\rho_2)_{\mathrm{I}} - (\rho_1)_{\mathrm{I}}} \, . \tag{3.89}$$

Formally, casting the transport equation in terms of V_f also in the incompressible model is correct but it is not strictly needed, since the volume fraction would be used to calculate the distribution of density in order to solve the momentum equations.

4

Incompressible modelling of RMI

Synopsis

As Richtmyer did in his first analysis, RMI can be also treated as a pure incompressible phenomena. From a numerical point of view, the incompressible instability can be caused by using either an impulse of velocity or a pulse of gravity. In view of hybrid simulations, it is important to address the behaviour of the incompressible Riemann-solvers when they are used in conjunction with the high resolution methods presented in Chapter 3. For this purpose, both triggering methods are tested. Data against which the numerical results are compared are provided by the literature, where different authors carried out numerical simulations and experiments on the incompressible version of the instability using the falling tank technique. The initial conditions for the fluids are provided in the papers as well as parameters which characterise the impulse or the acceleration imparted to the fluids. Pressure convergence and grid-convergence tests of the solver are left to Appendices A and B respectively.

Much of the work in this chapter will be presented in:
T.Oggian, D.Drikakis, D.L. Youngs and R.J.R. Williams, 'Numerical uncertainty in incompressible, variable-density flows due to reconstruction schemes and Riemann solvers'.

4.1 Generation of the initial impulse

The incompressible version of the Richtmyer-Meshkov instability substitutes the incident shock wave with an impulse of velocity. From a numerical point of view, the acceleration can be generated in two different ways. The first method uses the linear analysis to derive an initial velocity field that is then applied to the interface between the fluids which is supposed to be flat. The baroclinic vorticity is already included in the imposed initial velocity distribution. The work of Fraley (1986) laid the foundations for the production of well-posed incompressible initial conditions for numerical simulations. Supposing that the shock wave travels along the x-direction, the author analytically demonstrated that, contrarily to the compressible case where the solution of the perturbation decays as $\sim x^{-1/2}$ away from the interface for strong shocks and as $\sim x^{-3/2}$ for weak shocks, in the incompressible case it decays as $\sim e^{-k|x|}$. From linear analysis of the governing equation and assuming incompressible, inviscid and irrotational fluid, the initial impulse along the x-direction is described by the following velocity potential (Drazin and Reid, 2004):

$$\phi(x,y) = s(x)A(k)\phi_0 sin[ky + \varphi(k)]e^{-k|x|} \,. \tag{4.1}$$

Supposing that the interface is located at $x = 0$,

$$s(x) = \begin{cases} 1 & \text{if} \quad x > 0 \\ -1 & \text{if} \quad x < 0 \end{cases} , \tag{4.2}$$

and $\phi_0 = A^+ \Delta u$ represents the magnitude of the initial perturbation. $A(k)$ is a coefficient that compensates the finite length of the domain as it nullifies the x-velocity component at the boundaries

$$A(k) = \begin{cases} \dfrac{1 - e^{-2k(h_l + x)}}{1 - e^{-2kh_l}} & if \quad x < 0 \\ 1 & if \quad x = 0 \\ \dfrac{1 - e^{-2k(h_h - x)}}{1 - e^{-2kh_h}} & if \quad x > 0 \end{cases} , \tag{4.3}$$

Here, h_l and h_h are the lengths of the domain along the x direction occupied by the light and heavy fluid respectively. The velocity components are recovered by applying:

$$u = \frac{\partial \phi}{\partial x} \,, \tag{4.4}$$

$$v = \frac{\partial \phi}{\partial y} \,. \tag{4.5}$$

The vector field generated by Equation (4.1) is shown in Figure 4.1. Here it is possible to observe the two vortexes generated by the baroclinic vorticity which, in the compressible RMI, is deposited by the incident shock.
The alternative way of triggering the incompressible instability is to replicate the acceleration pulse, to which the falling box is subjected when it bounces off of the springs,

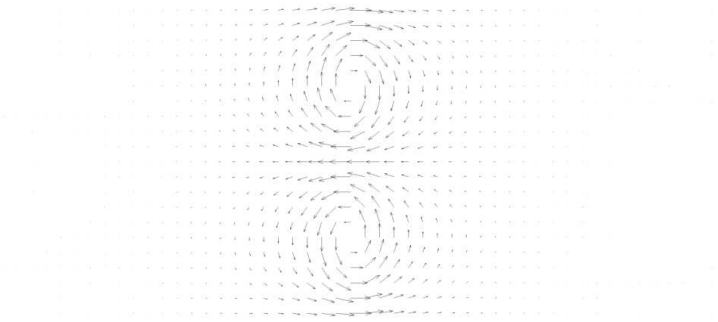

FIGURE 4.1: Baroclinic vorticity generated by the initial velocity impulse from Equation (4.1) applied to a grid with 60×21 cells.

within the simulations. This requires the addition of a source term to the incompressible Euler equations:

$$\begin{cases} \dfrac{\partial u}{\partial x} + \dfrac{\partial v}{\partial y} + \dfrac{\partial w}{\partial z} = 0 \\ \dfrac{\partial \mathbf{U}_\mathrm{I}}{\partial t} + \dfrac{\partial \mathbf{E}_\mathrm{I}}{\partial x} + \dfrac{\partial \mathbf{F}_\mathrm{I}}{\partial y} + \dfrac{\partial \mathbf{G}_\mathrm{I}}{\partial z} = -\nabla p + \rho \mathbf{g} \end{cases} , \tag{4.6}$$

where $\mathbf{g} = \mathbf{g}(t)$ is the measured gravity force and $\mathbf{U}_\mathrm{I}$, $\mathbf{E}_\mathrm{I}$, $\mathbf{F}_\mathrm{I}$ and $\mathbf{G}_\mathrm{I}$ are defined by the system (3.13). The inclusion of volume force in the model also requires a modification to the wall boundary condition, as the hydrostatic equilibrium must be respected along the direction of the impulse x:

$$\frac{dp}{dx} = -\rho g \, . \tag{4.7}$$

The value of $\mathbf{g}(t)$ is interpolated from the experimental measurement since an accelerometer is always positioned on the falling box in order to record the acceleration and the impulse to which the tank is subjected to. The interface between the fluids is not flat as it was in the previous initialisation but it needs to be shaped accordingly through the initial condition for the density field. In this chapter, both methods are tested and verified against experimental results and numerical simulations.

4.2 Impulsive initial condition

The single-mode impulsive RMI where the initial velocity field is given by Equation (4.1) is the test case chosen in order to explore the capabilities of the incompressible algorithm. The simulations are compared against experiments by Niederhaus and Jacobs (2003). For completeness, a brief description of the experimental approach is reported.

4.2.1 Experimental rig

Niederhaus and Jacobs (2003) used the falling-tank technique of Jacobs and Sheeley (1996) to trigger the instability. The tank had dimensions of $0.2544 \times 0.1199 \times 0.0508$ m and it was attached to a three meter high vertical rail system. The experiment starts

by releasing the box from the top of the tracks and let it fall freely without any external disturbance until it bounces off a system of springs, which imparts an impulsive upward acceleration (see Figure 4.2).

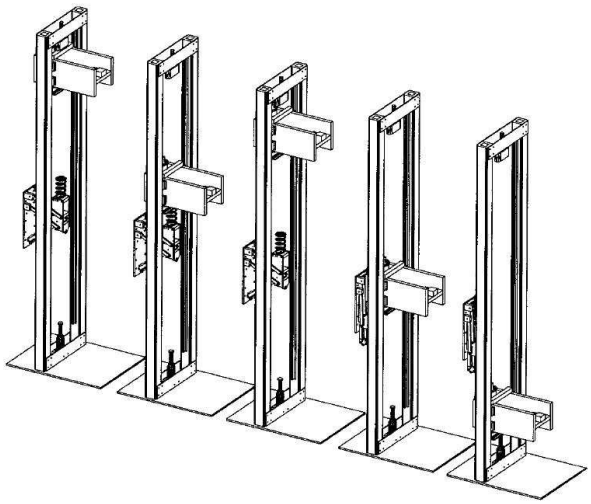

FIGURE 4.2: Sequence of the tank falling along the vertical rails (Niederhaus and Jacobs, 2003).

The fluids employed in the experiments are a mixture of water/calcium nitrate, which constitutes the heavy fluid, and a mixture of water/isopropanol. The resulting Atwood number is 0.1587, with $\rho_h = 1202.5$ Kg/m^3 and $\rho_l = 873.1$ Kg/m^3. The media are perfectly miscible and therefore no surface tension is present. The initial perturbation is obtained by oscillating the tank horizontally at the desired frequency, producing $n + 1/2$ standing internal waves, with n bounded between 0 and 4.
The technique employed for the visualisation of the motion field is the Planar Laser-Induced Fluorescence (PLIF), where a laser sheet illuminates the centre of the tank. Disodium fluorescein is added to the heavy fluid to obtain a clear distinction of the density field illuminated by the laser. The images of the mixing zone were obtained using a CCD camera with a resolution of 640×480 pixels at 60Hz.

4.2.2 Numerical set-up

The two-dimensional single-mode test case considered is derived from the experiments and it consists of a rectangular domain of dimensions 0.24×0.08 m. The grid resolution used to verify the behaviour of the various Riemann-solvers and high-resolution schemes considered is 160×496 cells, which allows to obtain a converged solution (see Appendix B). The magnitude of the initial impulse, $\dot{a}_0$, is obtained from the recorded acceleration history of the falling tank. The triangular impulse imparted by the springs (Figure 4.3) has a duration of 26 ms and a peak magnitude of 50 g, which results in $\dot{a}_0 = 0.225$ m/s. Since the growth of a single and constant wavelength is computed, the boundary conditions along the x-direction are periodic and slip walls along y-direction are imposed due the inviscid nature of the simulation.
The explorative purpose of the test case required the use of all the three Riemann solvers presented in §3.5.1: LF, RU and HLL. Each flux is employed in conjunction

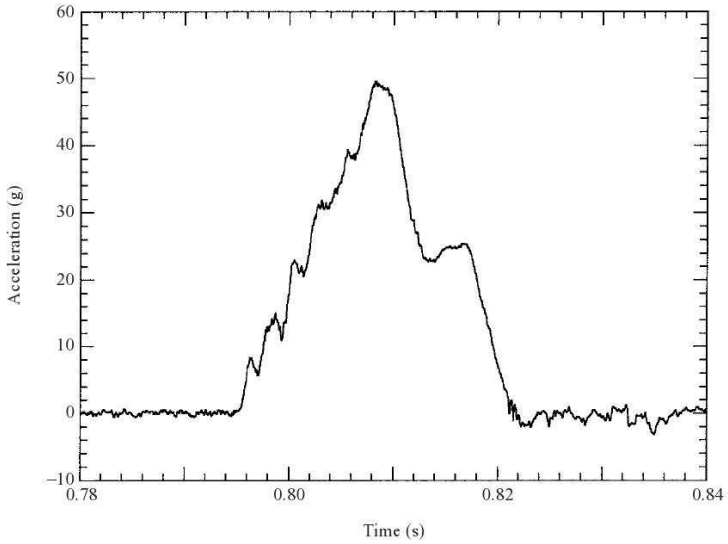

FIGURE 4.3: Acceleration history imparted to the falling tank by the springs (Niederhaus and Jacobs, 2003).

with each of the five different high resolution methods presented in §3.4.2: M2, M3, M5, W5, W9. The time marching scheme is the standard RK third-order accurate and Δt is computed at each time-step depending on the CFL number, $C = 0.5$. The residual for the pressure was set to 1.0×10^{-4} in accordance with the pressure-convergence test, which is reported in Appendix A.
Due to the complexity of the phenomenon, obtaining local measurements of the flow field during the experiments is not possible and the only data which are available from the practical tests is the growth of the mixing zone, of the bubbles and of the spikes in time, respectively a, h_b and h_s. The spikes are defined as the portions of heavy fluid penetrating the light fluid and, conversely, the bubbles are defined as the portions of light fluid penetrating the heavy fluid. Both variables are measured along the x-direction from the initial position of the interface to the extreme points on the domain where the volume fraction has a value of 0.5. The amplitude of the perturbation is defined as the average between the height of the spikes and the height of the bubbles. In order to compare this parameter with the experimental data, a is multiplied by the wave-number of the perturbation:

$$ka = k\left(\frac{h_b + h_s}{2}\right) . \tag{4.8}$$

4.2.3 Effect of the reconstruction scheme

Even though the incompressible method is limited to an overall second-order of accuracy in space, it is of interest to address the behaviour of the different numerical schemes for the fluxes reconstruction.
Considering the growth of the instability ka, in Figure 4.4 it is possible to see how M2, M3, M5, W5 and W9 perfectly agree on its evolution since all the lines are substantially superposed one over the other. The marginal difference which can be noticed is given by the Riemann-solver. In particular, RU appears to be the most consistent method

as it is not possible to distinghish the single lines as they lay on top of each other (Figure 4.4b). On the other hand, the broadest distribution of results is given by LF (Figure 4.4a), even though it needs to be pointed out that the biggest discrepancy presents a very small relative error of 1.91% (between M2 and W9 at $k\dot{a}_0 t = 25$). This outcome was somehow expected, since this method for the computation of the fluxes is not actually a proper Riemann-solver. In fact, the formulation of LF (3.52) closely resembles the Rusanov variant (3.53), where the wave-speed is replaced by the CFL stability condition $S = C\Delta x/\Delta t$, with $C = 1$. This makes the LF flux the most dissipative and less accurate method among the three schemes employed and therefore the most sensitive to the order of accuracy with which variables are reconstructed at the interface between cells. Finally, the HLL solver is collocated in between LF and RU since the envelope of the solutions given by the reconstruction scheme is visibly reduced with respect to LF but not as narrowed as for RU (Figure 4.4c). The reason of this can be attributed to the fact that the HLL solver consider a two-wave Riemann fan which is somehow needless, since for incompressible flows there is only one wave only.

4.2.4 Comparison with experiments

Integral quantities

Figure 4.5 shows the integral quantities for the reconstruction schemes M2, M3, M5, W5 and W9 (see §3.4.2, page 37). Here, the envelope traced by the grey solid lines represents the range of values obtained from the experimental tests. From the graphs, it is possible to see how the parameters are included within the range of the experimental values provided by Niederhaus and Jacobs (2003) for almost all the combinations tested. The only exception is done for HLL+M5, which at late-time predicts a slightly higher value of kh_s (Figure 4.5e), resulting in an overestimation of the total growth of the instability at late-time ka (Figure 4.5f). Apart from this particular case, excellent agreement is found between computations and experiments for this test case from a quantitative point of view. The predicted growth of the instability is collocated in the higher part of the envelope, indicating higher mixing than the average of the experimental values. This seems to be due to a higher growth of the spike at late-times since kh_b tends to lie closer to the central part of the envelope.
Considering the differences among the trends computed by the various reconstruction method, it is possible to always notice from the graphs that the evolutions of kh_s, kh_b and ka in time are consistent and very good matching of the solutions is noticeable as well. The cases where the best agreement is found are the ones where W9 and M3 are employed. Here, the biggest discrepancy between the fluxes (LF and HLL) occurs for kh_b at late-times and it is less than 1% at $k\dot{a}_0 t = 25$. On the other hand, it is possible to observe that the least consistent method among those tested is M5 since kh_s computed by LF+M5 and HLL+M5 presents a difference of 2.5% at $k\dot{a}_0 t = 25$.

Qualitative comparison

A visual comparison between the instability predicted by the numerical simulations and the flow field photographed during the experiments is necessary in order to give an interpretation of the trends presented in the previous paragraph. Contour plots of

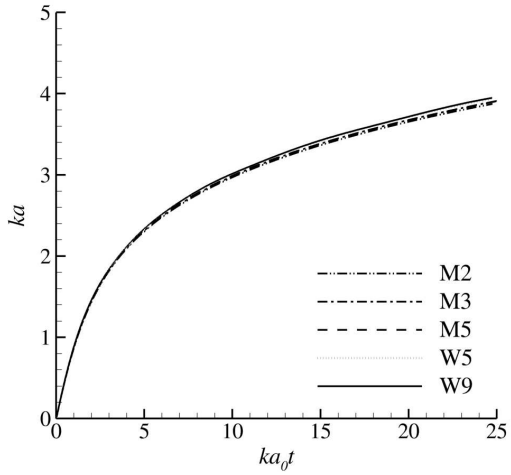

(a) LF

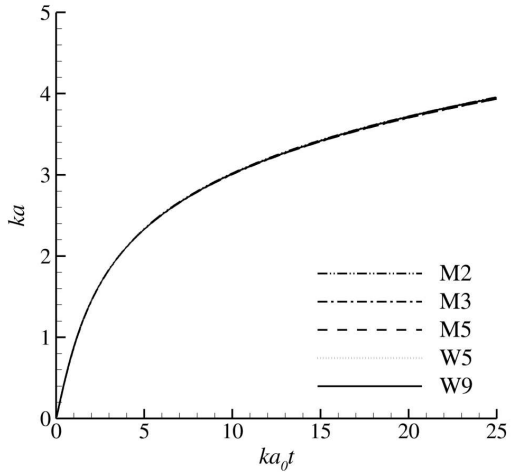

(b) RU

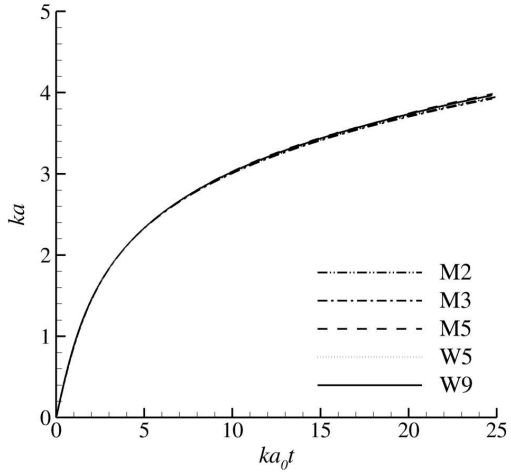

(c) HLL

FIGURE 4.4: Normalised growth of the instability according to the tested reconstruction schemes.

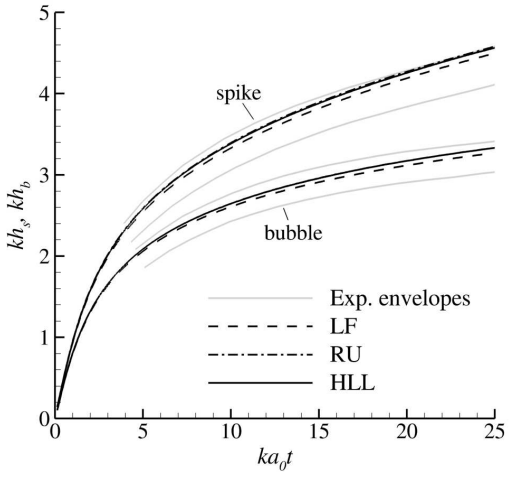

(a) M2: Spikes and bubbles growth

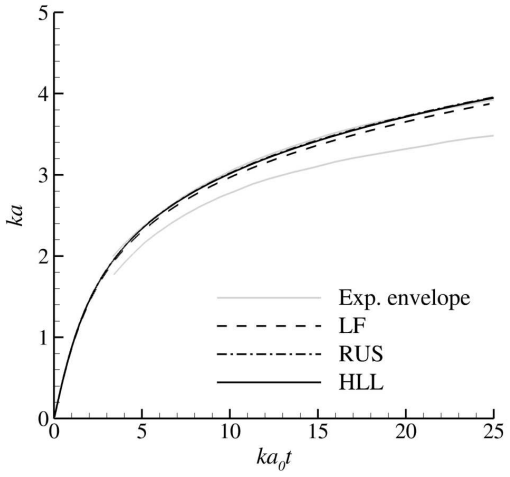

(b) M2: Growth of the mixing zone

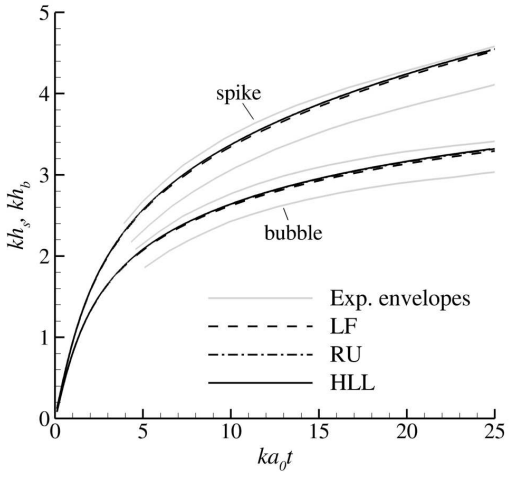

(c) M3: Spikes and bubbles growth

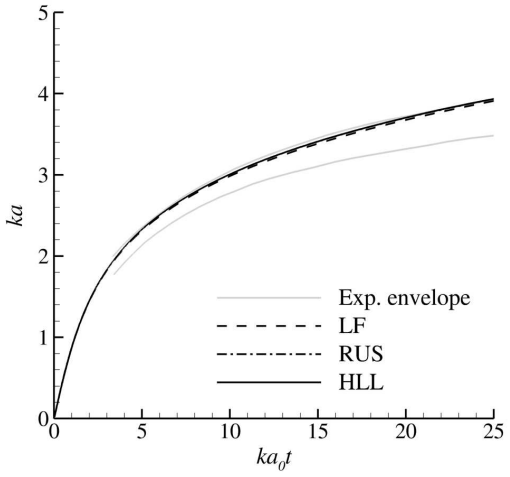

(d) M3: Growth of the mixing zone

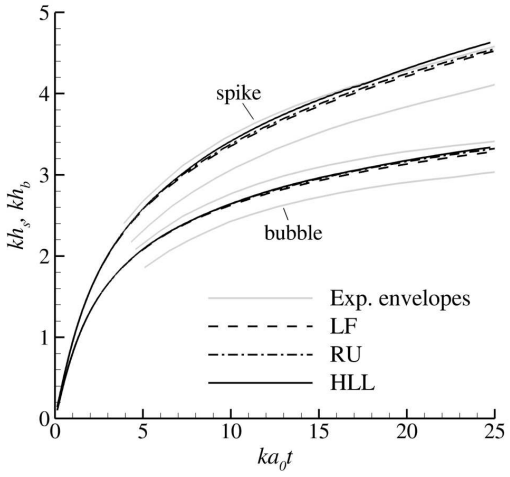

(e) M5: Spikes and bubbles growth

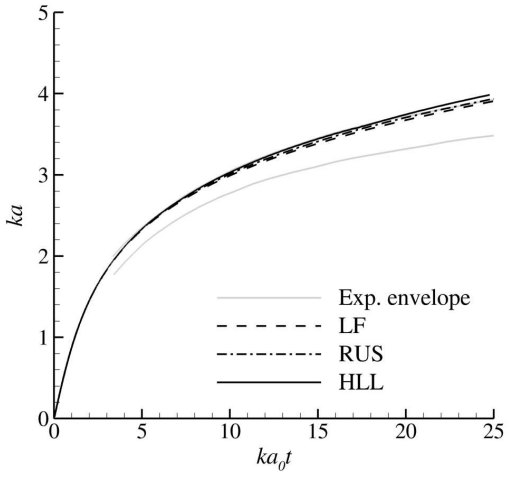

(f) M5: Growth of the mixing zone

FIGURE 4.5: Integral quantities computed according to M2 compared with experimental envelope.

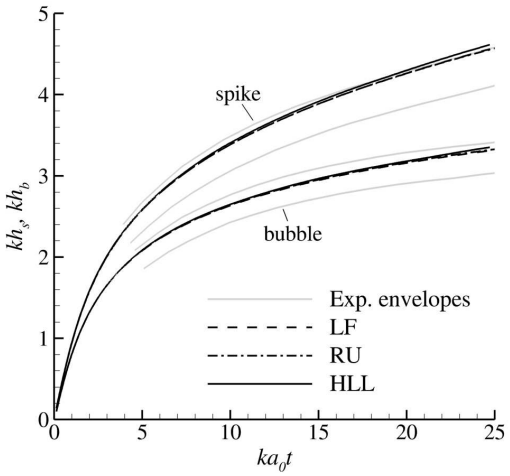

(g) W5: Spikes and bubbles growth

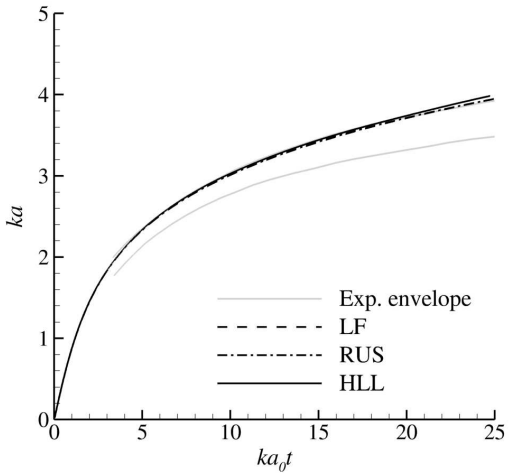

(h) W5: Growth of the mixing zone

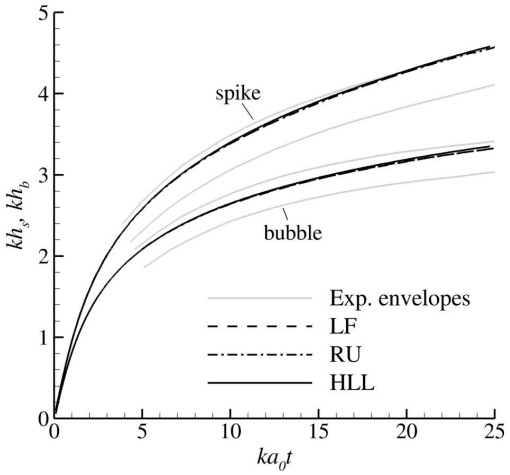

(i) W9: Spikes and bubbles growth

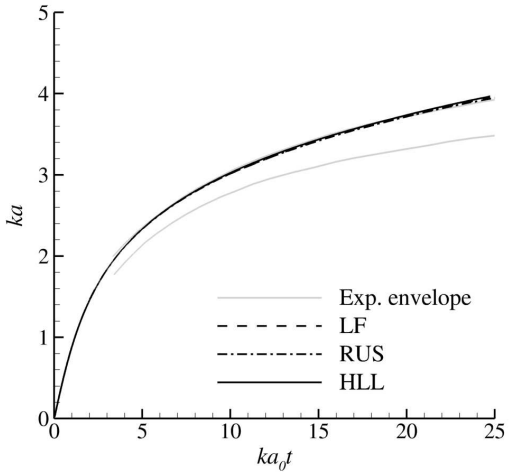

(j) W9: Growth of the mixing zone

FIGURE 4.5: *(continued).*

the numerical density field together with the experimental PLIF image are shown in Figure 4.6. The images refer to $t \approx 900$ ms.

At this moment in time, the typical mushroom-shape of RMI is very well developed and the two big coherent structures are clearly observable on the sides of the mushroom. The general shape and proportions look very similar in all the snapshots and the main difference which can be noticed lies on the look of the roll-ups. A cross-comparison between the different flux schemes shows clearly the different amount of numerical dissipation which each of them provides. The worst flux in this sense is the LF. In fact, for a given reconstruction scheme, the appearance of the side vortexes is the least sharp and least defined, despite the fine grid resolution. On the contrary, HLL flux gives the best defined roll-ups. RU lies in between LF and HLL since it captures the features better predicted by HLL than LF. As a direct consequence of the different amount of the dissipation given by the Riemann-solvers, the details of the structures that are

(a) PLIF image of the flow-field from Niederhaus and Jacobs (2003).

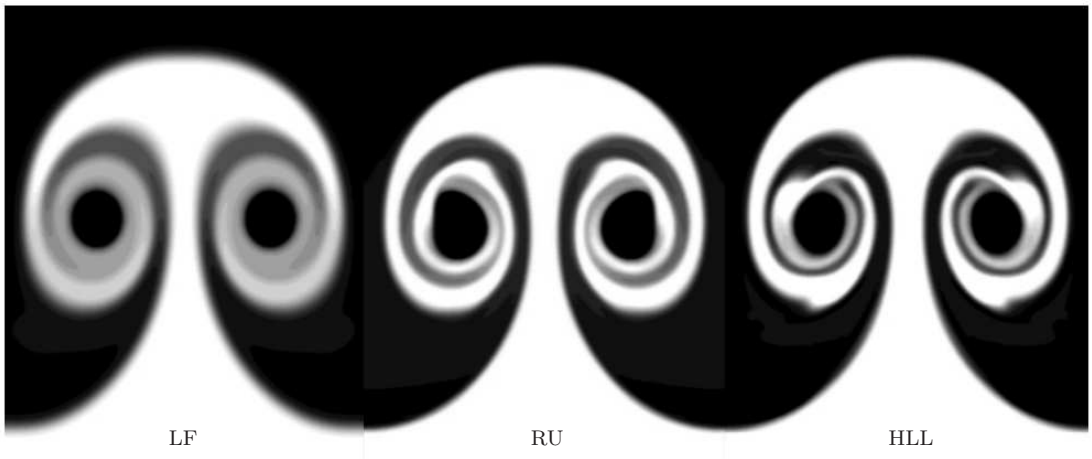

(b) M2

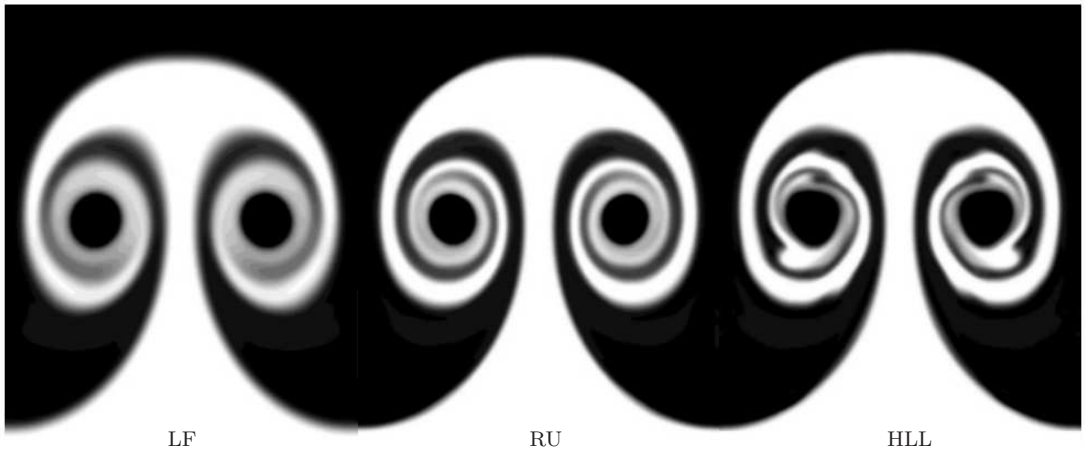

(c) M3

FIGURE 4.6: Comparison between PLIF image of the instability from Niederhaus and Jacobs (2003) (top figure) and the density contours of the numerical field obtained from the simulations at $t \approx 900$ ms. The snapshots from the simulations are rotated for clearer comparison. From the top to the bottom of each row, the mushrooms are computed with: M2, M3, M5, W5 and W9, whereas from left to right the fluxes employed are LF, RU, HLL.

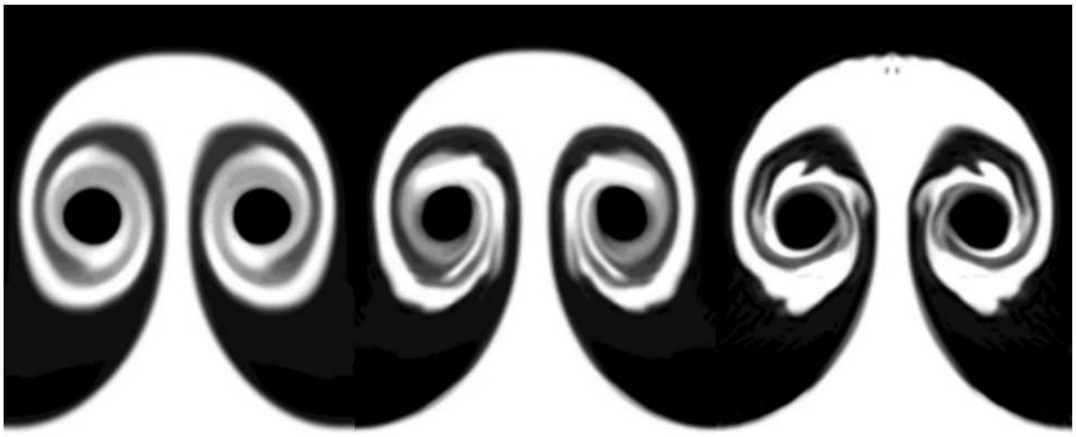

LF RU HLL
(d) M5

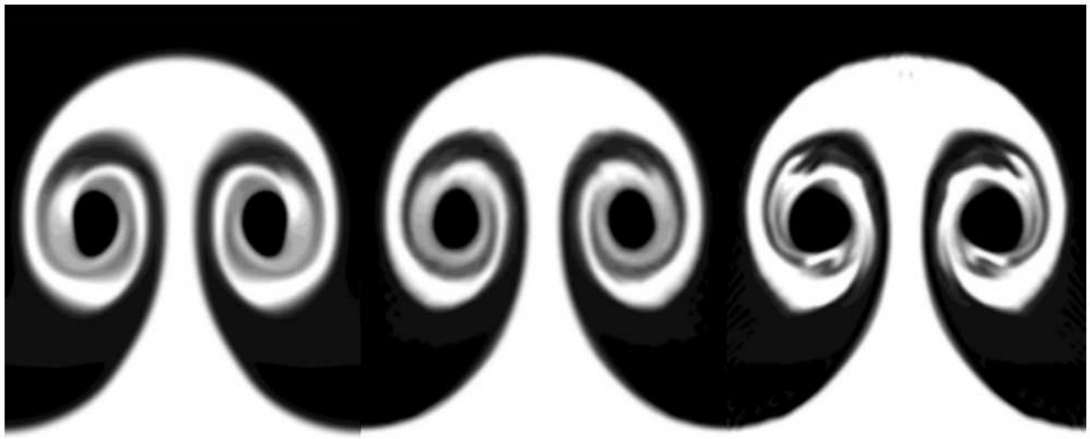

LF RU HLL
(e) W5

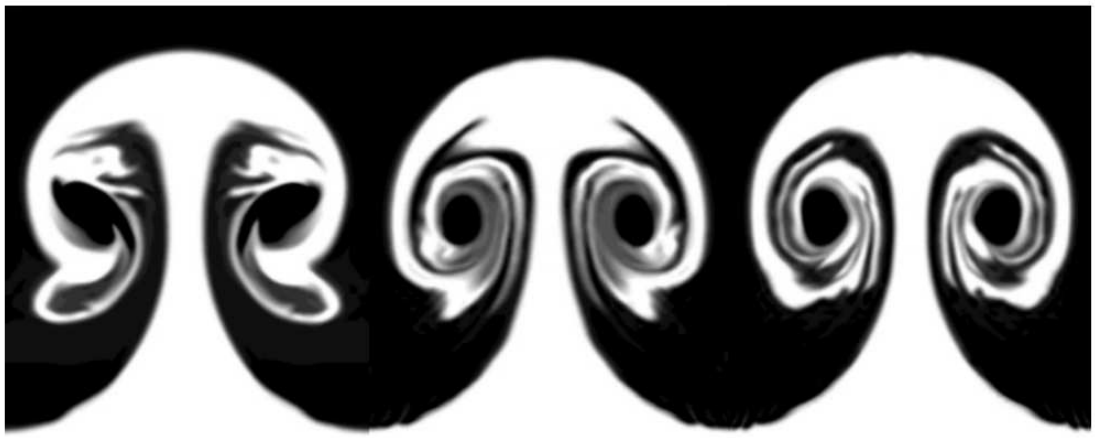

LF RU HLL
(f) W9

FIGURE 4.6: *(continued).*

captured increase from LF to HLL.
The mushrooms can also be compared from the point of view of the reconstruction scheme employed. Similar considerations can be drawn. Increasing the order of accuracy of the reconstruction at the cell interfaces (i.e. reducing the amount of dissipation provided by the numerics) results in a better capability of the solver in capturing fine-scales structures. Independently from the Riemann-solver employed, the level of the details provided by the code, varying from the least (M2) to the most (W9) accurate reconstruction schemes, is higher and higher and the roll-ups become sharper.
It needs to be pointed out that less numerical dissipation, thus more details and sharper interface between the fluids, does not imply that the solution reflects the reality. In fact, comparing the snapshots obtained from the simulations against the PLIF image from Niederhaus and Jacobs (2003) (Figure 4.6a) reveals that the numerical schemes can capture structures and flow-features that are not present in the reality. In these terms, the best example is given when LF flux and W9 reconstruction scheme are used together (leftside of Figure 4.6e). Here, even though the external edge of the mushroom closely resembles the reality, the zone in which the roll-ups are supposed to develop is not correctly reproduced by the simulation, where these features look as if they broke up. Remarkable differences can be noticed in almost all the combinations between fluxes and reconstruction schemes, with an exception made for the most dissipative ones (M2 and M3 with LF or RU). The snapshot which resembles the experiments more closely is given by the coupling RU+M3 (central mushroom in 4.6c). Here in fact, the roll-ups are more defined and regular than the other simulations, although the number of close-ups is inferior.

4.2.5 Considerations

From the results presented, some considerations need to be done before proceeding further. Looking at the trend of the integral quantities, the schemes are found in very good agreement with the experiments. Supposing the correct solution to lie around the centre of the experimental envelope, a slight overestimation of the spike growth is present at late-times. The explanation for this lies in the fact that the numerical simulations do not correctly capture the roll-ups at the sides of the mushroom, since the number of the close-ups of the vortexes detected in the experiments is higher than the value computed by the simulations. These structures directly influence the growth of the instability, as they are associated with a low-pressure zone just behind the head of the spike and which retain the mushroom from propagating. Moreover, inside the coherent structures, the viscous forces and Kelvin-Helmholz instability lead the evolution of the flow-field and the development of the vortexes. In the code described in this document, the viscous forces are not taken into account, therefore it is not possible to correctly capture these features, even with higher-order of accuracy schemes. Due to the impossibility of carrying out experimental measurements which concern variables other than the growth of the interface, it is not possible to find a confirmation directly from the practical tests. Nevertheless, a support to the above statement comes by comparing the results presented in the previous paragraph against the prediction obtained with a different numerical simulation on the same test case. Mueschke et al. (2005a) used a second-order accurate inviscid solver on a 100×310 grid to compute the SM-RMI in its incompressible version. The comparison of the growth of the instability

presented in the paper against the combination RU+M5 is presented in Figure 4.7. As it is possible to notice from the graph, perfect agreement is found between the different inviscid numerical techniques.

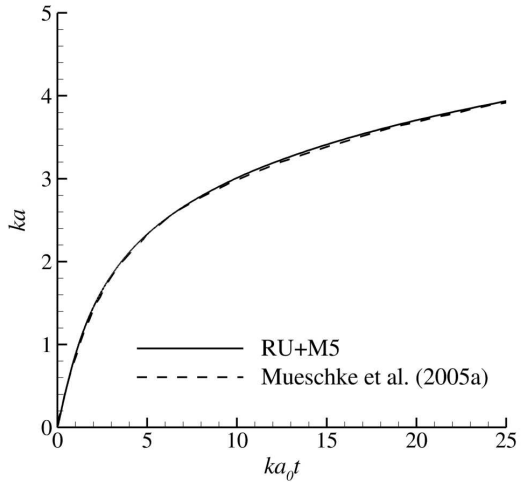

FIGURE 4.7: Growth of the instability computed by RU+M5 compared against the inviscid simulation from Mueschke et al. (2005a).

4.3 Acceleration pulse

This second modelling approach was also taken into consideration to test the solver and the data for the initialisation were provided by Kotelnikov et al. (2000). Here, the authors used the Vortex-In-Cell (VIC) technique to numerically replicate the experimental test case from Jacobs and Niederhaus (1997), who adopted the falling tank technique to trigger the incompressible RMI. The measured acceleration history is showed in Figure 4.8.

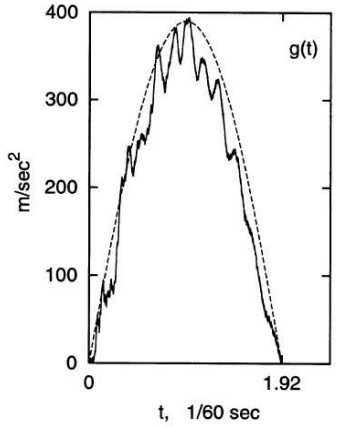

FIGURE 4.8: Acceleration pulse on the falling tank (Kotelnikov et al., 2000). The solid line represents the measurement by the accelerometer and the dashed line is the approximating analytical function Equation (4.9).

The solid line which represents the recorded data is approximated by the analytical

function:

$$g(t) = \begin{cases} 390 \sin(\pi/1.92t) \text{ m/s}^2 & \text{if} \quad 0 < t/60 < 1.92 \\ 0 & \text{otherwise} \end{cases}, \tag{4.9}$$

The temporal unit of measurement considered is 1/60 s since this corresponds to the time between two subsequent experimental frames.

4.3.1 Description of the test case

Using the gravity force to trigger the instability in the numerical model requires that the interface between the fluids is not flat as in the previous case. In fact, if in the case of the impulse of velocity the deposition of baroclinic vorticity was directly included in Equation (4.1), the use of the experimental data to trigger the instability requires the interface to be shaped accordingly to the desired case. Here, the SM-RMI is still considered. The perturbation is sinusoidal with a constant wavelength $\lambda = 74.87$ mm. As in the previous case, only one wavelength is taken into consideration in the simulation and symmetric BC is applied along the direction normal to the impulse. The amplitude of the wave a is 2.32 mm. The fluid densities are set to 1.96 Kg/m^3 and 2.52 Kg/m^3, which result in $A_t = 0.125$.
The dimensions of the domain are: $-74.87 \leq x \leq 74.87$ mm and $0 \leq y \leq 74.87$ mm and the grid resolutions employed are: 64×32 (G1), 128×64 (G2) and 256×128 (G3) cells.
The Riemann-solver for this investigation is RU. The choice is made according to the results obtained for the impulsive initialisation. In fact, even though the results produced by the schemes are in very good agreement for the integral quantities of interest, RU proved to be the least affected method by the high-resolution scheme chosen. Due to the explorative nature of the test case, M2 is employed in conjunction with RU because of its light computational demand compared to the other high-resolution methods.

4.3.2 Comparison against experiments and VIC simulations

The growth rate of the instability computed by the PP solver and compared with the reference results from Kotelnikov et al. (2000), which found very good agreement with the experiments, is presented in Figure 4.9.
The convergence of the grid is obtained for G3. A clear overestimation of a is noticeable at late-time, whereas perfect agreement between the simulations is found at the early stage of the instability. In order to investigate further into this discrepancy, comparison of the flow-field at different instants in time is provided in Figure 4.10, where the evolution of the mushroom computed by the PP solver and the experimental images are juxtaposed.
From the images, it appears clear how the formation and the evolution of the side vortices predicted by the numerical simulation is delayed with respect to the experiments. Comparing the flow field when the coherent structures are forming (Figure 4.10d), it clearly stands out that the vortexes at this moment in time are in a more advanced status of development in the experiments. In fact, the PLIF image shows that the coherent structures present half of a roll-up, whereas in the simulation this feature has

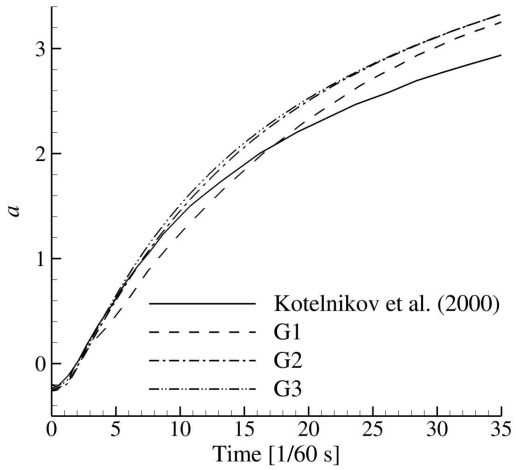

FIGURE 4.9: Growth of the instability computed by the PP solver compared against the VIC simulation from Kotelnikov et al. (2000).

just started to form. This delay has repercussions on the successive evolution of the mushroom and the number of roll-ups in the simulation at late-time ($t/60 = 35$) does not equal the experiments.
The overestimation of the growth in the PP case finds an explanation when the value of the circulation, Γ, in time is plotted against the VIC result. Figure 4.11 shows the comparison of evolution of the Γ, defined as:

$$\Gamma = \int_{y \leq L_y/2} \omega \, dxdy \, , \tag{4.10}$$

where ω is the vorticity.
In both cases, it is possible to notice how the baroclinic vorticity is generated by the gravitational pulse during $0 < t/60 < 1.92$ and successively ($t/60 > 1.92$) Γ manifests a plateau. For $t/60 > 1.92$ no source of ω is present in the numerical field, which is allowed to evolve freely. Nevertheless, the amount of vorticity deposited at the interface by the gravity pulse is different depending on the numerics employed. The PP case predicts a higher Γ than the VIC case, which explains why the instability grows more quickly according to the former solver.

4.4 Summary

From the comparison of the PP results against the VIC numerical simulations and experiments, it appears clear how the PP solver presented in this thesis is sensitive to the triggering cause of the instability. In fact, using the impulse of velocity allows to obtain very good agreement with the experiments. On the contrary, if the instability is caused by a pulse of gravity, then the simulations fit very well with the experimental data only during the early-stages and at late-times they tend to overestimate the growth. A common point which was found is that, in both cases, the coherent structures typical of the SM-RMI computed by the PP code are not as detailed as what the experiments found. In fact the number of roll-ups predicted by the numerical simulations is less

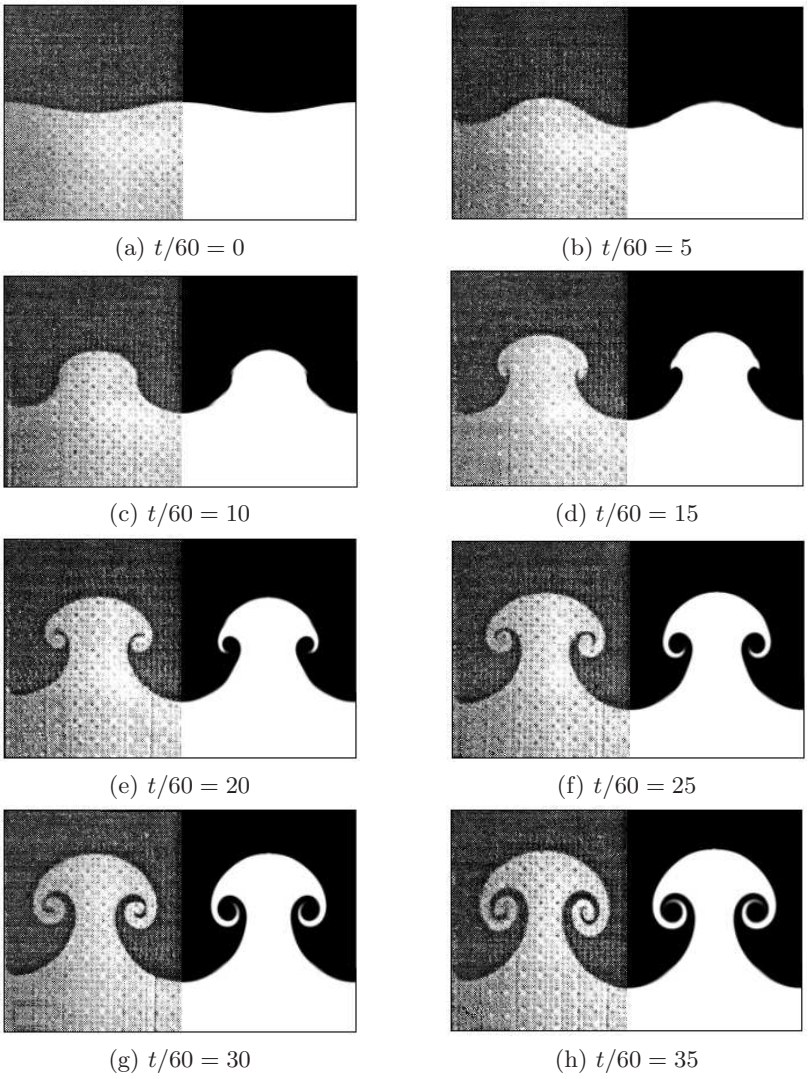

(a) $t/60 = 0$ (b) $t/60 = 5$

(c) $t/60 = 10$ (d) $t/60 = 15$

(e) $t/60 = 20$ (f) $t/60 = 25$

(g) $t/60 = 30$ (h) $t/60 = 35$

FIGURE 4.10: Juxtaposition of the image of the the RMI mushroom at different instants in time from the experiments (Jacobs and Niederhaus, 1997) (left) and from the simulation (right). The snapshot from the numerical simulations are rotated for better comparison.

than what appears in reality. Comparison with other inviscid simulations allowed to clarify that the inviscid nature of the Euler equations is the reason of the discrepancy. It is of no interest to investigate further into this field as the issue has already been a topic of research in the literature (Mueschke et al., 2005a,b). Secondly, even though the SM-RMI is currently a field of research, this project aims to create a new numerical approach to investigate the MM-RMI.

The discrepancies against experiments that were noticed in the incompressible simulations also highlight how the assumption of perfect fluids might not be appropriate for SM studies as the cores of the late-time coherent structures, where the viscosity plays a dominant role, is not properly represented. For reliable long-time SM simulations, it is crucial to correctly capture these vortices as the viscous forces acting within strongly influence the growth of the instability at late-time. On the other hand, when the per-

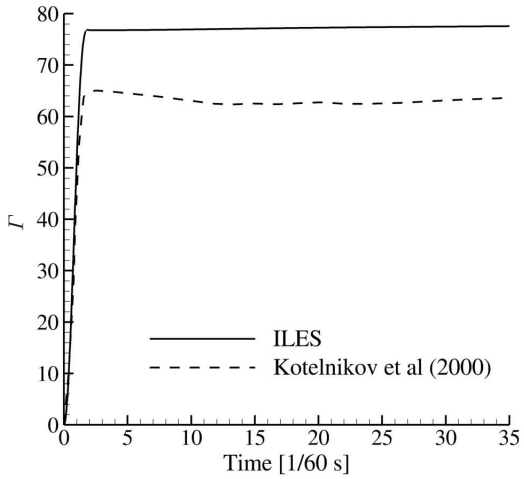

FIGURE 4.11: Circulation for $0 \leq y \leq L_y/2$ computed by the PP solver and VIC method.

turbation includes a range of different wavelengths, the evolution of the mixing layer is independent from the viscosity of the fluids. In MM-RMI each protuberance of the interface generates a single mushroom and late-time behaviour is governed by the interactions between these structures which generate new scales of motions that interact with the whole flow field. Therefore, the range of temporal and spacial scales is broad and the viscosity does not have an important effect on the growth of the mixing layer. Further confirmationd comes from the numerical simulations and theories presented in §2.3, as all of them make use of the Euler equations.

On the base of all the two-dimensional analysis, it has also been possible to realise how the reconstruction variants have a smaller influence on RU than on LF and HLL. Therefore the former Riemann-solver was chosen to be used in the three-dimensional simulations presented in the following chapter. The decision of not using the HLL scheme, although the good results, is due to the fact that its two-wave structure is not appropriate for the incompressible model, which exhibits a one-wave structure solution. Moreover obtaining convergence of the pressure residual proved to be difficult, especially when high-order methods were employed. W9 was also not included in MM-RMI either since the ratio between computational cost and result improvements turned out to be very high.

5
Hybrid treatment of RMI

Synopsis

The late-stage of RMI where the shocks are sufficiently far from the interface is characterised by a low velocity flow field. This prompts to the use of the incompressible model in the simulations, as compressible solvers are affected by issues when they are employed for low-Mach number flows. A novel technique which consists in operating a numerical switch, or transition, between compressible and incompressible method is used to study the late-stage of the instability. Using a shock wave to trigger RMI and investigating the compressibility of the numerical field in time showed that there are the conditions for initialising the PP solver from the results computed by the compressible model. Comparison between fully compressible and hybrid solution on both SM- and MM-RMI cases are presented. Moreover, the simulation time is pushed beyond any limit reached so far with a compressible code in order to study the very late-stage of the instability.

Much of the work in this chapter will be included in:
T. Oggian, D. Drikakis, D.L. Youngs and R.J.R. Williams. 'A hybrid compressible-incompressible solver for multi-component flows' and it will also be presented at the 13^{th} International Workshop on the Physics of Compressible Turbulent Mixing. 16-20 July 2012, Woburn (UK).

5.1 Compressible methods in the low-Mach limit

Assuming a general single-specie flow, from a theoretical point of view the incompressible model is only a subset of the compressible case and the difference between them lies on the fact that the density in the latter is considered to be constant both in space and time instead of a varying parameter. Nevertheless, two distinct sets of PDE of different nature, Equation (3.7) and Equation (3.11), are employed for the representation of the models, implying that different numerical techniques have to be considered in order to solve them. This brings about two relevant issues: is a compressible solver capable of correctly capturing the low-Mach structures which could be present in the numerical field? Is the solver able to run in a stable and consistent manner with the flow physics if, for any reason, the numerical field becomes incompressible during its evolution? Numerical simulations by Volpe (1993) showed that the FV method employed to solve the compressible model for low-Mach number flows fail. The first analytical analysis of the problem was presented by Turkel et al. (1994) and a clear understanding of the matter was achieved thanks to the works of Schnochet (1994) and Grenier (1997). Studying the Euler equations in their compressible formulation, the authors found that their solution, $s(\mathbf{x}, t)$, can be split into a fast acoustic component $s_{\text{fast}}(\mathbf{x}, t, t/M)$ and a slow component $s_{\text{slow}}(\mathbf{x}, t)$ in the following way:

$$s(\mathbf{x}, t) = s_{\text{fast}}(\mathbf{x}, t, t/M) + s_{\text{slow}}(\mathbf{x}, t) + \mathcal{O}(M^*) \, . \tag{5.1}$$

s_{slow} represents the solution of the incompressible system and it has the order of magnitude $\mathcal{O}(M^2)$. Carrying out the asymptotic analysis for the discrete Euler equations and comparing the results with the exact solution, initially Guillard and Viozat (1999) and successively Guillard and Murrone (2004) showed that in Godunov-type schemes the solution of the Riemann problem at the cell interface creates an artificial acoustic wave of the same order of magnitude of $\mathcal{O}(M)$ which destroys the incompressible sought solution. This is known in the literature as 'cancellation error' and it is strictly related to numerical round off errors. When $M \ll 1$, the thermodynamic quantities ρ, p and T change very slightly if compared with their stagnation quantities. This implies that the value of their gradients, which are included in the slow component of the solution (5.1), can be small enough not to be computed with the necessary accuracy. Further analytical analysis by Thornber et al. (2008a) related the entropy generation with the dissipation of kinetic energy, proved that the projection of the initial data on piecewise constants creates an artificially large velocity jump at the cell interface. In addition to the cancellation error, compressible codes also suffer from loss of efficiency during the simulation time. In fact, for this class of solvers, the stability condition is dictated by the speed with which the fastest acoustic wave travels, i.e. the highest eigenvalue of the system:

$$C = \frac{\lambda^n \Delta t}{\Delta x} \, , \tag{5.2}$$

where $\lambda^n = \max\{|u_q| + a_q\}$. The subscript $(.)_q$ indicates the three directions x, y and z. Hence, when the Mach number of the flow is low and the sound speed, a_q, becomes significantly larger than the speed with which the flow evolves, u_q, the speed of acoustic waves determines the time-step size even though they do not play a significant role in

the fluid flow. This implies a clear loss of time-marching efficiency.
Since the incompressible model is a subset of the compressible one, the latter can somehow be modified to improve the quality of the solution when M is low. Obviously, it does not work the other way around. In order to overcome these issues, three main paths have been followed so far. The first way is to entirely modify the numerics to solve the compressible Euler equations, either introducing a reference state for the variables and perform the calculations only on their fluctuations (Sesterhenn et al., 1999), or introducing a predictor-corrector type algorithm which involves the solution of one (Klein, 1995; Roller and Munz, 2000) or two elliptic-equations for the pressure (Schneider et al., 1999). The second method, adopted by Guillard and Murrone (2004) and by Thornber and Drikakis (2008), aims at modifying the Riemann-solver itself either by compensating for the strength of the acoustic wave, in the former, or modifying the wave strengths in the Roe scheme, in the latter. The third way, which focuses on the solution of the cancellation error, was introduced by Thornber et al. (2008b). It consists in correcting the extrapolated quantities locally in order to reduce the artificial velocity jump at the cell interfaces.
In the framework of RMI, it is of key importance to have a reliable compressible solver at disposal even when M is low since the instability involves both flow regimes: compressible at early time and incompressible during the late-stage (see §1.2). In this chapter, a new way which aims to overcome the issues mentioned above is presented and tested. Although the method was initially thought and developed to study the late-time growth of RMI, it does suit all those classes of flows which start as compressible and become incompressible with time. The approach does not follow any of the previous paths which have been investigated so far since it does not try to modify the compressible methods used in order to compute low-Mach number flows. From a conceptual point of view, it is much simpler, even though much more drastic than the solutions previously presented and it allows to bypass the issues related to the cancellation error and the time-stepping computation typical of compressible solvers. The main idea behind it is to employ the right numerical model depending on the situation of the field. The simulation starts with a compressible solver to allow the shock wave to trigger the instability and at a precise moment during the simulation a literal switch to the incompressible solver previously introduced is operated. The compressible solution is employed as the new initial condition.

5.1.1 Numerical transition

The numerical transition between the compressible and incompressible solver is based on the Mach number of the flow. After every time-step of the compressible phase, the distribution of M in the computational domain Ω is calculated and the switch is operated when $\max_\Omega\{M_{i,j,k}\}$ is less than a given threshold M_{NT}, which is a matter of investigation.
Moving from compressible to incompressible model implies a change in the unknown:

$$[\rho, \rho u, \rho v, \rho w, E, \rho V_f]^{\mathrm{T}} \longrightarrow [p, \rho u, \rho v, \rho w, \rho]^{\mathrm{T}} \, .$$

As it is possible to notice, both the pressure and the density fields need to be initialised. There are two ways for initialising the pressure. The first is from the equation of the

total energy E per unit volume:

$$E = \frac{p}{\gamma - 1} + \frac{1}{2}\rho_{\mathrm{C}}|\mathbf{U}|^2 \,, \tag{5.3}$$

which in this case becomes:

$$p = (\gamma - 1)\left[E - \frac{1}{2}\rho_{\mathrm{C}}|\mathbf{U}|^2\right] \,. \tag{5.4}$$

The second way is as a constant value throughout the domain. Since the initial distribution of p is only the initial guess needed by the iterative solver, the best choice is dictated only by the numerics, i.e. by the ease with which the iterative process reaches the converged solution. The achievement of the incompressible solution is guaranteed by solving the pressure equation which computes the pressure distribution needed for a divergence-free field.
The key point is how to initialise the incompressible density inside the numerical field. In fact, the densities of the fluids need to be artificially corrected in order to respect the incompressibility constraints which assumes them to be constant for a given fluid. The distribution of ρ inside the numerical domain is consequently adjusted by using the volume fraction from the compressible simulation. The solution adopted here is the following. First, considering the compressible solution, the cells where V_f is either 1 or 0 are identified and their densities are averaged separately, thus obtaining a value for $(\rho_1)_{\mathrm{I}}$ and another for $(\rho_2)_{\mathrm{I}}$. The other step is to assign the value of density to the cells where mixture between the fluids is present, i.e. $0 < V_f < 1$. This is accomplished through the use of the volume fraction available from the compressible solution:

$$\rho_{\mathrm{I}} = V_f(\rho_1)_{\mathrm{I}} + (1 - V_f)(\rho_2)_{\mathrm{I}} \,. \tag{5.5}$$

Even though the distribution of the density is artificially modified in order to enforce the conditions for incompressibility, the conservative variables ρu, ρv and ρw remain unaltered.

5.2 RMI transition investigation

The Richtmyer-Meshkov instability is triggered by a shock wave hitting the perturbed interface between two fluids of different densities. This generates a transmitted shock wave which travels along the same direction of the incident shock and a reflected wave, which travels backwards. As the reflected and transmitted shock waves move away from the interface, the effect of compressibility on the mixing layer becomes less and less important and the incompressible regime is achieved in time. It is commonly accepted that the transition from compressible to incompressible evolution of the mixing layer takes place when Richtmyer's linear model starts to break down. Very few studies on this matter have been presented in the literature. The very first one was conducted by Aleshin et al. (1988), who carried out some experiments on the single-mode RMI, trying to quantify the transition time. The authors proposed the following relation:

$$\Delta t_{\mathrm{tr}} \approx \frac{1}{k^2 A_t \Delta u a_0} \,, \tag{5.6}$$

where, Δt_{tr} is the time-interval between the instant when the shock hits the interface and the transition between compressible and incompressible evolution of the mixing zone. A similar relation was proposed also by Grove et al. (1993). Equation (5.6) represents a possibility on which basing the numerical transition that is intended to be tested in this work. In order to check the feasibility of the hybrid compressible-incompressible simulation and the moment of switch between the models, it is necessary to investigate further into the result of Aleshin et al. (1988) and into the transition between the flow regimes. For this purpose, both of the two-dimensional single-mode and the three-dimensional multi-mode test cases are considered.

5.2.1 Single-mode perturbation

The dimensions of the domain for the SM test case are $-4\pi < x < 4\pi$ and $0 < y < 2\pi$ with a grid resolution of 256×64 cells. The initial conditions of the fluids, derived from Li and Zhang (1997), consist of a light and a heavy gas separated by a sinusoidal perturbation of amplitude 0.2 and an incident shock wave with Mach number 1.5 travelling from the light towards the heavy fluid along the x-direction. Supposing the starting position of the shock to be at $x = -1.0$, the initial state of the fluids are the following:

$$-4\pi < x < -1.0 \quad (\rho, u, p) = (1.98, -6.15, 256250) \ , \tag{5.7}$$

$$-1.0 < x < 1.0 + \wp(y) \quad (\rho, u, p) = (1.15, -151.1, 100000) \ , \tag{5.8}$$

$$1.0 + \wp(y) < x < 4\pi \quad (\rho, u, p) = (5.77, -151.1, 100000) \ , \tag{5.9}$$

where $\wp(y)$ is the perturbation applied to the interface. Due to the Eulerian nature of the code, the non-shocked fluids are assigned a non-zero x-velocity component in order to keep the interface at the centre of the domain after the incident-shock hits it and to avoid it to be pushed out. The boundary conditions are periodic along the y-direction, whereas a one-dimensional extended domain is used at both the inlet and the outlet in order to allow the shocks to exit the domain preventing their excessive reflection. This technique does not completely eliminate the reflection of the shock waves, which is impossible to cancel where the mesh size changes, but reduces their magnitude by approximately 99.97% (Melnikov, 1995). The Riemann-solver employed is the compressible HLLC and the reconstruction of the variables at the cell interfaces is carried out by M2. The time-marching method adopted is the standard three-step RK and the CFL number was set to 0.2.

Using the initial data and Aleshin's formula, it is possible to estimate the instant when the linear model starts to lose its validity for this test case. The time between the start of the simulation and when the incident shock hits the interface is estimated as $\Delta t_{\mathrm{hit}} = \Delta x / M_0 c_0 = 0.00089$ s, where M_0 and c_0 are respectively the Mach number and the speed of sound of the non-shocked heavy fluid. On the other hand, using Equation (5.5) it is possible to find: $t_{\mathrm{tr}} = 0.06513$ s. Therefore, the linear model is expected to break down after about 0.06602 s from the start of the simulation. Excellent agreement of this numerical estimation is found with the numerical simulation. Looking at the growth of the interface plotted in Figure 5.1, it is possible to observe that it is deviating from the linear model exactly around the moment in time predicted by

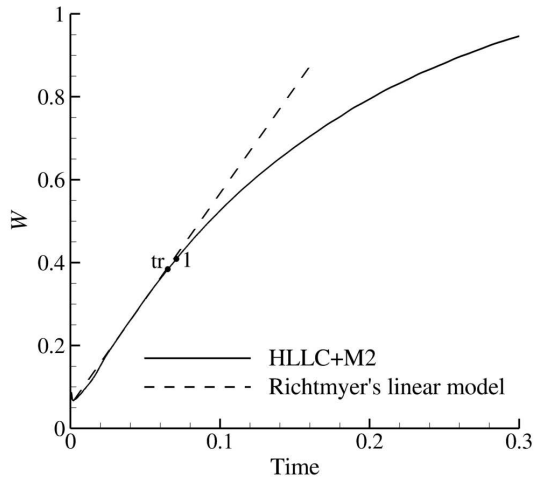

FIGURE 5.1: Comparison between Richtmyer's linear model and the growth predicted by the numerical simulation. The point '1' represents the instant computed using Aleshin's formula Equation (5.6) and the point '2' represents the instants when the transmitted shock wave has left the domain.

Aleshin's formula, which is represented on the graph by the black point on the line marked as 'tr'. Although the results match very well, it is still not possible to take Equation (5.6) as the reference for applying the numerical transition. In fact, looking at Figure 5.2c and Figure 5.2d, it appears clear how at t_{tr} the transmitted shock wave is still present inside the numerical domain and it is travelling towards the left side. Therefore, the effects of compressibility are still dominant and this does not allow to initialise the incompressible solver. In order to operate the numerical switch on the base of Equation (5.6), a shorter domain would be needed, but in this case a priori knowledge of the final dimension of the mushroom is needed to choose an appropriate length. Another possibility is not to change the original dimensions of the domain and to wait for both shock waves to be gone. In fact, the points 'tr' and '1' in the graph of Figure 5.2c are very close and at t_1 the linear model has just started to break down. Therefore, a slight delay with respect to the optimal point can be introduced in the transition instant without being too far from it. It also needs to be remarked that Equation (5.6) is only meant for single-mode perturbations and it is not possible to do such a prediction for multi-mode interfaces. The numerical switch can therefore be based on either the value of divergence of velocity or the Mach number inside the domain. Since there is not a clear threshold between a compressible and incompressible flow for the former parameter, $M < 0.3$ is adopted as the rule for distinguishing the two regimes. When the transmitted shock leaves the domain ($t \approx 0.07097$), it is possible to see from Figure 5.2f how the Mach number inside the domain is close to zero all over the domain but around the developing interface it assumes values around 0.16. This indicates a clear incompressible flow with which the PP solver can be initialised.

5.2.2 Multi-mode perturbation

The three-dimensional domain for the investigation on the transition for multi-mode perturbation are $-2\pi < x < 2\pi$, $0 < y < 2\pi$ and $0 < z < 2\pi$ and the computational mesh has a resolution of $64 \times 32 \times 32$ cells. The perturbation at the interface is given

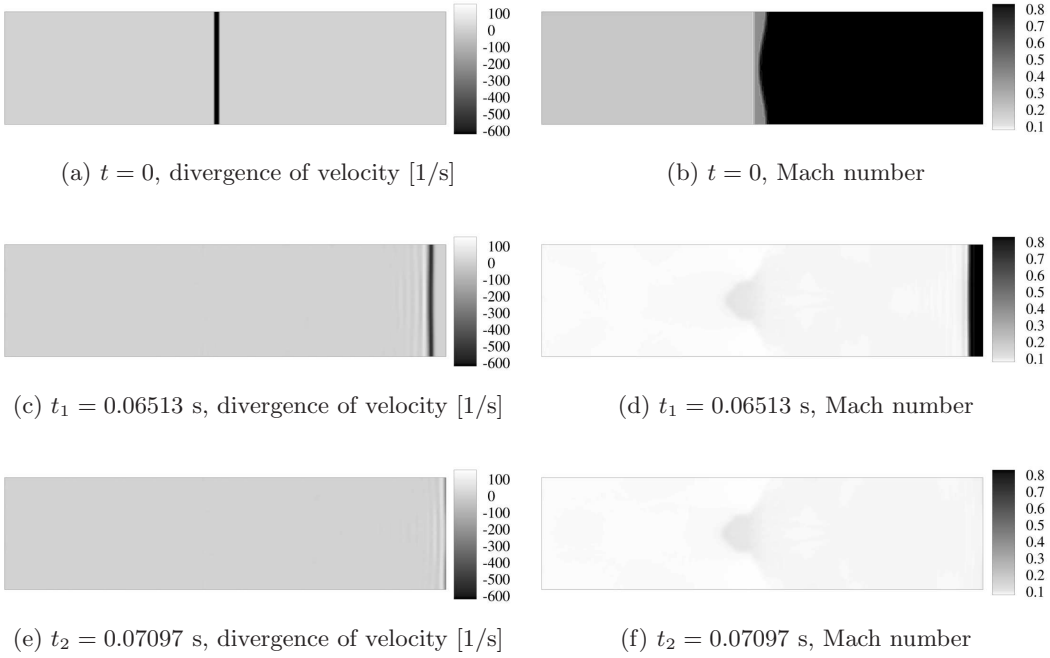

(a) $t = 0$, divergence of velocity [1/s]

(b) $t = 0$, Mach number

(c) $t_1 = 0.06513$ s, divergence of velocity [1/s]

(d) $t_1 = 0.06513$ s, Mach number

(e) $t_2 = 0.07097$ s, divergence of velocity [1/s]

(f) $t_2 = 0.07097$ s, Mach number

FIGURE 5.2: Contour floods of divergence of velocity (left) and Mach number (right) at significant instants in time.

by a Narrow Band (NB) combination of linear modes with random phase and a power spectrum proportional to the inverse of the wavenumber[1]. The initial conditions and the numerics employed for this case are the same as in the SM case.
In Figure 5.3 it is possible to observe the growth of the instability computed in time and the point '1' is the instant when the transmitted shock has left the domain ($t \approx 0.0240$ s). Similarly to the previous case, the shock exits the domain when the linear stage of the instability is ending. Looking at the compressibility of the numerical field at this instant in time (Figure 5.4), the Mach number inside the domain is well under 0.1 almost everywhere, with an exception made for the zone around the growing interface and the right side of the grid. In fact, since the transmitted shock has just left the domain, part of its wake is still present. Nevertheless, confirming the results obtained for the two-dimensional case, the flow field is clearly incompressible everywhere, which makes it possible to initialise the PP solver.

5.2.3 Criterion for the numerical transition

From the two test cases implemented, important conclusions can be drawn in view of hybrid simulations. If the formula Equation (5.6) was to be adopted, it might not be possible to operate the switch because both or either one of the transmitted and the reflected waves could still be present in the numerical domain. This would impede the initialisation of the incompressible flow model, since the compressibility of the numerical field is still too high. Moreover, the prediction is valid only when the perturbation is

[1] More details on the initial perturbation are given in §5.4.1.

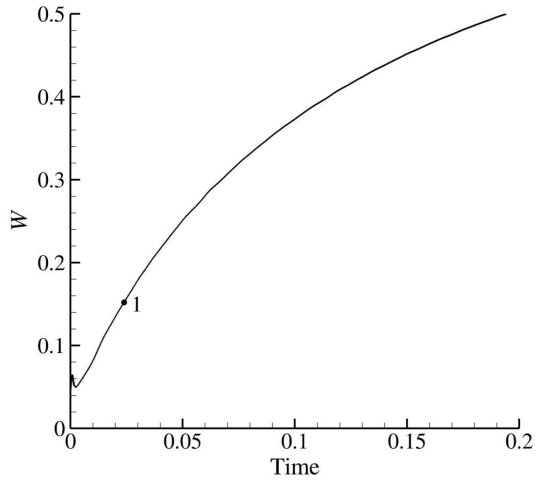

FIGURE 5.3: Growth of the multi-mode perturbation. The point '1' indicates the instant when the transmitted shock has left the domain.

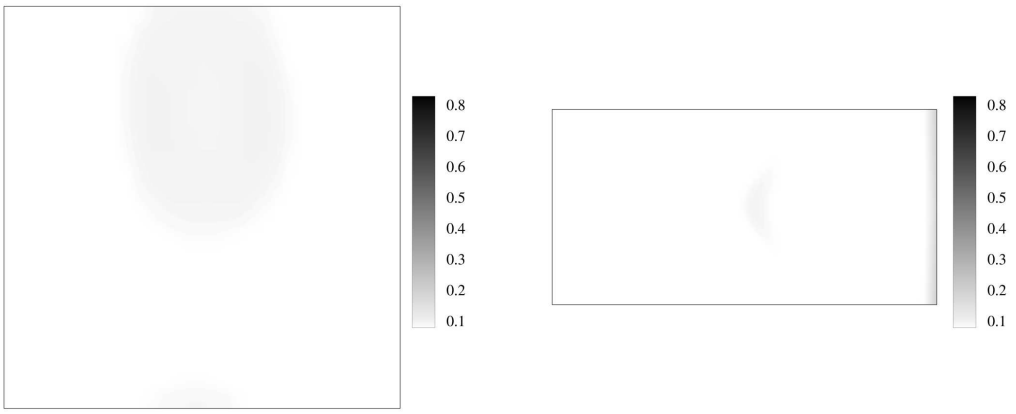

(a) y-z plane, $x \approx 0.25$. (b) x-z plane, $y \approx 1.57$.

FIGURE 5.4: Slices of the computational domain flooded with Mach number at $t_1 = 0.0240$ s for MM perturbation.

of SM type. Waiting until both shocks have left the domain constitutes another valid option for the numerical transition. In fact, as shown by the test cases, for the domain dimensions which are typically applied for studying RMI, the time needed for the shocks to move out from the domain corresponds approximately to the linear-stage of the growth of the instability. Therefore it is possible to take advantage of this fact and operate the switch just after the instants when the last shock has left the domain. The criterion used for the hybrid simulations is the following. After every time-step of the compressible phase, the distribution of M in the computational domain Ω is calculated and the switch is operated when

$$\max_{\Omega}(M_{i,j,k}) < M_{\mathrm{NT}} \ , \tag{5.10}$$

where M_{NT} is a given threshold which is a matter of investigation.

5.3 Hybrid single-mode perturbation

The first test case taken into consideration to test the hybrid solver is that of SM perturbation. The dimensions of the computational domain are: $-4\pi < x < 4\pi$, $0 < y < 2\pi$. Different grids with increasing resolution are employed to test the consistency of the method: G1 (64×16), G2 (128×32), G3 (256×64), G4 (512×128). The initial conditions are the same of the test case presented in §5.2.1.
The reconstruction at the interface is done by the M2 scheme, whereas the time-integration chosen is the third order Runge-Kutta method. The CFL number for the compressible simulations is 0.5 it is decreased to 0.05 during the incompressible stage. This change was due to stability reasons after the numerical transition. In fact, since the computation of Δt is different in the two cases, it was necessary to reduce the CFL number in order to preserve the value of the time-step after the transition, thus avoiding an abrupt change. The residual for the pressure equation during the incompressible phase of the simulations was chosen $r = 1 \times 10^{-4}$ in accordance with the pressure-convergence test. The value of M_{NT} on which the numerical transition is based is investigated and the values $M_{\mathrm{NT}} = 0.2$, $M_{\mathrm{NT}} = 0.3$ are taken into consideration. Similarly to the impulsive RMI, the parameter which is taken into account in the comparison of the results is the growth of the mixing layer defined as:

$$W_s = \frac{h_b + h_s}{2} , \tag{5.11}$$

5.3.1 Grid convergence and moment of transition

The grid-convergence test is based on the Grid Convergence Index (GCI), defined as (Roache, 1998):

$$\mathrm{GCI} = F_s \frac{|\epsilon|}{r^p - 1} . \tag{5.12}$$

ε is the relative error between two grids where one is created by doubling the resolution of the other and the values of the constants adopted are: $F_s = 3$, $p = 2$ and $r = 2$.

Time [s]	GCI [%]		
	G1-G2	G2-G3	G3-G4
0.10	4.55	1.16	0.42
0.15	3.69	0.46	0.34
0.20	2.83	1.02	0.38

TABLE 5.1: GCI at different instants in time (see Figure 5.5) after the numerical transition.

Figure 5.5 shows that the convergence of the grid is achieved by G3, but good results are also obtained using G2. Comments on the physical evolution of the instability are discussed in the next paragraph.
The next parameter which was checked is the influence of the moment at which the numerical transition was operated. Using $M_{\mathrm{NT}} = 0.2$ or M_{NT}=0.3 as reference for the transition did not bring any significant variation worth mentioning. This can be easily explained by looking at Figure 5.6.

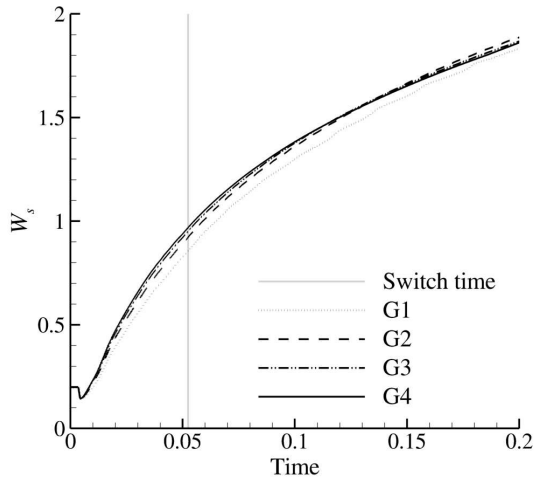

FIGURE 5.5: Grid-convergence for the growth of the mixing layer.

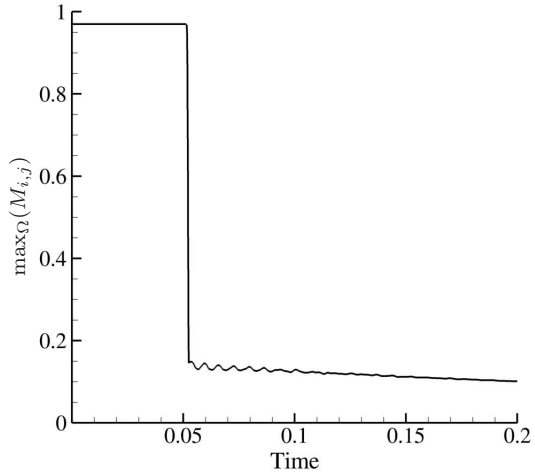

FIGURE 5.6: Highest local value of Mach number in time for fully compressible simulation.

The initial velocity component which the non-shocked fluids are given is meant to prevent the interface from being pushed out from the numerical domain while growing. This implies that the fluid far from the interface has very low velocity, therefore very low Mach number. Hence, the high value of $\max_\Omega(M_{i,j})$ at the early stage is due to the presence of the transmitted shock in the numerical field. As soon as this leaves the domain, $\max_\Omega(M_{i,j})$ drastically drops down from 0.96 to approximately 0.15 and the transition from $\max_\Omega(M_{i,j}) = 0.3$ to $\max_\Omega(M_{i,j}) = 0.2$ takes place in few time-steps without producing any remarkable difference between the after-switch physics of the numerical field in the two cases. The only alteration which was possible to notice was on the iterative process during the first time-steps immediately after the transition. In fact, setting $M_{\mathrm{NT}} = 0.2$ resulted in a higher number of iterations necessary for the Poisson-solver to reach the convergence (Figure 5.7).

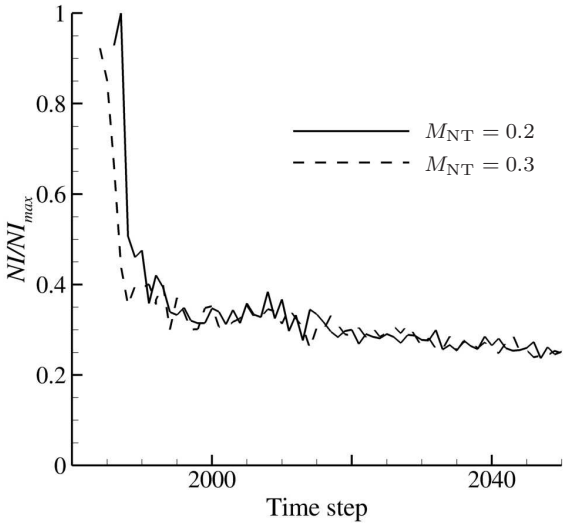

FIGURE 5.7: Number of Iterations, NI, necessary for the Poisson-solver to reach the convergence ($r < 10^{-4}$) during the first Time-Steps, TS, after the transition normalised by $NI_{\max}$. The numerical switch is operated between $TS = 1985$ and $TS = 1986$ for $M_{\rm NT} = 0.2$ and between $TS = 1983$ and $TS = 1984$ for $M_{\rm NT} = 0.3$.

5.3.2 Comparison with compressible simulation

Fully compressible simulations of the single-mode test case were run to compare the results obtained against the hybrid solver (H). The low-Mach correction is also employed (C+LM) in order to assess the improvement of the solution from the standard compressible solution (C). The numerical analyses considered for this purpose are the ones run using the finest grid G4. The density values computed at the end of the compressible stage and with which the incompressible solver was initialised are: $(\rho_1)_{\rm I} = 2.68$ and $(\rho_2)_{\rm I} = 13.01$.

The main distinction between the results obtained is that a divergence-free flow field must be retrieved after the numerical transition by the pressure-projection method in the hybrid simulation. Figure 5.8 shows the comparison of the evolution of the average value of $|\nabla \cdot \mathbf{u}|$ within the numerical domain in time for both the compressible and hybrid case, starting from the instant when the numerical transition was applied: $t_{\rm NT} = t(M_{\rm NT}) \approx 0.0052$ s.

As it can be noticed, the two methods give the results which are expected. After the transition, $|\nabla \cdot \mathbf{u}|$ in the compressible case has a low value but still far from being considered divergence-free, whereas when the incompressible solver is used, the parameter assumes a value very close to zero. It needs to be specified that the perfect divergence-free condition cannot be strictly achieved as the pressure term is computed by an iterative process within an appropriate tolerance (see Appendix A). In the former case, the divergence of velocity decreases very quickly in time after the last shock wave has left the domain, reaching its lowest value of about 1.45 $\rm s^{-1}$ at late-time. Therefore, even though for $t > 0.052$ s no shock wave is present in the numerical domain, traces of compressibility are clearly present. On the contrary, the incompressible stage of the hybrid simulation predicts a flow field which is divergence-free, considering an appropriate tolerance, from the very first time-step after the numerical transition. In fact, the average $|\nabla \cdot \mathbf{u}|$ is of the order of magnitude of 10^{-2} $\rm s^{-1}$, but for $t \geq 0.08$ it decreases to

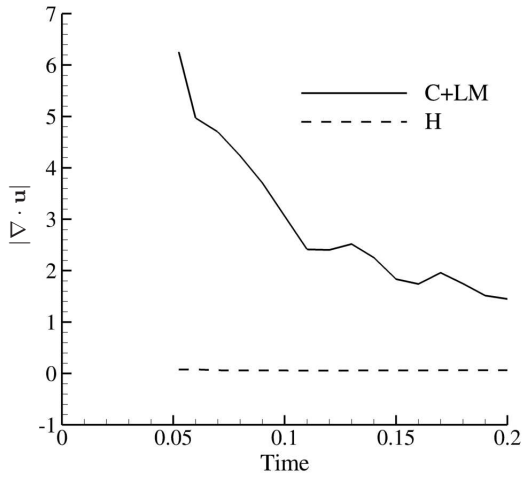

FIGURE 5.8: Average value of $|\nabla \cdot \mathbf{u}|$ in time after the numerical transition ($t_{\mathrm{NT}} \approx 0.0052$ s) for compressible (C+LM) and incompressible (H) case.

10^{-3} s^{-1}. A deeper insight on the distribution of divergence of velocity is obtained from Figure 5.9. Here, the punctual value along the central row of cells ($y = \pi$) is plotted for both C+LM and H cases at various moments in time for $t > t_{\mathrm{NT}}$. The compressible solution shows a very irregular trend which is bounded between +20 s^{-1} and -30 s^{-1} at $t = 0.06$ s and becomes smoother at late times, with -5 s^{-1} $> |\nabla \cdot \mathbf{u}| >$ +5 s^{-1}. In the hybrid simulations, the incompressibility constraint is also achieved locally, since the values of the parameter are of the order of magnitude of 10^{-3} at all the instants and along the entire dashed line.

The main parameter of interest for RMI cases is the growth of the mixing width. Its trend in time is plotted and compared in Figure 5.10. As it is possible to notice, at t_{NT} there is a bifurcation of the solution. In fact a very small discrepancy between the compressible and hybrid simulation is present and the latter predicts a slightly higher mixing between the fluids. This difference seems to slightly increase as the time goes by, since the two lines tend to move away from each other. Comparing the numerical values of a at some instants in time (Table 5.2), it is possible to notice that the relative error between the solutions, although very small, tends to increase for $t > 0.125$ s. The low values of ε_r show that even though the numerics involved with compressible and hybrid simulations are completely different, they tend to be in very good agreement. Another important outcome which needs to be pointed out is that the continuity of the trend is not broken during the first time-steps just after the transition. In fact the detail present in Figure 5.10 shows that a evolves naturally and smoothly in both cases without any non-physical discontinuity. This is confirmed analysing the value of the derivative da/dt at the time steps immediately after the transition for the two cases. In correspondence of the very first time-step after the transition $TS_{\mathrm{NT+1}}$, $(da/dt)_{\mathrm{C}} = (da/dt)_{\mathrm{C+LM}} = 11.7$, whereas at $(da/dt)_{\mathrm{H}} = 12.4$. As it is expected from Figure 5.10, this small difference confirms that in the incompressible case, the growth of the instability is slightly faster than in the two compressible cases. Concerning C and C+LM, the low-Mach correction does not seem to significantly improve the results for single-mode perturbation, since the lines which represent the solutions match almost perfectly.

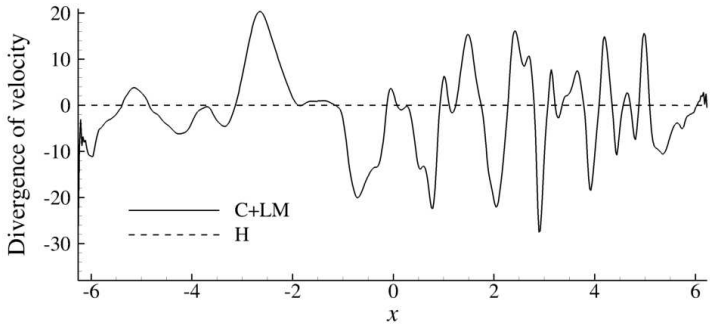

(a) $t \approx 0.060$ s

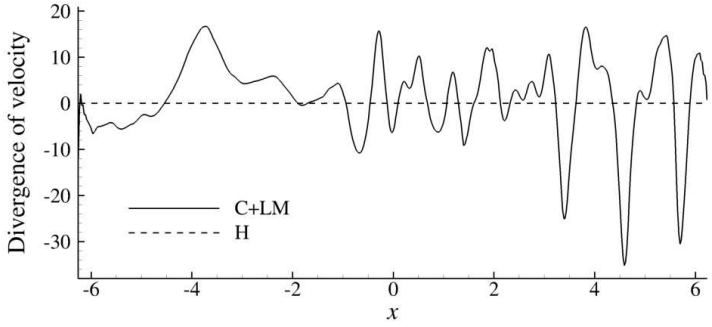

(b) $t \approx 0.080$ s

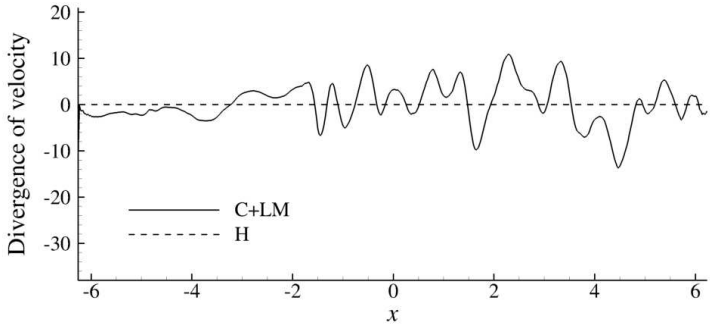

(c) $t \approx 0.12$ s

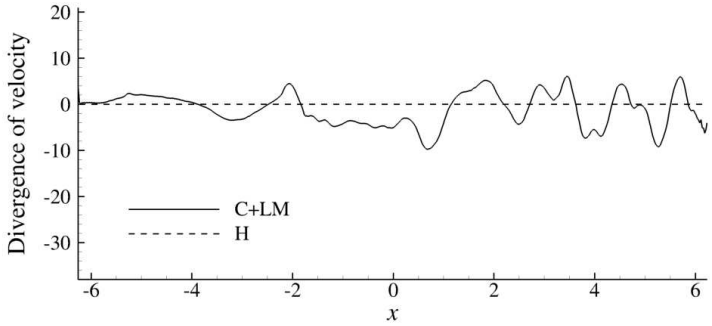

(d) $t \approx 0.16$ s

FIGURE 5.9: Absolute value of divergence of velocity along the central row of cells ($y = \pi$) for C+LM and H simulations at different moments in time. All the graphs refer to instants successive to the the numerical transition.

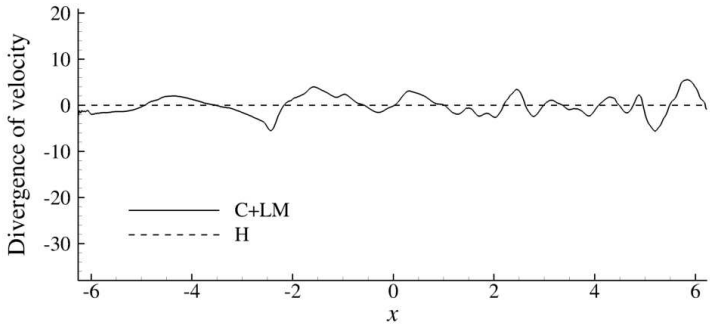

(e) $t \approx 0.20$ s

FIGURE 5.9: (*continued*).

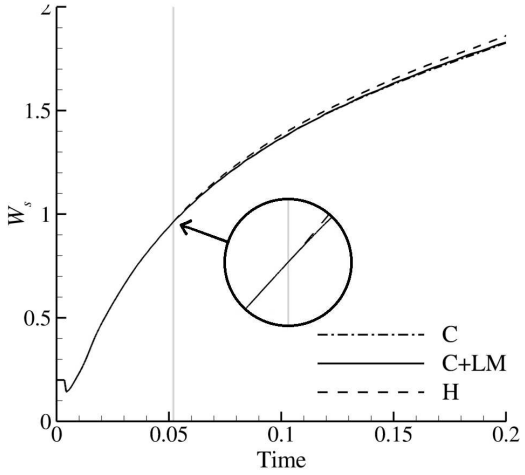

FIGURE 5.10: Predicted growth of the single-mode RMI by compressible, compressible plus LM correction and hybrid cases (G4). The grey line represents the instant of the switch.

Time [s]	$W_{s-\mathrm{C+LM}}$	$W_{s-\mathrm{H}}$	$\varepsilon_r[\%]$
0.075	1.18	1.20	1.03
0.100	1.37	1.38	1.27
0.125	1.51	1.53	1.14
0.150	1.63	1.65	1.22
0.175	1.74	1.76	1.39
0.200	1.83	1.86	1.74

TABLE 5.2: Relative error between compressible plus LM and hybrid solutions (see Figure 5.10).

Observing the contour flood of volume-fraction at various moments in time for $t \geq t_{\mathrm{NT}}$ the agreement of the results showed by the growth of the instability is confirmed also from a visual point of view. A first analysis of the two compressible cases shows that the use of the LM correction makes a quite noticeable difference from a qualitative point of view. Even though the outer shape of the mushroom and the number of roll-ups are the same, the C case presents a very diffused and fuzzy mushroom. The low-Mach

correction improves the results and the development of the instability looks sharper and less diffused, especially in the zones where the roll-ups evolve. A further improvement is achieved by the use of the incompressible solver in the H case. The compressible and incompressible mushroom look very similar to each other. However, the latter produces an even sharper mushroom than the C+LM case, with more and better defined roll-ups at its sides. C and C+LM cases present two symmetric vortexes which, at late-time ($t \approx 0.200$ s), are rolled-up twice. The H solver instead captured three roll-ups, which are more clearly distinguishable as well.

5.4 Hybrid multi-mode perturbation

The MM perturbation is of particular interest since it is a closer representation of reality than the SM case. In this section, two different sets of initial conditions are taken into consideration. The first is the Light-to-Heavy (L-H) impact, which has already been employed in all the simulations presented in the previous paragraph of this chapter, whereas the second set of initial conditions consists in a Heavy-to-Light (H-L) case.
The dimensions of the computational domain are: $0 < x < 2.8\pi$, $0 < y < 2\pi$ and $0 < z < 2\pi$ with grid resolutions of $180 \times 128 \times 128$ and $360 \times 256 \times 256$ cells respectively. The perturbation is the same NB used for the transition study in §5.2.2. Due to its grid-dependency, it is necessary to select a proper non-dimensional time in order to compare the results from the different grids employed. According to Richtmyer's impulsive model, the normalised time is chosen as:

$$\tau = t \frac{A_t^+ \Delta u}{\lambda_{\min}} \,, \tag{5.13}$$

where $\lambda_{\min} = 16\Delta x$ is the smallest wavelength included in the perturbation. During the compressible phase of the hybrid simulations the LM correction (Thornber et al., 2008b) was always employed and the same numerics and parameters were adopted for all cases, unless differently mentioned. The Riemann-solver was the CB and the time-marching scheme is the three-step RK-SSP, which was retained also for the incompressible phase. The CFL was 0.5 for the compressible stage and it was lowered to 0.2 after the numerical transition. The parameter of interest for the mixing between the fluids is the integral length of the mixing zone, which is defined as:

$$W = \int \overline{V_f} \left(1 - \overline{V_f}\right) \, dx \,, \tag{5.14}$$

where $\overline{V_f}$ is the volume fraction averaged over the y-z planes of the domain.

5.4.1 Initial interface perturbation

The initial perturbation at the interface has a constant power spectrum of the form:

$$P(k) \begin{cases} C & \text{if} \quad k_{\min} < k < k_{\max} \\ 0 & \text{otherwise} \end{cases} \,, \tag{5.15}$$

with $k_{\min} = 16\Delta x$ and $k_{\max} = 32\Delta x$, $k = \sqrt{k_y + k_z}$ wave vector and C constant. The interaction between shock and interface triggers the instability via mode coupling

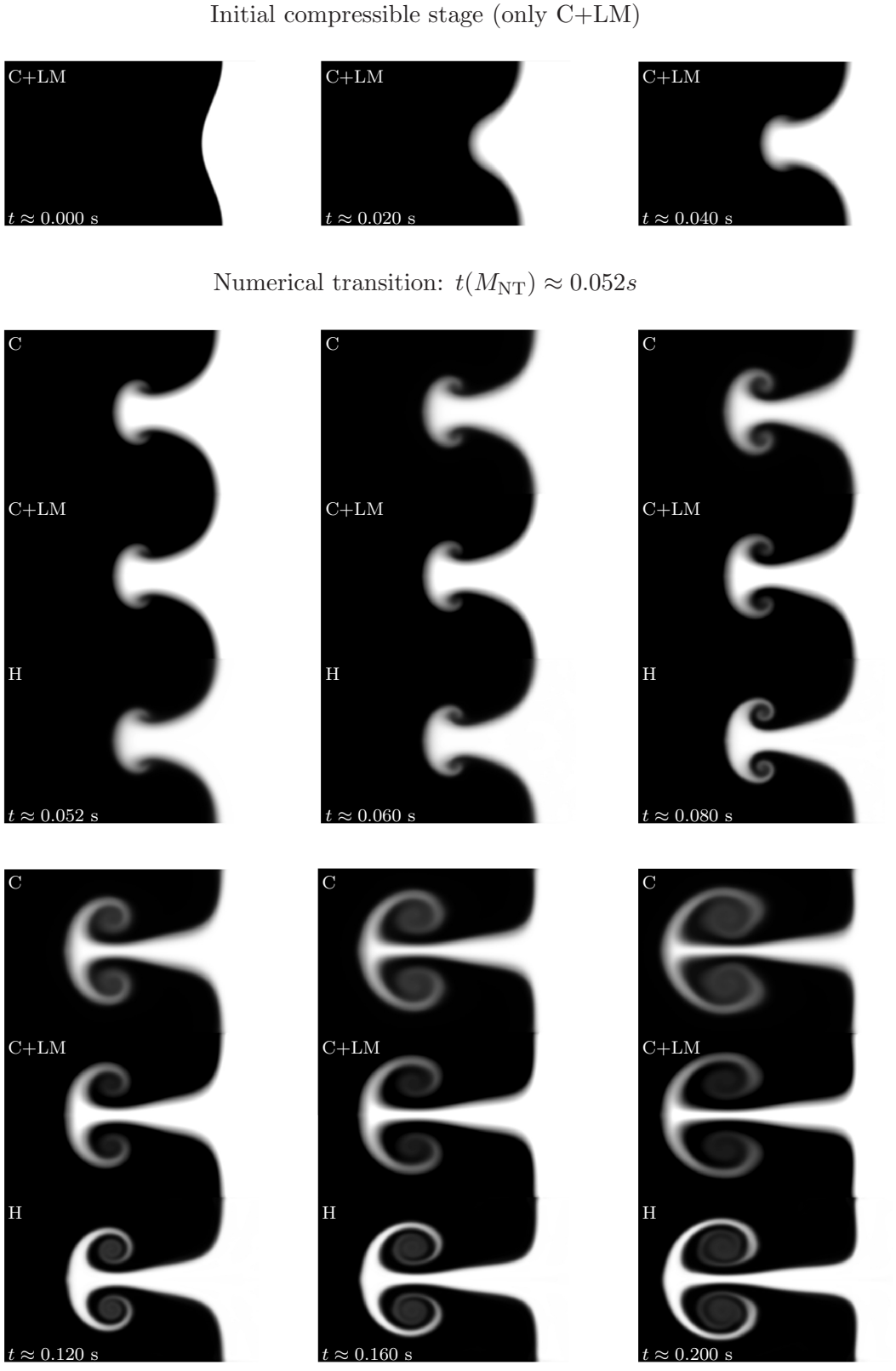

FIGURE 5.11: Volume-fraction snapshots. Comparison of the evolution between compressible and hybrid simulations (G4).

of the high wavenumbers, when the significant modes within the system have saturated (Thornber et al., 2010). Considering that a given power spectrum has equivalent amplitude:

$$a(\mathbf{k}) \propto \sqrt{\frac{P(k)}{k}} \,, \tag{5.16}$$

it is possible to use the inverse Fourier transform of this relation to calculate the perturbation in the physical space. Considering only the real part, one obtains:

$$\begin{aligned} a(y,z) = \sum_{m,n=0}^{N} & a_{m,n}\cos(k_0 m y)\cos(k_0 n z) + b_{m,n}\cos(k_0 m y)\sin(k_0 n z) \\ & + c_{m,n}\sin(k_0 m y)\cos(k_0 n z) + d_{n,m}\sin(k_0 m y)\sin(k_0 n z) \,. \end{aligned} \tag{5.17}$$

Here, m and n are the wavenumbers in the y and z direction respectively, whereas a, b, c and d are the amplitudes of the modes which are initialised from a random Gaussian distribution so that the standard deviation, σ, is proportional to the Fourier coefficients. In this work, σ has value $0.1\lambda_{\min}$.
It is important to ensure the linearity of the initial perturbation, i.e. the amplitude of the mode with wavenumber k is significantly less than its wavelength. This is achieved by appropriately choosing the coefficient C in Equation (5.15) in such a way that:

$$P(k) < \frac{k^3}{16} \,. \tag{5.18}$$

For more detailed information about the initialisation of the perturbed interface, a curious reader can refer directly to Appendix A of Thornber et al. (2010). Results from this publication are compared against the computations using the hybrid technique in §5.4.3. It is important to notice that even though CNS3D, the code employed by the authors in the aforementioned publication, and Hirecom share the same subroutine to compute the initial perturbation, some differences which do not allow a full comparison of the results and that also explain the observed differences are present. In particular, Hirecom does not scale the perturbation using the standard deviation, with the consequence that the interface appears flatter and with smaller protuberances than the one used in Thornber et al. (2010). This allows to consider the perturbation employed in this work as linear, but with a higher safety margin than CNS3D and moreover it explains the slower growth of the fully compressible mixing layer computed by Hirecom with respect to the predictions presented in the aforementioned paper. A further difference consists in how the codes apply the perturbation to the initial mass fraction field. In fact, Hirecom filters the perturbation by doing a 4-point average of the values output by the subroutine for each cell, whereas CNS3D employs an 'unfiltered' perturbation. This results in Hirecom presenting a smoother interface in addition to the previously mentioned smaller protuberances. Despite these differences, the fact that the linearity of the initial perturbation is preserved allows to consider the simulations presented in this work as physically valid.

5.4.2 Influence of the reconstruction scheme

Using different order of accuracy in the reconstruction process provides different amount of numerical diffusion. This inevitably affects the energy cascade process and it is therefore of particular interest to investigate the influence that it has on the spectrum of turbulent kinetic energy. In Figures 5.12-5.15, the TKE spectrum obtained from the numerical simulations on the finest grid together with snapshots of the mixing layer for different instants in time are presented. Each spectrum is the result of an averaging process of the spectra computed over ten slices of the domain along the x-direction, which is the direction of the shock propagation. These slices are selected to be at the centre of the mixing layer.

Comparing the evolution of the spectra in time, it is possible to notice that at early time ($\tau = 50$) the sub inertial range tends to decay in accordance to Kolmogorov's $k^{-5/3}$ for all the methods used and only later in time Zhou's $k^{-3/2}$ is achieved. This is explained by the fact that Zhou's theory assumes fully developed turbulence, therefore a period of transition between the instant when the shock hits the interface and when the achievement of fully turbulent regime by the mixing layer is needed. In fact, at $\tau = 150$ and $\tau = 200$, the decay of the subinertial range is closer to the modified $k^{-3/2}$, in accordance with analytical results. This transition was also noticed by Thornber et al. (2010) employing fully compressible simulations.

The use of different high-resolution methods results in a different decay of the TKE at high wavenumbers, independently from the moment in time. The schemes are in excellent agreement on the distribution of the energy among the energy-containing scales (low wavenumbers) and the peak is predicted around $k/k_{\min} = 0.25$. Increasing the wavenumber and entering the subinertial range allows to better observe the numerical diffusion provided by the reconstruction scheme. For all the methods employed, $k^{-3/2}$ is achieved, but the range of wavenumbers through which it extends is tighter as the order of accuracy of the method decreases. In fact, taking $k/k_{\min} \approx 1$ as the beginning of the subinertial range, for M2 it goes up to $k/k_{\min} \approx 2.5$, whereas for M5 or W5 it can be extended up to $k/k_{\min} \approx$ 3-4. Finally, in the dissipation range of the spectrum M2 gives a curve with higher slope than M5 or W5, which indicates that the smaller scales contain less energy and that consequently a higher amount of numerical dissipation is provided by this reconstruction scheme. This is particularly evident for $k/k_{\min} > 2$.

The excessive diffusion at high wavenumbers, which the lower order methods are affected by, results in an inability of the schemes to capture the small-scale structures present in the numerical field. This clearly stands out if the contour plots of the mixing layer showed in each of Figures 5.12-5.15 are compared. Independently from the instant in time, the higher order of accuracy methods M5 and W5 capture a more detailed flow field with a higher amount of scales which interact among each other. On the contrary, using M2 gives a flow field with much less details and dominated by bigger turbulent structures.

The growth of the instability does not present a significant influence from the reconstruction scheme. In fact, from Figure 5.16, all the predictions representing the high-resolution methods substantially lie on the same curve. From the literature presented in §2.3, theoretical analysis in accordance with experiments and simulations show that the growth of MM-RMI follows an exponential trend in time. In order to obtain a value for the exponent from the numerical results, the Non Linear Regression (NLR) package

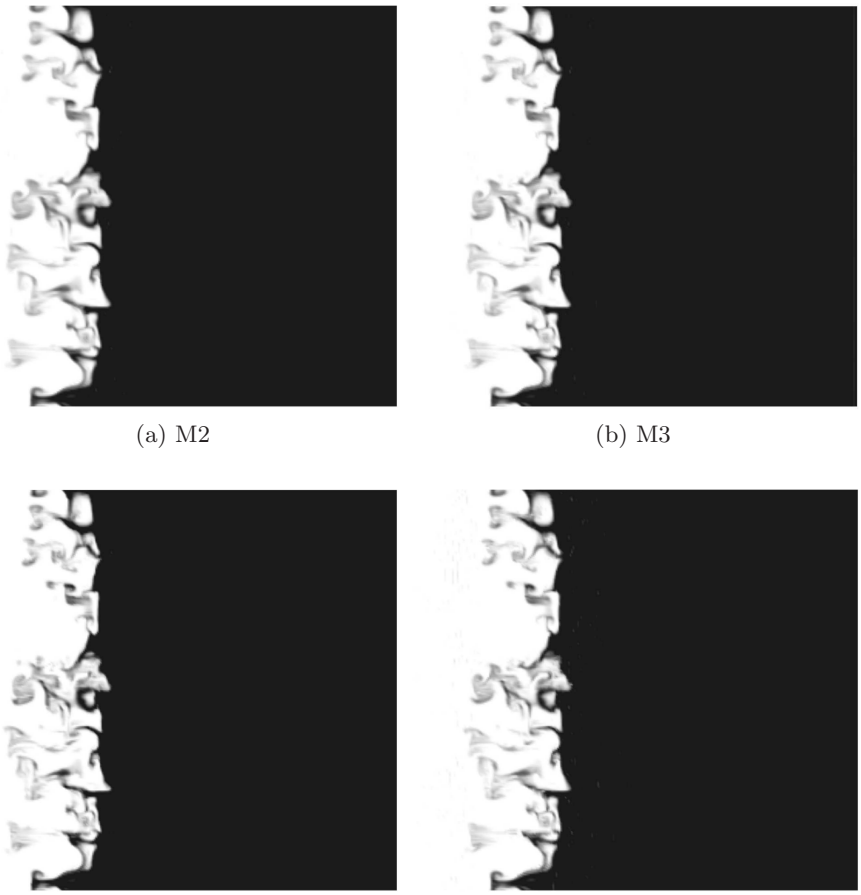

(a) M2 (b) M3

(c) M5 (d) W5

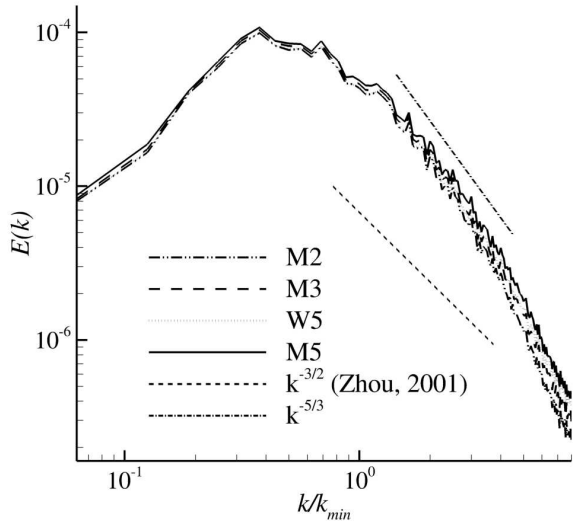

(e) TKE spectrum

FIGURE 5.12: Contour plots of the density (x-z plane, $y = \pi$) and spectrum of turbulent kinetic energy from the incompressible solver after the numerical transition is operated at $\tau = 50$.

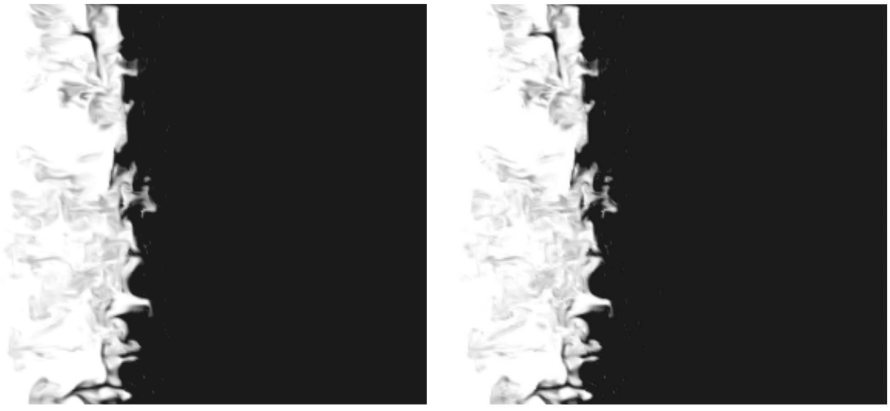

(a) M2 (b) M3

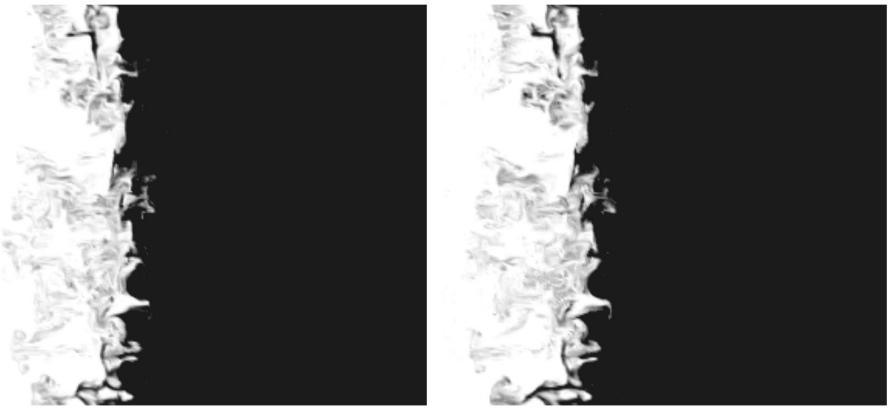

(c) M5 (d) W5

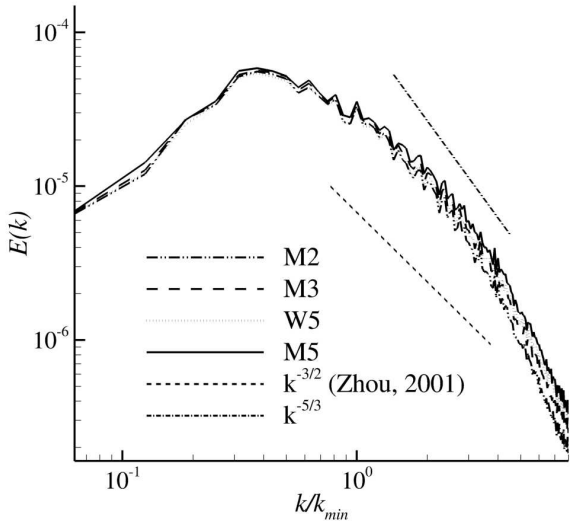

(e) TKE spectrum

FIGURE 5.13: Contour plots of the density (x-z plane, $y = \pi$) and spectrum of turbulent kinetic energy from the incompressible solver after the numerical transition is operated at $\tau = 100$.

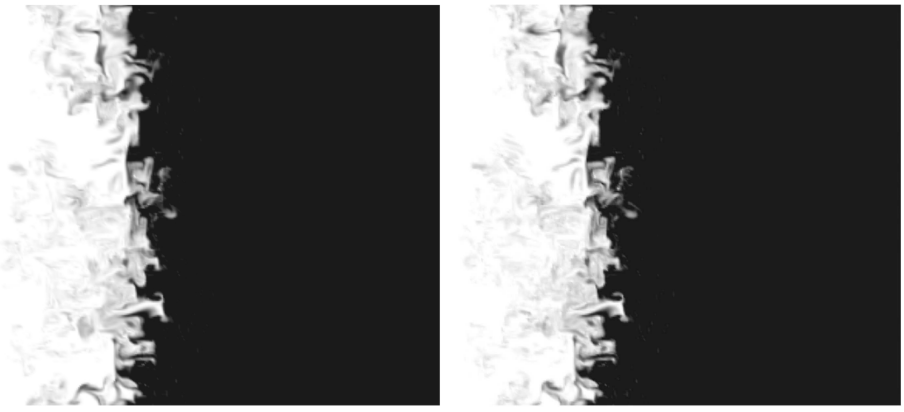

(a) M2 (b) M3

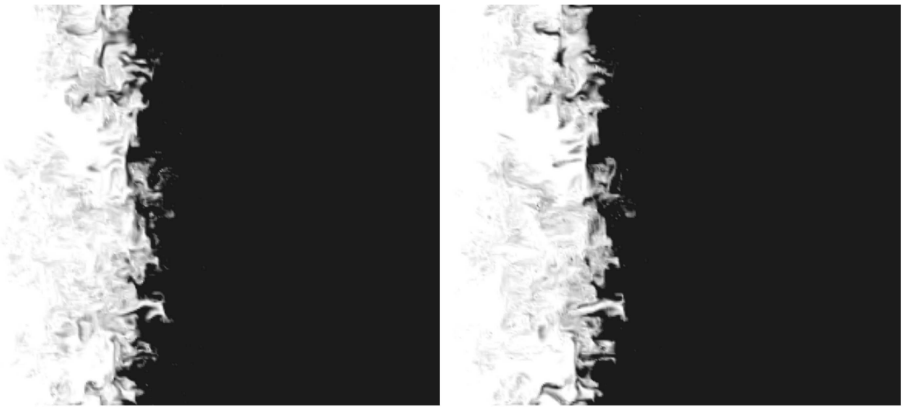

(c) M5 (d) W5

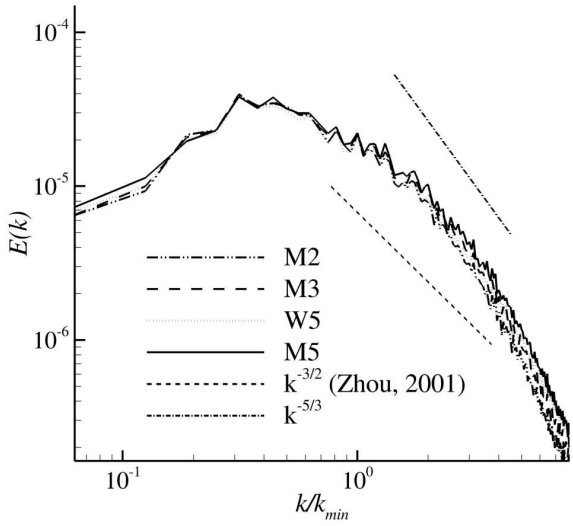

(e) TKE spectrum

FIGURE 5.14: Contour plots of the density (x-z plane, $y = \pi$) and spectrum of turbulent kinetic energy from the incompressible solver after the numerical transition is operated at $\tau = 150$.

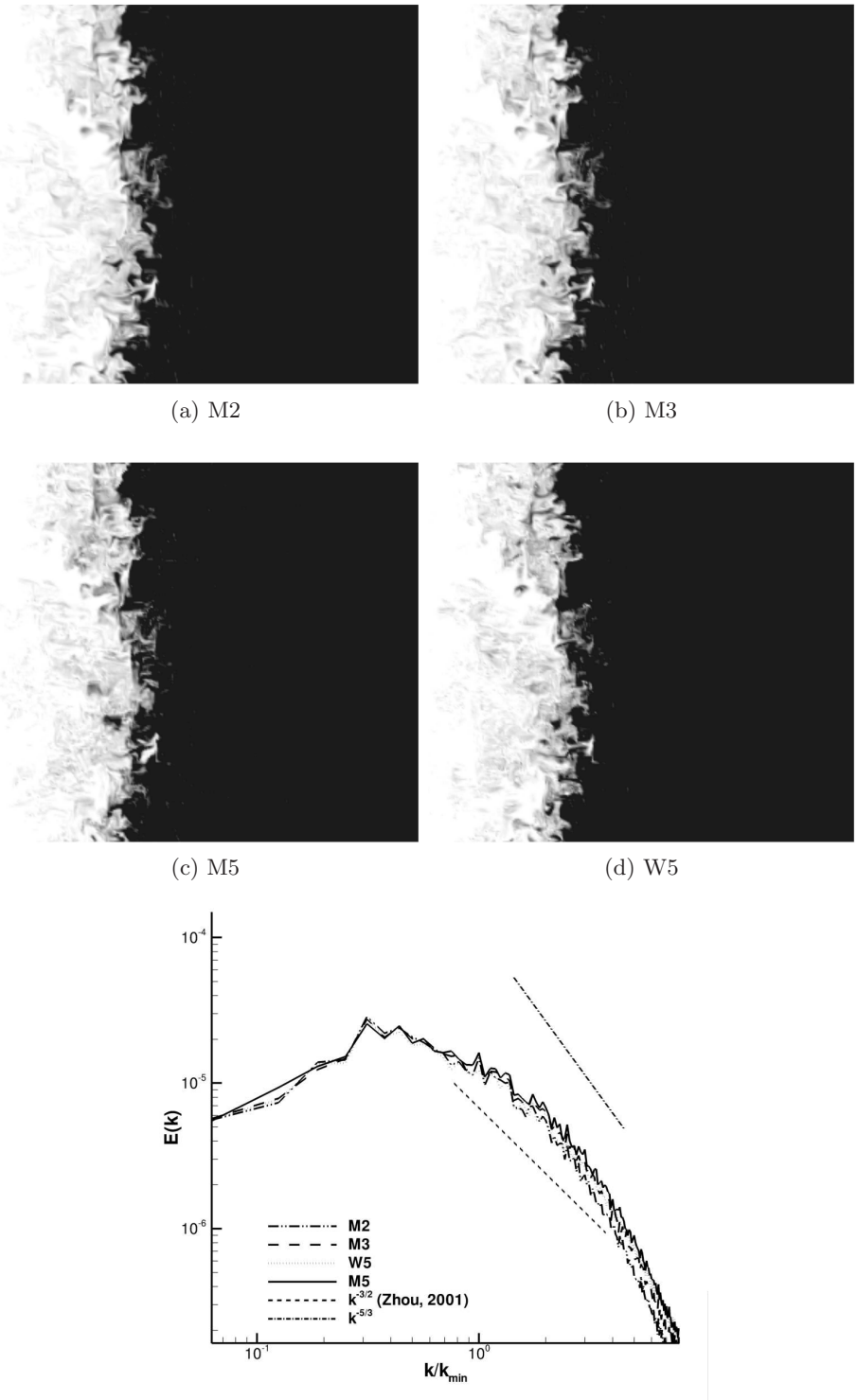

(a) M2 (b) M3

(c) M5 (d) W5

(e) TKE spectrum

FIGURE 5.15: Contour plots of the density (x-z plane, $y = \pi$) and spectrum of turbulent kinetic energy from the incompressible solver after the numerical transition is operated at $\tau = 200$.

of Mathematica was used. Assuming a functional relationship of the form:

$$W/\lambda_{\min} = C(\tau - \tau_0)^{\theta} \,, \tag{5.19}$$

this feature allows to obtain the best fit line optimising the values of C, τ_0 and θ and reducing the mean square difference. Results are fitted starting from $\tau = 50$.

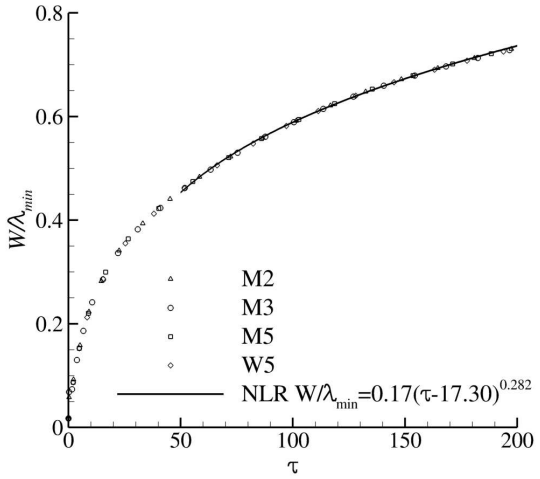

FIGURE 5.16: Growth of the integral length of the mixing zone according to the different reconstruction schemes. The solid line represents the data fit computed by using the nonlinear regression package from Mathematica.

The value of the coefficients computed by the NLR analysis on the results obtained with different high-resolution methods are presented in Table 5.3.

Rec. scheme	C	τ_0	θ
M2	0.171 ± 0.00033	17.75 ± 0.101	0.281 ± 0.00033
M3	0.173 ± 0.00046	18.37 ± 0.139	0.278 ± 0.00047
M5	0.168 ± 0.00026	17.12 ± 0.102	0.280 ± 0.00038
W5	0.170 ± 0.00033	17.31 ± 0.101	0.282 ± 0.00033

TABLE 5.3: Values of the coefficients and estimated errors for RMI growth $W/\lambda_{\min} = C(\tau - \tau_0)^{\theta}$ computed by NLR analysis starting from $\tau = 50$.

The value $\theta \approx 0.282$ found by the incompressible simulations is in very good agreement with the range of values estimated by the theoretical analysis but simulations run for a longer time are needed in order to capture a more reliable value.

5.4.3 Comparison against compressible simulation

Simulations of MM-RMI obtained from the hybrid code (H) are compared against fully compressible numerical analyses (C), which were carried out simply by letting the compressible solver run without applying the transition. The compressible run with the finest grid took roughly 90 days of computations on 64 processors to reach $\tau = 500$, whereas the hybrid solver needed just about 10 days to reach $\tau = 1500$ on the same amount of nodes. Already from this numbers, it is possible to state that the potential gain of efficiency using the hybrid solver is huge.

Unless differently specified, the results presented in the following sections refer to the finest grid.

Numerical setup and transition

For this test case, the NB perturbation is applied to two different grids with different resolution and different length. The dimensions of the cross section of the domains is the same $0 < y < 2\pi$ and $0 < z < 2\pi$, whereas the x-length varies depending on the resolution of the grid. $0 < x < 6\pi$ is chosen for the coarse mesh, which has a resolution of $768 \times 256 \times 256$, whereas $0 < x < 2.8\pi$ is chosen for the fine grid, with a resolution of $720 \times 512 \times 512$ cells. The reason underlying the difference in the x-dimension is that it is important to make sure that the mixing layer evolves far from the extremities of the domain. In fact, the range of wavelength included in the perturbation is dependent upon the grid spacing[2] and therefore the NB perturbation applied to a finer grid will produce a shorter mixing layer, in absolute value, than a coarser grid at a given instant in time.
The initial position of the shock (X_s) and the of the interface (X_i) changes depending on the grid. For the coarse grid, the interface is at $x + \wp(y, z) = 9.0$ and the shock is at $x = 8.5$, whereas in the fine grid the interface is initialised at $x + \wp(y, z) = 4.0$ and the shock position is at $x = 3.5$. The impact is of H-L type (Youngs, 2004) and the Mach number of the incident shock wave travelling across the heavy fluid was 1.84. The initial state of the numerical field is the following:

$$0.0 < x < X_s \quad (\rho, u, p) = (6.38, -6.15, 4000) \ , \tag{5.20}$$

$$X_s < x < X_i + \wp(y, z) \quad (\rho, u, p) = (3.0, -29.16, 1000) \ , \tag{5.21}$$

$$x > X_i + \wp(y, z) \quad (\rho, u, p) = (1.0, -29.16, 1000) \ . \tag{5.22}$$

The reconstruction method employed at the cell interfaces is that of M5 in the hybrid solver and M5+LM in the compressible case. The time-marching scheme chosen is the RK-SSP second order accurate, which allowed the simulation to run with $C = 0.5$ for the compressible stage and $C = 0.2$ for the incompressible part and the target residual for the pressure equation was set to $r = 10^{-4}$. The numerical transition was operated with the same modalities as in the SM case: $M_{\mathrm{NT}} = 0.2$. The switch took place at $t_{\mathrm{NT}} \approx 0.156$ s, which corresponds to the normalised time τ of approximately 5.78 and 11.56 for the grids 256 and 512 respectively. The densities of the incompressible fluids computed are: $(\rho_1)_{\mathrm{I}} = 5.23$ and $(\rho_2)_{\mathrm{I}} = 1.82$. The status of the interface at the end of the compressible part of the simulation is presented in Figure 5.17. The inversion of phase due to the heavy-to-light nature of the test case has already taken place and the mixing layer is growing linearly, as shown by the graph in Figure 5.18.

Mixing and self-similarity

Snapshots of the mixing layer obtained with H and C techniques at different instants in time (for $t > t_{\mathrm{NT}}$) are presented in Figure 5.19.

[2] All the grids employed for the simulations presented in this thesis have cubic cells with $\Delta x = \Delta y = \Delta z$.

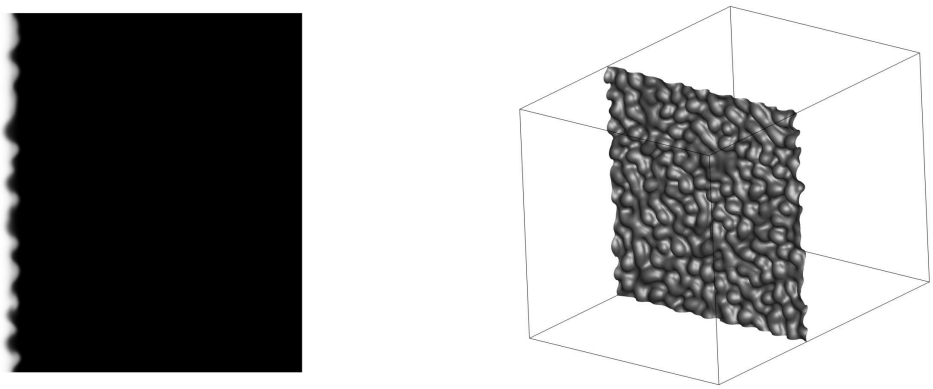

FIGURE 5.17: Interface deformation (isosurface $V_f = 0.5$) at the instant of the numerical transition between compressible and incompressible model for the 256 cross-section grid ($\tau \approx 5.78$).

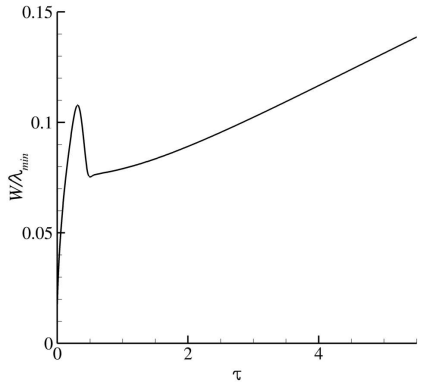

FIGURE 5.18: Growth of the mixing layer during the compressible stage for the 256 cross-section grid ($0 < \tau < 5.78$). The rapid decay after the overshot at $\tau \approx 0.3$ is due to the collision between a shock wave and the fluids interface.

Comparing the solutions given by the solvers at the same instants in time, various considerations can be drawn. For $\tau \leq 200$ (Figure 5.19a, 5.19b and 5.19c), the mixing layers from C (left-side) and H (right-side) appear almost equal. In fact, both small and large scale structures in the C mixing layer (on the left-side) are clearly distinguishable in the H mixing layer and vice-versa. Consistently with the SM case, it is also possible to notice that the latter appears sharper than the former, which show a more blurred ans fuzzy line between the gasses. On the other hand, for $\tau > 200$ the differences between the numerical models become more important and the codes agree only on the large scales structures. In particular, the compressible mixing layer appears more homogeneous with a more gradual and smooth change in V_f going from one fluid to the other, whereas the incompressible looks sharper with more clearly distinguishable turbulent structures.

The non-dimensional extension of the mixing zone can computed by averaging the volume fraction on the y-z planes of the domain and by plotting it against the x dimension normalised by W (Figure 5.20). At early time ($\tau = 50$), good agreement between the solver is present on the bulk of the mixing layer and also on the spikes side. Nevertheless, at later times ($\tau \geq 100$) the situation is reversed as the H solution

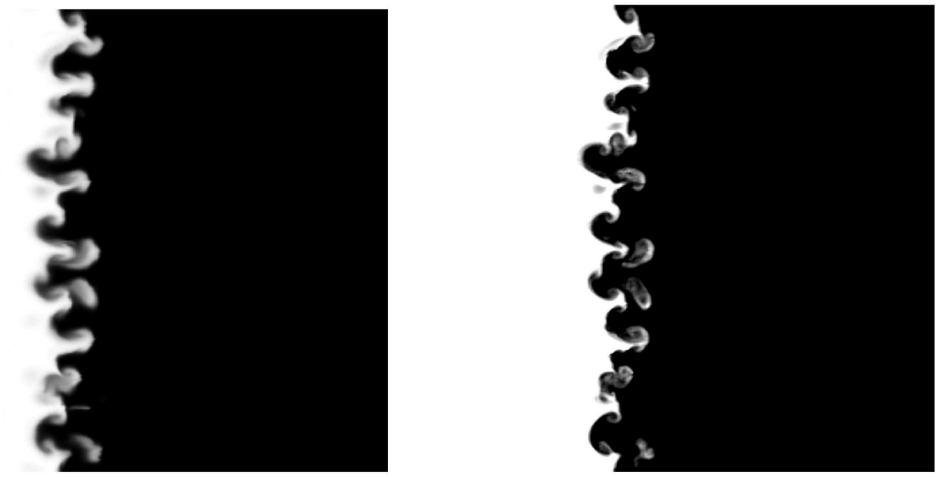

(a) $\tau = 50$

(b) $\tau = 100$

(c) $\tau = 200$

FIGURE 5.19: Two-dimensional visualisations of compressible (left) and hybrid (right) V_f contour plots. For $\tau = 1000$ and $\tau = 1500$ only hybrid visualisations are available. The plots are clipped to highlight the mixing layer.

(d) $\tau = 300$

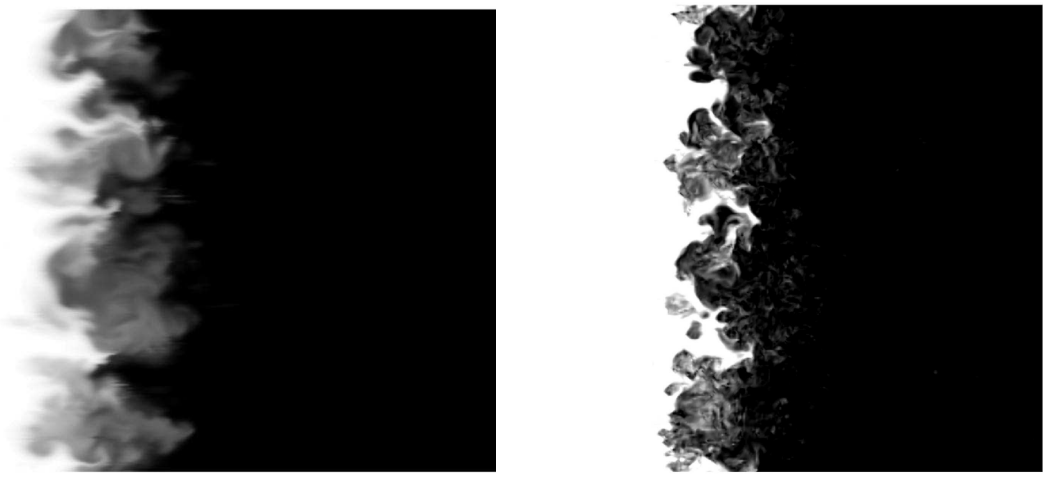

(e) $\tau = 400$

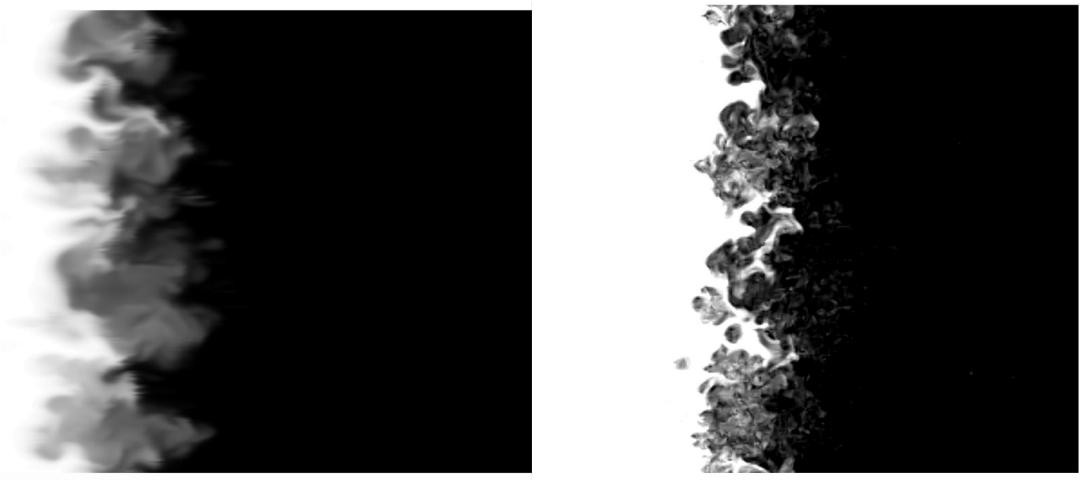

(f) $\tau = 500$

FIGURE 5.19: *(continued)*

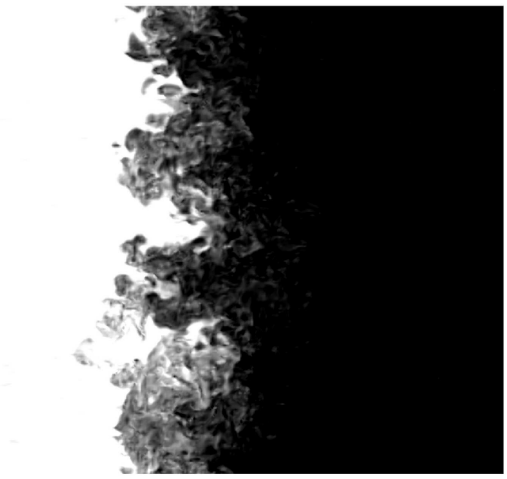

(g) $\tau = 1000$. Only hybrid plot.

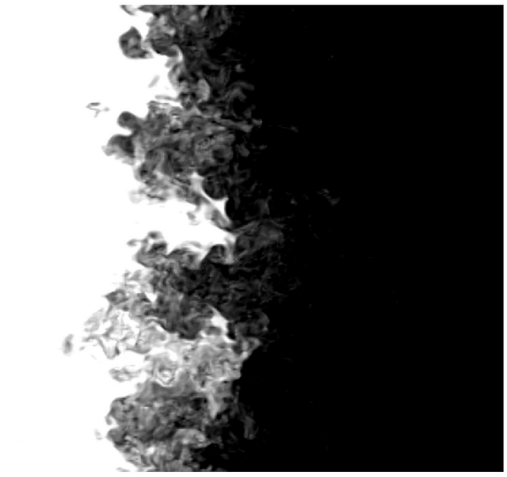

(h) $\tau = 1500$. Only hybrid plot.

FIGURE 5.19: *(continued)*

predicts a less gradual initial decrease of V_f, whereas according to the C case it is more rounded. The dashed and solid lines then join each other again for $V_f \lesssim 0.6$, with excellent agreement on the bubbles side. The figure includes also the compressible profiles obtained by Thornber et al. (2010). It is interesting to notice how these agree with the H profiles on the bubbles' side, whereas they matches the C profile on the spikes' side. This can be explained by the fact that the perturbation employed in our computation is scaled differently than the one used by the authors and this an have a potential infuence on the extremities of the mixing layer. Nevertheless, overall agreement is good.

It is possible to obtain information about the self-similar growth of the mixing layer by plotting on two distinct graphs the compressible and hybrid profiles presented in Figure 5.20.

Looking at Figure 5.21, it is clearly visible by the collapse of the profiles that, according to both compressible and hybrid solutions, the evolution of the bulk of the mixing layer becomes self-similar at $\tau \approx 250$, whereas the two extremes of the mixing layer require

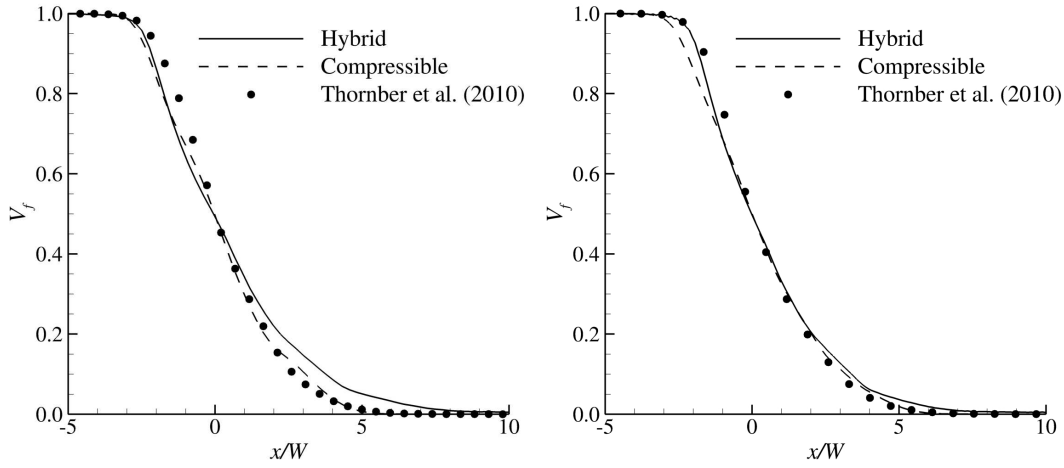

(a) $\tau = 50$ (b) $\tau = 100$

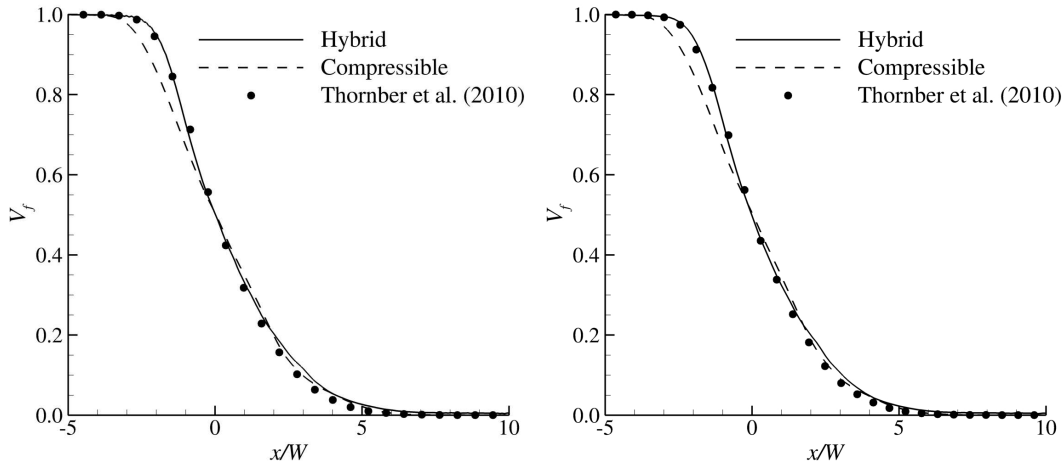

(c) $\tau = 200$ (d) $\tau = 300$

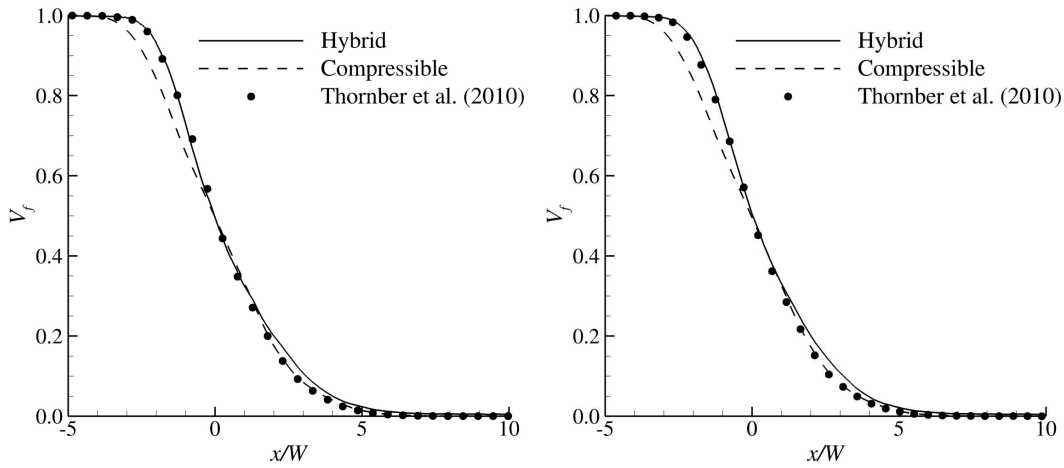

(e) $\tau = 400$ (f) $\tau = 500$

FIGURE 5.20: Profiles of V_f averaged on the x-planes (512 grid).

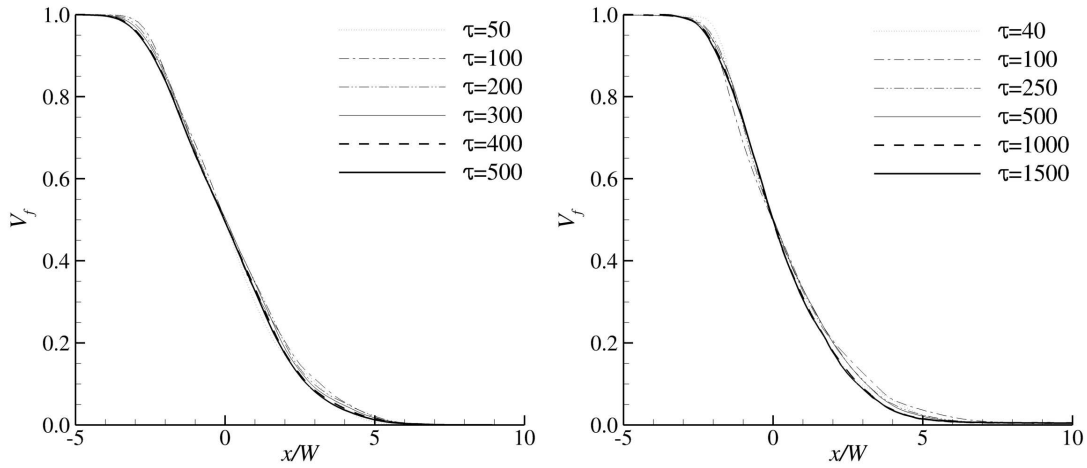

(a) Compressible (b) Hybrid

FIGURE 5.21: Profiles of volume fraction of specie one, averaged on the x-planes, plotted against the direction of the shock propagation normalised by the integral length of the mixing layer at significant instants of dimensionless time (finest grid).

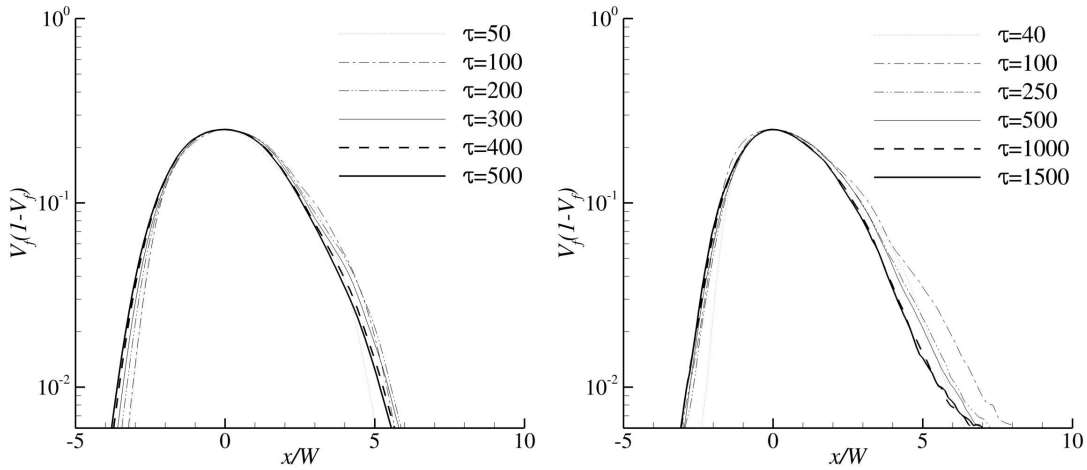

(a) Compressible (b) Hybrid

FIGURE 5.22: Profiles of $\overline{V_f}(1-\overline{V_f})$, averaged on the x-planes, plotted against the direction of the shock propagation normalised by the integral length of the mixing layer at significant instants of dimensionless time (finest grid).

more time to achieve this regime. The comparison is made clearer by plotting the trends of the quantity $\overline{V_f}\left(1-\overline{V_f}\right)$, which are presented in Figure 5.22. Later in time, also bubbles and spikes settle to a self-similar behaviour. In fact, it is necessary to wait until $\tau \approx 350$ (not shown for clarity) to see a better collapse of both C and H profiles on the left-side of the graph, which represents the growth of the bubbles. In the compressible results, in agreement with Thornber et al. (2010), the spikes do not become self-similar by the end of the simulated time. However, thanks to the new hybrid technique, it is possible to notice that also the right-side of the profiles starts

to develop in a self-similar manner at $\tau \approx 600$. This difference in the behaviour of the extremities of the mixing layer is caused by the difference in density, therefore in momentum, carried by bubbles and spikes. This makes the profiles of volume fraction asymmetric with respect to the centre of the mixing zone. The higher momentum of the spikes generates coherent vortex rings that travel away from the interface and which breakdown and become part of the mixing layer only at later time in comparison with the bubbles. As it was pointed out in Thornber et al. (2010), a much finer grid resolution is necessary to correctly capture the extremities of the mixing layer since the fine structures in this region of the domain make the results extremely sensitive to the dissipative characteristics of the numerical scheme at high wavenumbers. However, it is interesting to notice that treating the hypothesis of self-similar development of the instability at late-times seems to be effectively valid. In fact, bearing in mind that the spikes side is the last portion of the mixing layer to achieve self-similarity, for the test case considered in this thesis, the whole mixing layer does become self-similar when $\tau > 600$. Consistently with the above considerations, for higher Atwood numbers this time is expected to increase due to the higher momentum carried by the spikes.
Figure 5.23 shows the growth of the normalised integral length of the mixing layer with respect to the non-dimensional time τ according to the two solvers.

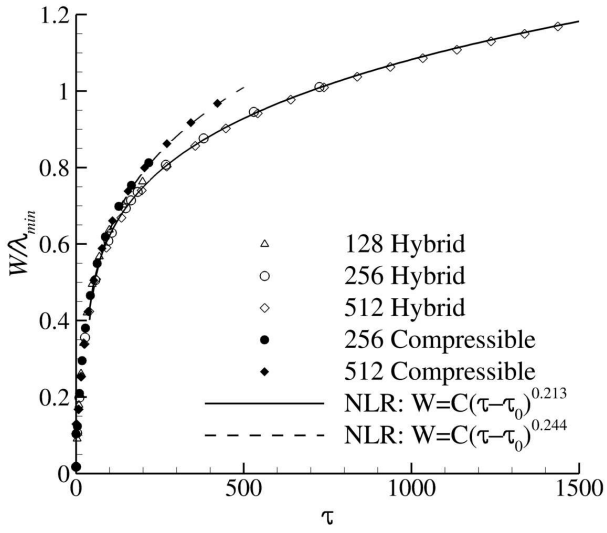

FIGURE 5.23: Evolution of the integral length of the mixing zone W for hybrid and fully compressible simulations from Thornber et al. (2010).

Similarly to the considerations above, when τ is included between τ_{NT} and 150, the codes show good agreement on W/λ_{min}. On the other hand, at later times the compressible solver computes a faster growth with a consequent larger mixing layer. The growth exponents obtained from the H and C simulations are presented in Table 5.4, together with compressible results available in the literature. The C growth exponent, is found in good agreement with both the experiments by Dimonte and Schneider (2000) and the compressible simulations from Thornber et al. (2010). Excellent agreement is present with Youngs (2004), who obtained $\theta = 0.243$ for a long-time compressible simulation. In fact, the discrepancy between Youngs' and our simulations is extremely small (~ 0.001) and stating that the results almost match each other would not con-

Source	Interpolation interval	θ
Compressible (C)	$40 < \tau < 500$	0.244
Hybrid (H)	$40 < \tau < 500$	0.225
	$40 < \tau < 1500$	0.213
Thornber et al. (2010) (compressible)	$40 < \tau < 500$	0.260
Youngs (2004) (compressible)	not specified	0.243
Dimonte and Schneider (2000) (experiments)	not specified	0.25 ± 0.05

TABLE 5.4: Growth exponent values for compressible and hybrid simulations and experiments.

tradict the numbers presented in the table. The H solution predicts a lower exponent independently from the interpolation interval for τ. Nevertheless, an important note is that the value of θ obtained for $40 < \tau < 500$ is not retained when the interpolation time is extended to $\tau = 1500$, as the coefficient decreases of about 0.012. This raises the doubt on whether or not the assumption that the values of the compressible θs are stable when the interpolation time is extended. Longer compressible simulations would be needed to answer this question. Comparing the hybrid results with the various analytical theories, the H code predicts a value which is more consistent with Barenblatt's suggestion $\theta = 2/3 - \nu$, where ν is a viscous correction which in this case is $\nu \approx 0.46$. It needs to be pointed out that the solid line in Figure 5.23 lies slightly above the simulation during the late-stage, therefore modification of the NLR analysis are expected in the case that the time covered by the simulation is longer. Even though the results compared in the table were obtained using a range of very different methods, it is very encouraging to notice the overall agreement with the incompressible prediction on this important parameter. It needs to be pointed out that the values obtained are significantly lower than the range proposed by Zhou (2001), which predicts a lower value of 2/3. However the agreement between the numerical and the experimental results is surely a very important point and it represents a further confirmation to the generally accepted viscous correction theory by Barenblatt et al. (1983) which takes into account the dissipative nature of the flow.
Finally, Figure 5.24 shows the evolution in time of the molecular mixing fraction, Θ, and of the mixing parameter, Ξ, defined as:

$$\Theta = \frac{\int \overline{V_f(1 - V_f)}\, dx}{\int \overline{V_f}\left(\overline{1 - V_f}\right) dx}\,, \tag{5.23}$$

$$\Xi = \frac{\int \overline{\min(V_f, 1 - V_f)}\, dx}{\int \min\left(\overline{V_f}, \overline{1 - V_f}\right) dx}\,. \tag{5.24}$$

The former is an index of the total reaction rate for a slow reaction, whereas the latter is the equivalent parameter for a fast reaction.
Both the coefficients follow a similar trend, even though they present a higher value according to the compressible simulation. At early-time, they drop very quickly down

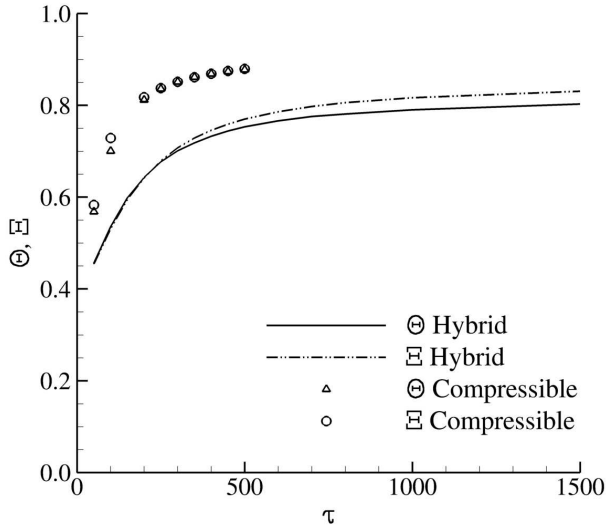

FIGURE 5.24: Evolution of the molecular mixing fraction, Θ, and of the mixing parameter, Ξ, in time for the 512 cross-section grid.

to 0.44 at $\tau \approx 35$ and successively the values increase approaching an almost constant state for $\tau > 500$. In fact, the curves are not perfectly flat but they are characterised by a very low positive slope which decreases with time. Table 5.5 summarise the asymptotic values and compare them against results from Thornber et al. (2010).

Source	Θ	Ξ
Compressible (C)	0.87	0.87
Hybrid (H)	0.74	0.80
Thornber et al. (2010) (compressible)	0.84	0.84

TABLE 5.5: Values of the mixing parameters for C and H simulations compared against the compressible simulation from Thornber et al. (2010).

The H solution predicts lower Θ and Ξ and moreover, differently to the C solution, they settle on different values, with $\Theta < \Xi$. This is reflected by the contour plots in Figure 5.19. In fact, as it was pointed out at the beginning of the paragraph, the compressible mixing layer appears more mixed that its incompressible variant.Looking at the compressible solution, Thornber et al. (2010) found a slightly lower value of the coefficients compared to our C results. However, in both cases Θ and Ξ tend to the same number.

Turbulent kinetic energy

More information concerning the physics of the flow and the behaviour of the numerics can be obtained by looking at the spectrum of TKE calculated on the y-z plane at different moments in time (Figure 5.25 and 5.26). The theory of Zhou (2001) for the decay of the TKE spectrum for shock-driven flows assumes that, at very late-times, the turbulent motion inside the mixing layer loses the influence of the initial shock wave, developing in an homogeneous and isotropic manner (see §2.2.2). This implies that the

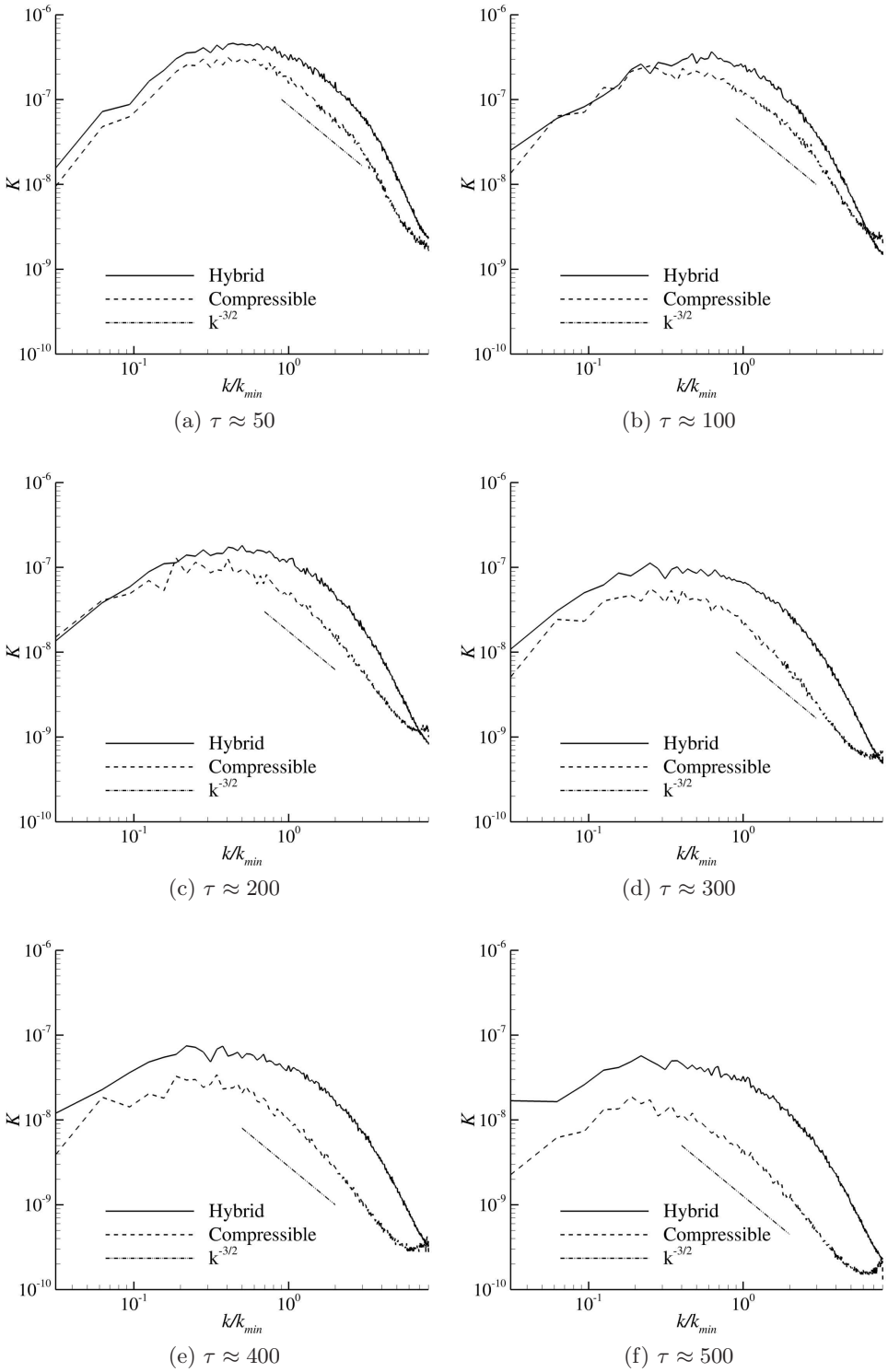

(a) $\tau \approx 50$ (b) $\tau \approx 100$

(c) $\tau \approx 200$ (d) $\tau \approx 300$

(e) $\tau \approx 400$ (f) $\tau \approx 500$

FIGURE 5.25: Comparison between C and H TKE spectrum at different instants in time.

$k^{-3/2}$ decay, which was analytically found by the author, should turn to the classic Kolmogorov's $k^{-5/3}$ as the time passes. Figure 5.25 shows the comparison between C and H spectrum for different values of τ. As it was previously pointed out, at earlier times ($\tau \leq 100$), the simulations are in good agreement. The C solution appears less dissipative as the amount TKE is slightly lower, nevertheless the spectra appear consistent between each other across the range of wavenumbers. A small turn-up typical of the low-Mach number correction is visible in the dissipation range of the compressible spectrum. At $\tau = 100$ there is very good agreement on the energy distribution across the energy containing scales, although the peak in the C case has already moved from $k/k_{\min} \approx 0.7$ ($\tau = 50$) to $k/k_{\min} \approx 0.2$. This shift is slower in the H case as only at $\tau = 400$ the peak of the incompressible spectrum reaches this point. At $\tau = 200$ there still is very good agreement in the energy containing range of the spectrum, but the C sub inertial range starts to move away from the hybrid prediction and at later times ($\tau \geq 300$) the codes progressively diverges also on the prediction of the larger scales energy distribution, with the H solver predicting a higher amount of TKE across the wavenumbers. Moreover, the compressible turn-up at high wavenumbers typical of the LM correction becomes more and more noticeable. Even though the general trend of the incompressible spectra is more rounded and less sharp than the C case, it is possible to observe that the subinertial range predicted by the theory is present in the limits of $1 \lesssim k/k_{\min} \lesssim 4$, whereas in the compressible case the $k^{-3/2}$ decay extends from $k/k_{\min} \approx 0.3$ to almost the end of the spectrum, before the turn-up. As it was pointed out in Thornber et al. (2008b), even though the low-Mach correction represents a clear improvement to the compressible solver, the drawback is that it does not provide enough dissipation in this part of the spectrum, resulting in an unphysical turn-up of the curve at high wavenumbers. This implies that the compressible small-scale features visible in Figure 5.19 might potentially be a numerical artefact rather than physical structures developed by the mixing process. Also the incompressible spectra do show this behaviour but it is much less noticeable. From this point of view, the approach presented in this thesis seems to lie in between the classical compressible solutions with and without LM correction since it extends the subinertial range of the spectrum without being excessively dissipative and without the inconvenience of the high wavenumbers turn-up.

A clearer evolution of the C and H spectra is presented in Figure 5.26. From these graphs, it appears clearer that the decay rate of the subinertial range at early-times follows Kolmogorov's decay rate $k^{-5/3}$ and only later in the simulation the spectra settle on a steady-state evolution in correspondence of $k^{-3/2}$. As it was already noticed, the peak of energy is not constant either and it moves progressively from an initial $k/k_{\min} \approx 0.6$ at $\tau = 40$ to $k/k_{\min} \approx 0.1$ at $\tau = 1500$. This shift is slower according to the hybrid solution. At high wavenumbers ($k/k_{\min} > 3$), the rate of decay of TKE increases, but at the very end of the spectrum, $k/k_{\min} \approx 8$, a slight turn-up of the energy is observable also in the hybrid solution. This part of the spectrum still represents the unknown since there is no theory which describes the dissipation range for shock-induced turbulent mixing. As it is observable from the general trend of the spectra in time, at the end of the simulation there is no evidence of memory loss of the initial shock and the mixing still behaves in an inhomogeneous and anisotropic manner. Further investigation on this is carried out by considering the turbulent kinetic energy

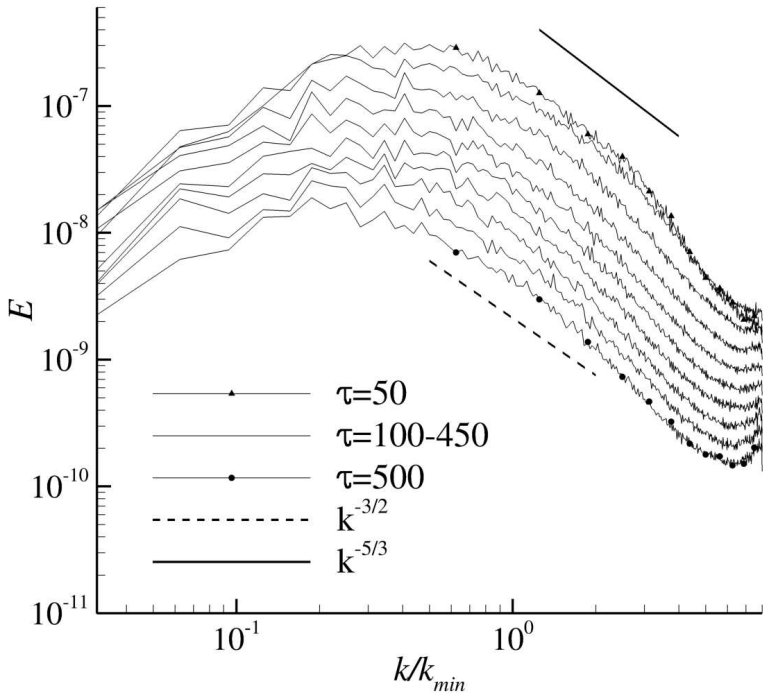

(a) Compressible solution. Spectra for $\tau = 50$, 100, 150, 200, 250, 300, 350, 400, 450 and 500.

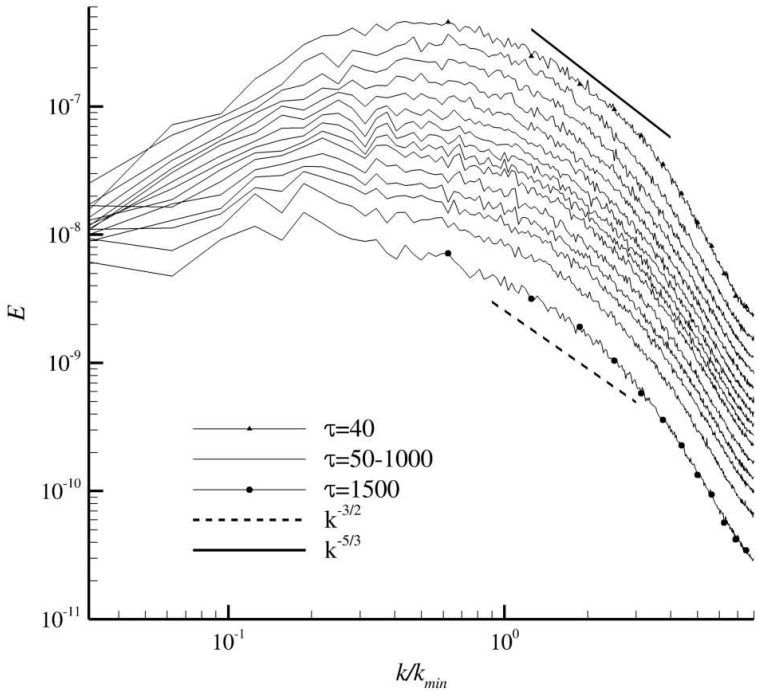

(b) Hybrid solution. Spectra for $\tau = 40$, 50, 100, 150, 200, 250, 300, 350, 400, 450, 500, 600, 700, 800, 1000 and 1500.

FIGURE 5.26: Compressible and hybrid spectra of radial turbulent kinetic energy averaged on y-z planes in the bulk of the mixing layer for the 512 cross-section grid and $k^{-3/2}$ guide-line analytically predicted by Zhou (2001).

components defined as:

$$K_x = \frac{1}{2}\int \rho(u-\overline{u})^2\, dV\ , \qquad K_y = \frac{1}{2}\int \rho v^2\, dV\ , \tag{5.25}$$

where,

$$\overline{u} = \frac{\displaystyle\int_{y,z} \rho u\, dS}{\displaystyle\int_{y,z} \rho\, dS}\ . \tag{5.26}$$

The trends of these quantities are reported in Figure 5.27.

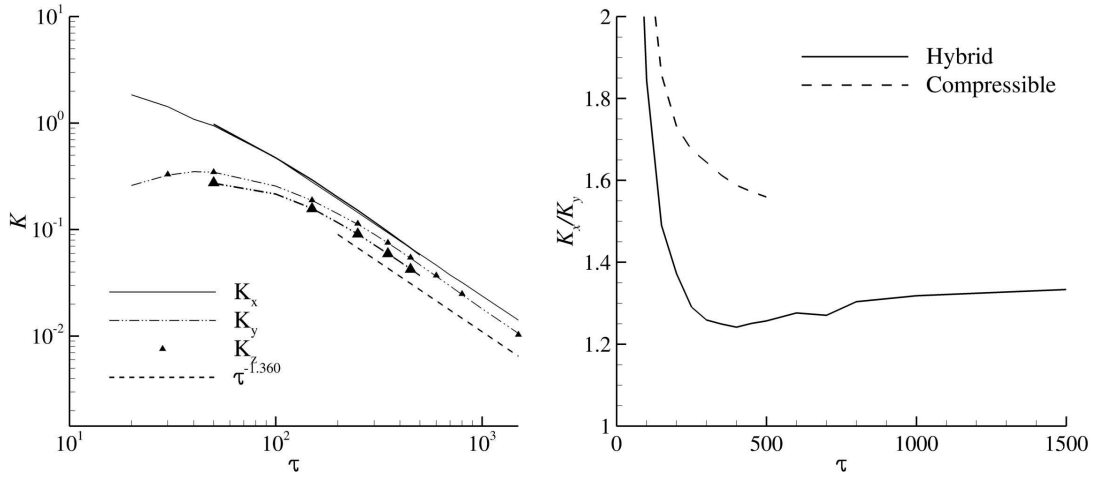

(a) TKE components. (b) K_x to K_y ratio.

FIGURE 5.27: Evolution in time of the turbulent kinetic energy components and of the ratio K_x/K_y for the 512 cross-section grid. The ticker lines in represent the compressible solution, whereas the thinner lines represent the hybrid computations.

Excellent agreement between the codes is noticeable on the evolution of the x-component (Figure 5.27a). At early-times the anisotropy of the flux is very strong in the numerical field, since the K_x is one order of magnitude bigger with respect to K_y and K_z. This is more evident according to the C solution as K_y and K_z have a slightly lower value. As the time goes by, according to both solutions, the behaviour of the longitudinal and radial components follows different trends. The former constantly decreases, whereas the latter presents an initial growth until $\tau \approx 40$ and successively it diminishes until the end of the simulation. At $\tau \approx 250$ the rate of decay of the components becomes almost identical, indicating the achievement of self-similar regime. In fact, this moment in time coincides also with the achievement of self similarity by the bulk of the mixing layer (see previous paragraph). Considering that the integral length of the mixing zone scales with t^θ, from the dimensional analysis, it is possible to find an exponent for the decay of the TKE. Recalling Equation (2.1) and considering that the decay of turbulent kinetic energy is proportional to the width of the mixing layer multiplied, it is possible to write that $W dK/dt \propto t^\theta K^{3/2}/t^\theta$, which gives $K \propto t^\theta t^{2\theta-2} = t^{3\theta-2}$. The

same result can also be found by considering that $\sqrt{K} \propto dW/dt \propto t^{\theta-1}$. Considering that the hybrid solver returned a growth coefficient $\theta = 0.231$, the turbulent kinetic energy is supposed to scale with $t^{-1.36}$. From Figure 5.27a, it is clear that the decay of K is consistent with the prediction in both C and H solutions. As a consequence of the evolution of the TKE in time, the hybrid ratio between the K_x and the radial components decreases very quickly until it reaches a minimum of 1.24 at $\tau \approx 400$ for then increasing very slowly. For $800 < \tau < 1500$, K_x/K_y is included in the range 1.315 ± 0.015 with the tendency to increase. According to the compressible analysis, this value settles around 1.5, but at $\tau = 500$ the transient is still ongoing. The analysis of the TKE components is perfectly consistent with what was noticed by looking at the spectra. Even though the trend of these quantities results in a constant and basically equal decay, at the end of the simulation, there is no sign of loss of anisotropy in the flow field as the x component of the turbulent kinetic energy is higher than the radial contributions. Compressible simulations by Thornber et al. (2010) gave very similar results as the flux was never found to lose the anisotropy caused by the incident shock wave. However, the asymptotic ratio K_x/K_y found by the authors became stable around the lower value 1.25 ± 0.02.

5.5 Summary

The shock-driven nature of RMI and its free decay in time causes the Mach number of the flow field to be characterised by a broad range of values during the entire evolution of the instability. A preliminary analysis of the compressibility of the numerical field showed that M is high ($M > 1$) during the initial stage and successively it decreases until the incompressible regime is achieved ($M < 0.3$).
Studies on the transition from compressible to incompressible evolution of the mixing layer for single-mode perturbations which are present in the literature proposed an analytical relation to estimate the instant when the regime starts to change. However, a preliminary numerical investigation presented in this chapter showed that it is possible that shock waves may still be present inside the numerical field at this moment in time. This does not allow to change the physical model since the field must be incompressible everywhere, therefore a small delay of the numerical transition with respect to the 'perfect instant' is introduced. This issue, added to the fact that no prediction on the transition from compressible to incompressible evolution is available for multi-mode cases, brought to define the criterion for the numerical transition based on highest local Mach number inside the numerical field.
The first step to test the technique was to apply the switch to a simple two-dimensional single-mode test case. The hybrid simulations were compared with fully compressible results obtained by the same initial conditions. The solvers resulted in excellent agreement when integral quantities were considered, whereas a sharper and less diffused density field was computed by the incompressible stage of the hybrid solver. In this case, the mushroom-shaped mixing layer typical of single-mode RMI was more detailed and better defined.
Of higher interest and relevance is the application of the numerical switch to the more complex three-dimensional multi-mode RMI, where the perturbation is made by protuberances of different wavelengths and amplitudes. Initially, a light-to-heavy fluid impact

was taken into consideration in order to compare different high-resolution methods. The integral quantities did not show relevant variation, but the spectrum of the turbulent kinetic energy presented different decay slopes at high wavenumbers, highlighting the different dissipative characteristics of each reconstruction scheme. Lower order of accuracy resulted in a faster decay of the turbulent kinetic energy, with a consequent loss of the small-scale structures inside the mixing layer. Successively, a heavy-to-light impact was simulated in order to compare the hybrid and the compressible solutions. A different behaviour from what was noticed in the single-mode case was found. The growth of the instability in time is faster according to the incompressible model but with a slightly lower growth exponent. According to theoretical results, the TKE spectrum presented the expected modified subinertial range, even though this was less extended over the wavenumbers than the compressible analyses which, on the other hand, do not present any clear dissipation range. Moreover, the amount of turbulent kinetic energy detected by the compressible analyses resulted to be higher.
The last consisted in running the hybrid simulation for a very-long time in order to address the appearance of self-similarity in the evolution of the instability and in order to compare the flow physics against the compressible results across the simulated time. Compressible and hybrid solutions were found in extremely good agreement, especially at early times ($\tau < 200$), in a number of parameters (i.e. mixing layer visualisations, volume fraction profiles, TKE spectra and decay). However, some differences were also detected, i.e. growth exponent and amount of TKE in the numerical field. Extremely good agreement was found in the general physics of the flow as the mixing layer achieved self-similar development in both cases and with the same time scale. Contrarily to what theoretical analysis assumed, the TKE spectrum inside the mixing layer did not tend to return to a condition of homogeneous decay at late-time. In fact, although TKE components were found to decay with the same rate, a non negligible amount of anisotropy was still detected in the flux. This was even more evident in the compressible solution as the flow anisotropy detected was higher.
A final note on the computational efficiency is worth to be mentioned. The compressible simulation took approximately 90 days of computations on 64 processors to reach $\tau = 500$, whereas the hybrid solver needed just about 15 days to reach three times the simulated time on the same amount of nodes.

6

Conclusions and future work

6.1 Conclusions

The aim of this thesis was to design, implement and test a novel approach to simulate those flows which present an initial compressible flow field and become incompressible during their evolution. In particular, the investigation presented in this work was concerned with the Richtmyer-Meshkov Instability (RMI), a phenomenon which is of prime importance in events such as supernovae explosion and supersonic combustion. Although it is relatively easy to test and eventually to validate theories which model the early stage of RMI, the collection of reliable data concerning the late-time development, when the instability is believed to evolve in a self-similar manner, is a real challenge. In fact, both experiments and numerical simulations rarely last long enough in order for the mixing layer to achieve a fully turbulent state and the consequence is an important lack of data in the literature.
Exploring new paths for simulating flows where the Mach number spans from supersonic to incompressible values was motivated by the fact that compressible numerical methods manifest two issues when the numerical field is incompressible. The first is the cancellation error, which in Godunov-type methods consists in the production of an artificial acoustic wave that destroys the incompressible solution, whereas the second is the loss of time-marching efficiency due to the presence of negligible acoustic waves in the flow field. The latter reason represents the main obstacle to compressible long-time simulation of RMI. The approach here presented introduced a radically new point of view in comparison to the paths which have been investigated so far. In fact, it bypasses the two aforementioned issues as it is based on the principle of using the right solver at the right time, i.e. to start the simulation using a compressible solver and to switch to the incompressible numerical model when the field allows it.
The first step was to develop a new inviscid, incompressible solver within Cranfield's in-house code for ILES simulations Hirecom, that already comprised two compressible solvers. The incompressible method chosen was the pressure-projection technique, which together with the momentum equations solves an elliptic equation for the pressure and then uses this parameter to project the solution onto the divergence-free space, thus recovering the incompressible solution. Central to ILES simulations is the use of Riemann-solvers and high-resolution methods, which were initially created as shock-

capturing schemes in order to avoid spurious oscillation in proximity of discontinuities. In this work, three different compressible Riemann-solvers re-adapted for computing the incompressible fluxes across the cell interfaces were taken into consideration and were tested in conjunction with MUSCL and WENO reconstruction schemes with different order of accuracy. Parallel computation capability was also added to the solver through the use of MPI calls. This allowed the use of computational grids with more than 10^8 cells on Cranfield's HPC facility Astral.

RMI can be viewed as a purely incompressible event if the interface between the fluids is impulsively accelerated, for example, by the gravity force. This allowed to carry out some preliminary studies on the behavior of the various Riemann-solvers and reconstruction schemes employed by the incompressible solver. Two different ways of generating the initial impulse were considered. The first consists of an impulse of velocity derived from the linear analysis, whereas the second replicates numerically the falling tank technique used in the experiments by modeling the recorded gravity impulse which is imparted to the box when it bounces off of the springs. Using the velocity impulse for triggering the instability allowed to obtain results which were in excellent agreement with experiments. The growth of the instability was clearly included in the experimental envelope for all the parameters of interest, i.e. growth of the instability, spikes and bubbles. Slight overestimation of the spike growth was noticed with respect to the centre of the envelope. The comparison of the curves against another inviscid simulation of the same test case allowed to conclude that this was due to the assumption of perfect fluids within the code. In fact, the curves obtained from the solver presented in this thesis matched perfectly the prediction of the other inviscid simulation in the literature. On the other hand, when the numerical field was compared against the experimental images, differences were noticed in the roll-ups on the sides of the mushrooms, where viscous interactions are important. In particular, these vortexes presented less close-ups than expected and also their appearance changed drastically depending on the order of accuracy of the reconstruction scheme. After this study, the WENO scheme in its ninth-order of accuracy was dropped due to the excessive distance of the numerical field from the reality. The second initialisation technique was tested against results coming both from experiments and VIC simulations. The solver was found to overestimate the growth of the instability at mid- and late-time and this was found to be caused by an excessive deposition of baroclinic vorticity at the interface by the gravity impulse. It needs to be pointed out that, differently from the previous case, the experimental results were not included in an envelope as it happens when a number of tests are carried out, but only a single curve was available. In the single-mode perturbation, the viscous forces play an important role in the evolution of the instability since its growth is dominated by two big coherent structures which contain the heavy fluid that rolls up and the inviscid nature of the solver did not allow to correctly capture these features. Looking at the integral quantities of interest, the velocity impulse initialisation resulted to be a better triggering cause for the instability, independently from the Riemann-solver or the high-resolution scheme employed. The difference between viscid and inviscid results was not investigated further for a number of reasons. First, it has already been the object of investigation in the literature. Second, this thesis aimed to study the late-time evolution of MM-RMI, where the interface perturbation is closer to real cases than the single-mode, which is an idealised case of

study. The temporal dynamics of RMI when the interface presents protuberances of different wavelengths is different and characterised by wide range of scales which interact with the whole field of motion and the viscous forces becomes important only at very very-late times, which is not the target of the investigation of this work.
The numerical simulation of impulsive, or incompressible, RMI was of great importance mainly to assess the behavior of the Riemann-solvers considered and allowed to choose one of them to be used in the hybrid compressible-incompressible simulations. The numerical switch between the models to study the evolution of RMI is possible thanks to the existence of the two main stages which distinguish the development of the instability. The first is characterised by the fact that the compressibility effects carried by the shock waves on the mixing layer are strong, whereas the second involves the free decay of this part of the domain and the incompressible regime is achieved. A prediction for the instant of the transition between the two states in a single-mode case was proposed from experimental tests. Due to the fact that a criterion for the numerical switch had to be established, this possibility was initially explored, but a preliminary study showed that it can happen that shock waves are still present inside the numerical field even though the mixing layer evolves at low Mach number. This together with the fact that no estimation for the transition between states is present for a multi-mode perturbation brought to define a switching criterion based on the Mach number. The numerical transition had to take place when the Mach number in every cell was lower than a given threshold.
Applying the numerical switch to a SM test case showed how the hybrid and the fully compressible analysis agree excellently when the results are grid-independent. This outcome represents a very important point since the numerical methods and the models themselves are very different. Agreement resulted mainly from the comparison of the integral quantities of interest, but from a visual point of view the mushroom-shaped mixing layer computed by the incompressible solver resulted to be sharper and less diffused with respect to the incompressible solutions (with and without low-Mach correction). Moreover, a higher number of close-ups was predicted by the hybrid solver. From this preliminary study, no obstacle to the extension of the method to three-dimensional simulations was noticed, confirming the feasibility of the initial idea.
The first hybrid simulations with MM perturbation proved that the solver was able to return results in line with the theory. In particular, it was verified that subinertial range of the turbulent kinetic energy spectrum presented a decay which followed the modified $k^{-3/2}$. Depending on the order of accuracy of the reconstruction method employed, the extension of the subinertial range over the wavenumbers was found to be different. Lower order of accuracy returned a shorter wave interval, typically $1 < k/k_{\min} < 2.5$, whereas high-order methods extended the interval up to $k/k_{\min} \approx 4$.
Using an incompressible solver allowed to run the simulations for a range of time which has never been reached by compressible analysis. This permitted to explore the evolution of the instability until very late-times: $\tau = 1500$. For better comparison, compressible results were also produced by letting the same code to run the compressible solver without switching the model. These computations were run up to $\tau = 500$. Very good agreement was found between the solvers for a number of different parameters. First, by looking at the contour plots of the mixing layer, it was possible to notice that the compressible and hybrid mixing layer appeared very similar. In fact, for $\tau \leq 200$,

it was possible to recognise the same small and large scale structures in this part of the domain. At later times, the small scales features started to show differences with more mixing between the gases happening in the compressible mixing layer. Overall agreement was found in the plane-averaged volume fraction profiles along the direction of the shock propagation with the compressible results almost matching the results from Thornber et al. (2010). From these graphs, it was also possible to notice how bubbles, spikes and the bulf of the mixing layer achieve self-similar development at different instants in time. In fact, both the solutions predicted that the core of the mixing layer is the first to achieve this regime at $\tau \approx 250$, whereas bubbles need to wait until $\tau \approx 350$. No self-similar growth of the spikes was detected within the time range simulated by the compressible analysis. However, thanks to the hybrid technique it was possible to observe that also this extremity of the mixing layer becomes self-similar at $\tau \approx 600$. Good agreement was found on the growth exponent of the instability. The compressible simulation returned a value of 0.244, which is extremely close to the 0.243 found by Youngs (2004). On the other hand, two different values were computed for the hybrid simulation. In fact, if the range of time was considered to be the same as the compressible analysis, then the growth exponent was found to be 0.225. Whereas it assumed the value 0.213 if the interpolation time was extended to $\tau = 1500$. This raised a question mark about the reliability of the compressible results as a longer simulated time might lead to a decrease of the exponent. Nevertheless, these values are in reasonable agreement also with experiments and they add further confirmation to the widely accepted viscous correction $\theta = 2/3 - \nu$. A successive field of comparison was the evolution of the turbulent kinetic energy and its decay inside the mixing layer. The spectra computed from the numerical models were in good agreement at early times, especially in the energy containing range. The solutions at later times showed some differences both in the amount of energy, which was lower in the compressible case, and in the distribution of the energy across the wavenumbers. In fact, the hybrid solution presented a spectrum which appeared more rounded and less sharp across the regimes and the modified subinertial range comprised a wider range of wavenumbers, $0.3 < k/k_{\min} < 7$, in the compressible analysis. Theories assume that at very long-times the flow field should lose memory of the initial anisotropy given by the hit of the shock and the subinertial range should tend again to the $k^{-5/3}$ decay given by Kolmogorov's theory for homogeneous and isotropic decaying turbulence. No such thing was observed in both compressible and hybrid numerical simulations and no evidence of the loss of anisotropy was noticed. In fact, the radial components of TKE had different values with respect the the longitudinal contribution until the end of the simulated time as the energy in the x-direction was constantly higher than the radial counterparts by a factor of 1.315 ± 0.015 for the hybrid code and by approximately 1.6 in the compressible results. It was not possible to enstablish a precise value for the latter case as at $\tau = 500$ the transient was still ongoing. Using dimensional analysis, it was possible to predict the decay rate of the three components to be $t^{-1.36}$, which was then confirmed by both compressible and hybrid results. Once again, good agreement was found with Thornber et al. (2010) who estimated a decay of $t^{-1.26}$. Considering the right-side of the TKE spectrum, differences were expected as this part highlights the dissipative characteristics of the numerical method. Contrarily to the compressible solution, where an unphysical turn-up of the spectrum is present at high wavenumbers,

the hybrid solution presents a clearer dissipation range.
Overall, the flow physics computed by the hybrid code is in excellent agreement with the compressible simulations which were run for a much shorter time and with completely different methods. In addition, considering that in order for the hybrid solver to achieve a three-time bigger simulated time than the compressible simulation, this technique needed approximately 16% of the total computational time required by the compressible code. These notes surely are an encouraging and a promising starting point for future investigations.

6.2 Future work

The idea of linking a compressible with an incompressible solver may sound odd at first, but it is easy to realise that it can be feasible if a method which cancels unwanted compressible modes is available. The results presented in this thesis certainly proved that hybrid simulations are possible and this opens the door for a vast research activity in different areas.
From the point of views of the numerics, various improvements to the incompressible solver can be done. The method here presented has an overall accuracy of the second order due to how the pressure equation is discretised. Substituting the classic finite differences with the discontinuous Galerkin method would represent a significant gain in accuracy. On the other hand, looking at the performance of the code, including a preconditioner in the iterative method for the pressure equation would speed-up the convergence process with the consequent saving of significant computational time.
The second main area on which future investigations can be carried out is that of the flow physics. The hybrid solver opens the door to very late-time investigation and therefore to studies on self-similarity. RMI is a very complex phenomena which is strongly influenced by the initial conditions and self-similar growth is achieved differently, in terms of time, depending on the perturbation applied to the interface and on the Atwood number. In this thesis, a narrowband of high wavenumber modes with a power spectrum of $1/k$ was considered. For this case, the expansion of the mixing layer is due only through mode coupling and it is not representative of any real case, but is still an interesting case of study. For example, it was found that a perturbation with a power spectrum $\propto 1/k^2$ is representative of the surface finish of an ICF capsule if modes over a broadband combination of wavelengths. This case has a higher growth exponents as the growth of the mixing layer is due to a contribution of mode coupling and growth of the large scales. Moreover, the Atwood number plays a very important role. As reported during the thesis, the growth rate is higher if A_t increases over 0.86 and the self-similar regime is also significantly delayed. Much longer simulations are needed to study the evolution of the instability at high Atwood numbers and standard compressible methods are computationally too expensive to be employed.

References

S. I. Abarzhi. Review of nonlinear dynamics of the unstable fluid interface: conservation laws and group theory. *Phys. Scr.*, T132-014012, 2008.

A. N. Aleshin, E. G. Gamalii, S. G. Zaitsev, E. V. Lazareva, I. G. Lebo, and V. B. Rozanov. Nonlinear and transitional stages in the onset of the Richtmyer-Meshkov instability. *Sov. Tech. Phys. Lett.*, 14:466–488, 1988.

A. S. Almgreen, J. B. Bell, C. A. Rendleman, and M. Zingale. Low Mach number modeling of a type Ia supernovae. I. Hydrodynamics. *Astrophys. J.*, 637:922–936, 2006.

U. Alon, J. Hecht, D. Ofer, and D. Shvarts. Power laws and similarity of Rayleigh-Taylor and Richtmyer-Meshkov mixing fronts at all density ratios. *Phys. Rev. Lett.*, 74:534–537, 1995.

M. J. Andrews. Accurate computation of convective transport in transient two-phase flow. *Int. J. Numer. Methods Fluids*, 21:205–222, 1995.

D. Arnett, J.N. Bahcall, R.P. Kirshner, and S.E. Woosley. Supernova 1987A. *Annual Review of Anstronomy and Astrophysics*, 27:629–700, 1989.

W.E. Arnoldi. The principle of minimized iteration in the solution of the matrix eigenproblem. *Q. Appl. Math.*, 9:17–29, 1951.

A. Bagabir and D. Drikakis. Numerical experiments using high-resolution schemes for unsteady, inviscid, compressible ows. *Comput. Methods Appl. Mech. Eng.*, 193: 4675–4705, 2004.

A. Banerjee and M. J. Andrews. 3D Simulations to investigate initial condition effects on the growth of RayleighTaylor mixing. *Int. J. Heat Mass Transf.*, 52:3906–3917, 2009.

G.I. Barenblatt, G.I. Looss, and D.D. Joseph. *Nonlinear Dynamics and Turbulence.* Pitman Publishing, 1983.

P. Batten, N. Clarke, C. Lambert, and D. M. Causon. On the choice of wave speeds for the HLLC Riemann solver. *SIAM J. Sci. Comp.*, 18:1553–1570, 1997.

R. Beauwens. Interative solution methods. *Appl. Numer. Math.*, 511:437–450, 2004.

J. B. Bell and P. Colella. A second-order projection method for the incompressible Navier-Stokes equations. *J. Comput. Phys.*, 85:275–283, 1989.

J. B. Bell and D. L. Marcus. A second-order projection method for variable-density flows. *J. Comput. Phys.*, 101:334–348, 1992.

M. Brouillette. The Richtmyer-Meshkov instability. *Annu. Rev. Fluid. Mech.*, 34: 445–468, 2002.

R. Castilla and J.M. Redondo. Mixing front growth in RT and RM instabilities. In D.L. Youngs P.F. Linden and S.B. Dalziel, editors, *Proceedings of the 4th International Workshop on the Physics of Compressible Turbulent Mixing*, pages 11–22, Cambridge, United Kingdom, March 1993.

P. R. Chapman and J. W. Jacobs. Experiments on the three-dimensional incompressible Richtmyer-Meshkov instability. *Phys. Fluids*, 18(074101):074101, 2006.

A. J. Chorin. Numerical solution of the Navier-Stokes equations for an incompressible fluid. *Math. Comput.*, 22:745–762, 1968.

A. J. Chorin. On the convergence of discrete approximations to the Navier-Stokes equations. *Math. Comput.*, 23:341–353, 1969.

A. J. Chorin and G. Marsden. *A mathematical introduction to fluid-mechanics*. Springer-Verlag, New York, 1993.

T. T. Clark and Y. Zhou. Growth rate exponents of Richtmyer-Meshkov mixing layers. *J. Appl. Mach.*, 73:461–468, 2006.

B. D. Collins and J. W. Jacobs. PLIF flow visualization and measurement of the Richtmyer-Meshkov instability of an air/SF_6 interface. *J. Fluid Mech.*, 464:113–136, 2002.

D. L. Cotrell and A. W. Cook. Scaling the incompressible Richtmyer-Meshkov instability. *Phys. Fluids*, 19:078105, 2007.

P.A. Davidson. *Turbulence: An Introduction for Scientists and Engineers*. Oxford University Press, USA, first edition, 2004.

G. Dimonte. Nonlinear evolution of the Rayleigh-Taylor and Richtmyer-Meshkov instabilities. *Phys. Plasmas*, 6(5):2009–2015, 1999.

G. Dimonte and M. Schneider. Turbulent Rayleigh-Taylor instability experiments with variable acceleration. *Phis. Rev. E*, 54:3740–3743, 1996.

G. Dimonte and M. Schneider. Density ratio dependence of RayleighTaylor mixing for sustained and impulsive acceleration histories. *Phys. Fluids*, 12(2):304–321, 2000.

G. Dimonte, C.E. Frerking, and M. Schneider. Richtmyer-Meshkov instbility in the turbulent regime. *Phys. Rev. Lett.*, 74:4855–4858, 1995.

P. G. Drazin and W. H. Reid. *Hydrodynamic stability.* Cambridge University Press, New York, 2004.

D. Drikakis. Advances in turbulent flow computations using high-resolution methods. *Prog. Aerosp. Sci.*, 39:405–424, 2003.

D. Drikakis and W. Rider. *High resolution methods for incompressible and low-speed flows.* Springer-Verlag, Berlin, 2004.

D. Drikakis, M. Hahn, A. Mosedale, and B. Thornber. Large eddy simulation using high-resolution and high-order methods. *Phil. Trans. R. Soc. A*, 367(1899):2985–2997, 2009.

W. E and C. W. Shu. A numerical resolution study of high order essentially non-oscillatory schemes applied to incompressible flows. *J. Comput. Phys.*, 110:39–48, 1994.

A. Eberle. Characteristic flux averaging approach to the solution of Euler's equations. Technical Report Lecture Series 1987-04, Von Karman Institute for Fluid Dynamics, 1987.

R. Fletcher. Conjugate gradient methods for indefinite systems. In *Proceedings of the Dundee Biennal Conference on Numerical Analysis 1974*, pages 73–89. G.A. Watson, 1975.

G. Fraley. Rayleigh-Taylor stability for a normal shock wave-density discontinuity interaction. *Phys. Fluids*, 29:376–386, 1986.

R.W. Freund and N.M. Nichitgal. QMR: a quasi-minimal residual method for non-Hermitian linear systems. *Methematics of Computation*, 60:315–339, 1991.

C. Fureby. Towards the use of large eddy simulation in engineering. *Prog. Aerosp. Sci.*, 44:381–396, 2008.

S. Gauthier and M. Bonnet. A k-ε model for turbulent mixing in shock-tube flows induced by Rayleigh-Taylor instbility. *Phys. Fluids A*, 2:1685–1694, 1990.

B.J. Geurts. *Elements of Direct Large-Eddy Simulation.* R.T. Edwards, 2003.

S. K. Godunov. A finite difference method for the computation of discontinuous solutions of the equations of fluid dynamics. *Math. Sb.*, 47:357–393, 1959.

E. Grenier. Oscillatory perturbations of the Navier-Stoke equations. *J. Math. Pures Appl.*, 76:477–498, 1997.

F.F. Grinstein, L.G. Margolin, and W.J. Rider. *Implicit Large Eddy Simulation: Computing Turbulent Flow Dynamics.* Cambridge University Press, 2007.

J. W. Grove, R. L. Holmes, D. H. Sharp, Y. Yang, and Q. Zhang. Quantitative theory of Richtmyer-Meshkov instability. *Phys. Rev. Lett.*, 71:3473–3476, 1993.

H. Guillard and A. Murrone. On the behavior of upwind schemes in the low Mach number limit: II. Godunov type schemes. *Comput. Fluids*, 33(4):655–675, 2004.

H. Guillard and C. Viozat. On the behaviour of upwind schemes in the low Mach number limit. *Comput. Fluids*, 28(1):63–86, 1999.

A. Harten. High resolution schemes for hyperbolic conservation laws. *J. Comput. Phys.*, 49:357–393, 1983.

A. Harten, P. D. Lax, and B. Van Leer. On upstream differencing and Godunov-type schemes for hyperbolic conservation laws. *SIAM Rev.*, 25(1):35–61, 1983.

J. Hecht, U. Alon, and D. Shvarts. Potential flow model of Rayleigh-Taylor and Richtmer-Meshkov bubble fronts. *Phys. Fluids*, 6:4019–4030, 1994.

M.R. Hestenes and E. Stiefel. Methods of conjugate gradients for solving linear systems. *J. Res. Natl. Bur. Stand.*, 49(6):409–436, 1952.

C. Hirsch. *Numerical Computation of Internal and External Flows: Volume 1*. Wiley-Interscience, Burlington, 1988.

R. L. Holmes, G. Dimonte, B. Fryxell, M. L. Gittings, J. W. Grove, M. Schneider, D. H. Sharp, A. L. Velikovich, R. P. Weaver, and Q. Zhang. Richtmyer-Meshkov instability growth; experiment, simulation and theory. *J. Fluid Mech.*, 389:55–79, 1999.

M. J. Huang and A. Leonard. Power-law decay of homogeneous turbulence at low Reynolds numbers. *Phys.Fluids*, 6:3765–3775, 1994.

N.A. Inogamov. The role of Rayleigh-Taylor and Richtmyer-Meshkov Instabilities in Astrophysics: an Introduction. *Astrophyis. Sp. Phys. Rev.*, 10(2):1–335, 1999.

N.A. Inogamov. Richtmyer-Meshkov turbulence. In *Proceedings of the International Workshop on the Physics of Compressible Turbulent Mixing 10*, 2006. Available online at: http://www.iwpctm.org.

J. W. Jacobs and C. E. Niederhaus. PLIF flow visualization of single-and-multi mode incompressible Richtmyer-Meshkov instability. In G.Jourdan and C.Houas Eds., editors, *Proc. of the 6th Intl. Workshop on the Physics ofCompressible Turbulent Mixing*, pages 214–219, Marseille, France, June 1997 1997.

J. W. Jacobs and J. M. Sheeley. Experimental study of incompressible Richtmyer-Meshkov instability. *Phys. Fluids*, 8:405–415, 1996.

M. A. Jones and J. W. Jacobs. A membraneless experiment for the study of Richtmyer-Meshkov instability of a shock-accelerated gas interface. *Phys. Fluids*, 9:3078–3085, 1997.

C.T. Kelly. *Iterative methods for linear and nonlinear equations*. SIAM Frontiers in Applied Mathematics, Philadelphia, 1995.

D.S. Kershaw. The incomplete Choleski-Conjugate Gradient method for the iterative solution of systems of linear equations. *J. Comp. Phys.*, 26(1):43–65, 1978.

K. H. Kim and C. Kim. Accurate, effcient and monotonic numerical methods for multi-dimensional compressible ows Part II: Multi-dimensional limiting process. *J. Comput. Phys.*, 208:570–615, 2005.

R. Klein. Semi-implicit extension of a Godunov-type scheme based on low Mach number asymptotics I: One-dimensional flow. *J. Comput. Phys.*, 121:213–237, 1995.

A.N. Kolmogorov. The local structure of turbulence in an incompressible uid at very high Reynolds numbers. *Dokl. Akad. Nauk. SSSR*, 30:299, 1941.

A. D. Kotelnikov, A. D. Ray, and N. J. Zabusky. Vortex morphologies on reaccelerated interfaces: Visualization, quantification and modeling of one- and two- mode compressible and incompressible environments. *Phys. Fluids*, 12(12):3245–3264, 2000.

R.H. Kraichnan. Inerital reange spectrum of hydromagnetic turbulence. *Phys. Fluids.*, 8:1385–1387, 1965.

H. J. Kull. Theory of the Rayleigh-Taylor instability. *Phys. Rep.*, 5:197–325, 1991.

P. K. Kundu and I. M. Cohen. *Fluid Mechanics*. Academic Press, 2008.

C. Lanczos. Solution of systems of linear equations by minimized iterations. *J. Res. Natl. Bur. Stand.*, 49:33–53, 1952.

P. D. Lax. Weak solutions on nonlinear hyperbolic equations and their numerical computation. *Comm. Pure Appl. Math*, 7:159–193, 1954.

D. Layzer. On the instability of superposed fluids in a gravitational field. *Astrophys. J.*, 122(1):1–12, 1955.

X. L. Li and Q. Zhang. A comparative numerical study of the Richtmyer-Meshkov instability with nonlinear analysis in two and three dimensions. *Phys. Fluids*, 9(10): 3069–3077, 1997.

J. D. Lindl, R. L. McCrory, and E. M. Campbell. Progress toward ignition and burn propagation in inertial confinement fusion. *Phys. Today*, 45:32–40, 1992.

X. D. Liu, S. Osher, and T. Chan. Weighted essentially non-oscillatory schemes. *J. Comput. Phys.*, 115:200–212, 1994.

A. Llor. Invariants of free turbulent decay. 2006. arXiv:physics/0612220v1.

E.N. Lorentz. Deterministic nonperiodic flow. *Journal of Atmospheric Sciences*, 20: 130–141, 1963.

L.G. Margolin and W.J. Rider. A rationale for implicit turbulence moling. *Int. J. Numer. Methods Fluids*, 39(9):821–841, 2002.

G.H. Markstein. A sohock-tube study of flame front-pressure wave interaction. In *6th International Symposium on Combustion*, Reinhold, 1957. 387-398.

J. Mathieu and J. Scott. *An Introduction to Turbulent Flow*. Cambridge University Press, Cambridge, first edition, 2000.

R. Melnikov. Numerical anomalies mimicking physical effects. Technical report, Los Alamos National Laboratory, 1995.

E. E. Meshkov. Instability of the interface of two gases accelerated by a shockwave. *Fluid Dyn.*, 43(5):101–104, 1969.

N. J. Mueschke, W. N. Kraft, M. J. Andrews, and J. W. Jacobs. Numerical investigation of internal vortex structure in two-dimensional, incompressible Richtmyer-Meshkov flows. In *Proceedings ASME 2005 International Mechanical Engineering Congress and Exposition (IMECE2005) Paper no. IMAEC2005-82723*, pages 109–118, Orlando, Novermber 5-11 2005a.

N. J. Mueschke, W. N. Kraft, O. Dibua, M. J. Andrews, and J. W. Jacobs. Numerical investigation of single-mode Richtmyer-Meshkov instability. In *Proceedings ASME International Mechanical Engineering Congress and Exibition (IMECE 2005) Paper no. FEDSM2005-77189*, pages 185–193, Houston, 19-23 June 2005b.

C. E. Niederhaus and J. W. Jacobs. Experimental study of the Richtmyer-Meshkov instability of incompressible fluids. *J. Fluid Mech.*, 485:243–277, 2003.

D. Oron, L. Arazi, D. Kartoon, A. Rikanati, U. Alon, and D. Shvarts. Dimensionality dependence of the Rayleigh-Taylor and Richtmyer-Meshkov instability late-time scaling laws. *Phys. Plasmas*, 8(6):2883–2889, 2001.

S.B. Pope. *Turbulent Flows*. Cambridge University Press, Cambridge, first edition, 2000.

O. Poujade and M. Peybernes. Growth rate of Rayleigh-Taylor turbulent mixing layers with the foliation approach. *Phys. Rev. E*, 81:016316, 2010.

J. D. Ramshaw. Simple model for linear and nonlinear mixing at unstable fluid interfaces with variable acceleration. *Phys. Rev. E*, 58:5834–5840, 1998.

Lord Rayleigh. *Scientific papers II*, page 200. Cambridge University Press, Cambridge, 1900.

J.K. Reid. The use of conjugate gradients for systems of equations possessing Property A. *SIAM J. Numer. Anal.*, 9:325–332, 1972.

O. Reynolds. An experimental investigation of the circumstances which determine whether the motion of water shall be direct or sinuous, and of the law of resistance in parallel channels. *Philos. Trans. R. Soc.*, 174:935–982, 1883.

L.F. Richardson. *Weather Prediction by Numerical Process*. Cambridge University Press, Cambridge, 1922.

R. D. Richtmyer. Taylor instability in shock acceleration of compressible fluids. *Comm. Pure Appl. Math*, 13:297–319, 1960.

P. J. Roache. *Verification and validation in computational science and engineering*. Hermosa Publishers, 1998.

S. Roller and C. D. Munz. A low Mach number scheme based on multi-scale asymptotics. *Comp. Vis. Sci.*, 3:85–91, 2000.

V. V. Rusanov. Calculation of interaction of non-steady shock waves with obstacles. *USSR J. Comput. Math. Phys.*, 1:267–279, 1961.

Y. Saad. *Iterative Methods for Sparse Linear Systems*. PWS Pubblishing Company, Boston, 1996.

Y. Saad and M.H. Schultz. GMRES: A generalized minimal residual algorithm for solving nonsymmetric linear systems. *SIAM J. Sci. Stat. Comp.*, 7(3):856–869, 1986.

P. G. Saffman. Note on decaying of homogeneous turbulence. *Phys. Fluids*, 10:1349, 1967.

P. G. Saffman and D. I. Meiron. Kinetic energy generated by the incompressible Richtmyer -Meshkov instability in a continuously stratified fluid. *Phys. Fluids A*, 1(11): 1797–1771, 1989.

T. Schneider, N. Botta, K. J. Geratz, and R. Klein. Extension of finite volume compressible flow solvers to multi-dimensional, variable density zero Mach number flows. *J. Comput. Phys.*, 155:248–286, 1999.

S. Schnochet. Fast singular limits of hyperbolic PDEs. *J. Differ. Equ.*, 114:476–512, 1994.

J. Sesterhenn, B. Mller, and H. Thomann. On the cancellation problem in calculating compressible low Mach number flows. *J. Comput. Phys.*, 151:597–615, 1999.

E. Shapiro and D. Drikakis. Artificial compressibility, characteristics-based schemes for variable density, incompressible, multi-species flows. Part I. Derivation of different formulations and constant density limit. *J. Comput. Phys.*, 210:584–607, 2005a.

E. Shapiro and D. Drikakis. Artificial compressibility, characteristics-based schemes for variable density, incompressible, multi-species flows. Part II. Multigrid implementation and numerical tests. *J. Comput. Phys.*, 210:608–631, 2005b.

J. Smagorinsky. General circulation experiments with the primitive equations: I. The basic equations. *Mon. Weather Rev.*, 91:99–164, 1963.

P. Sonneveld. CGS, a fast Lanczos-type solver for non-symmetric linear systems. *SIAM J. Sci. Stat. Comp.*, 10:36–52, 1989.

R. J. Spiteri and S. J. Ruuth. A new class of optimal high-order strong-stability-preserving time discretisation methods. *SIAM J. Numer. Anal.*, 40(2):469–491, 2002.

K.R. Sreenivasan. On the universality of the Kolmogorov constant. *Phys Fluids*, 7: 2778–2784, 1995.

G.G. Stokes. On the theories of internal friction of fluids in motion. *Trans. Camb. Philos. Soc.*, 8:287–305, 1845.

G.G. Stokes. On the effect of the internal friction of fluids on the motion of pendulums. *Trans. Camb. Philos. Soc.*, 9:8–106, 1851.

G. I. Taylor. The instability of liquid surfaces when accelerated in a direction perpendicular to their plane. *Proc. Lond. Math. Soc.*, 201(1065):192–196, 1950.

B. Thornber and D. Drikakis. Numerical dissipation of upwind schemes in low Mach flow. *Int. J. Numer. Methods Fluids*, 56:1535–1541, 2008.

B. Thornber, D. Drikakis, R. J. R. Williams, and D. L. Youngs. On entropy generation and dissipation of kinetic energy in high-resolution shock-capturing schemes. *J. Comput. Phys.*, 227:4853–4872, 2008a.

B. Thornber, A. Mosedale, D. Drikakis, D. L. Youngs, and R. J. R. Williams. An improved reconstruction method for compressible flow with low Mach number features. *J. Comput. Phys.*, 227:4873–4894, 2008b.

B. Thornber, D. Drikakis, D. L. Youngs, and R. J. R. Williams. The influence of initial conditions on turbulent mixing due to Richtmer-Meshkov instability. *J. Fluid Mech.*, 654:99–139, 2010.

E. F. Toro. *Riemann Solvers and Numerical Methods for Fluid Dynamics: A Practical Introduction*. Springer, Berlin, third edition, 2009.

E. F. Toro, M. Spruce, and W. Speares. Restoration of the contact surface in the HLL-Riemann solver. *Shock Waves*, 4:25–34, 1994.

E. Turkel, Fiterman A., and Van Leer B. *Preconditioning and the limit of the compressible to the incompressible flow equations for finite differences schemes*. John Wiley and Sons, 1994.

H.A. Van der Vorst. Bi-CGSTAB: A fast and smoothly converging variant of Bi-CG for the solution of nonsymmetric linear systems. *SIAM J. Sci. Comp.*, 13(2):631–644, 1992.

H.A. Van der Vorst. Krylov subspace itaration. *Compu. Sci. Eng.*, 2:32–37, 2000.

B. Van Leer. Towards the ultimate conservative difference scheme. IV. A new approach to numerical convection. *J. Comput. Phys.*, 23:276–299, 1977.

G. Volpe. Performances of compressible flow codes at low Mach number. *AIAA J.*, 31: 49–56, 1993.

D.C. Wilcox. *Turbulence Modeling for CFD*. DCW Industries, La Canada, third edition, 2006.

J. Yang, T. Kubota, and E. E. Zukosky. Application of shock-induced mixing to supersonic combustion. *AIAA J.*, 31(5):854–862, 1993.

D. L. Youngs. Three-dimensional numerical simulation of turbulent mixing by Rayleigh-Taylor instability. *Phys. Fluids A*, 3(5):1312–1320, 1991.

D. L. Youngs. Numerical simulation of mixing by Rayleigh-Taylor and Richtmer-Meshkov instabilities. *Laser Part. Beams*, 12:725–750, 1994.

D. L. Youngs. Effect of initial condition on self-similar turbulent mixing. In *Proceedings of the International Workshop on the Physics of Compressible Turbulent Mixing 9*, 2004. Available online at: http://www.iwpctm.org.

D. L. Youngs. Modelling turbulent mixing by Rayleigh-Taylor instability. *Phys. D*, 37: 270–287, 1989.

D. L. Youngs. Numerical simulation of turbulent mixing by Rayleigh-Taylor instability. *Phys. D*, 12:32–44, 1984.

D. L. Youngs. Application of MILES to Rayleigh-Taylor and Richtmyer-Meshkov mixing. *AIAA*, Paper 2003-4102‘, 2003.

D. L. Youngs and R. J. R. Williams. Turbulent mixing in spherical implosions. *Int. J. Numer. Methods Fluids*, 56:1593–1603, 2007.

S.A. Zehekov, R. McCray, K. Borkowski, and S. Burrows, D. Park. Chandra observations of shock kinematics in supernova remnant 1987A. *Astrophys. J. Lett.*, 628: 127–130, 2005.

Y. Zhou. A scaling analysis of turbulent flows driven by Rayleigh-Taylor and Richtmyer-Meshkov instabilities. *Phys. Fluids*, 13(2):538–543, 2001.

A

Pressure-convergence test

The pressure-convergence test for the incompressible solver is necessary to establish the value of the residual at which the iterative precess of the Poisson-solver can be considered converged. In fact, choosing a too high value of the residual tolerance would lead to a non-converged, and therefore not reliable, solution. On the other hand, a too low value would increase the time necessary for running the simulation without any particular benefit in terms of accuracy of the results. Therefore, a correct choice of the parameter is important. The test case considered is the experiment presented in §4.2. The grid used for the test is G1 in conjunction with M2 and Rusanov flux scheme. Three different simulations were run, keeping exactly the same initial condition and numerical set-up, but the tolerance of the residual was set to: 1.0×10^{-3}, 1.0×10^{-4} and 5.0×10^{-5}. The evaluation of the convergence process is done comparing the values of the velocity components u and v for the three cases at $k\dot{a}_0 t = 25$. In Figure A.2, the values of these two variables along the cells-row $y = 0.02$ are shown and compared.

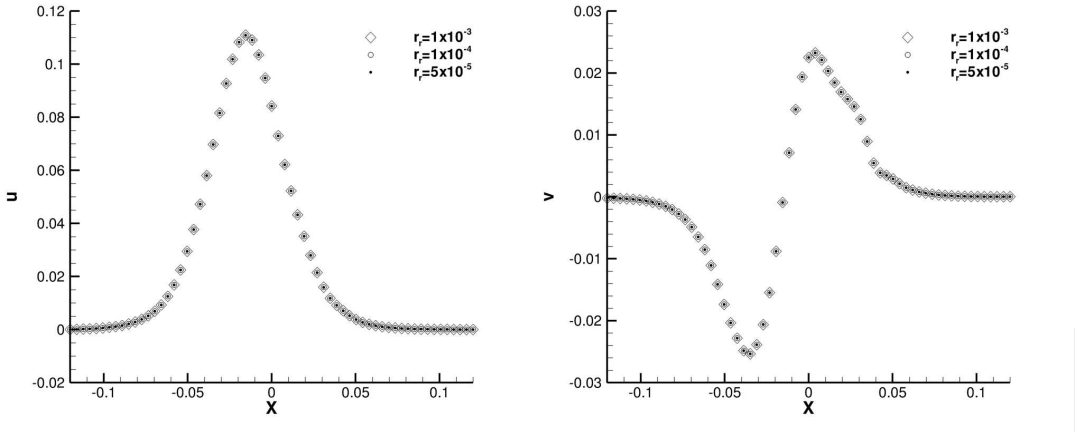

(a) u-velocity (b) v-velocity

FIGURE A.1: Pressure convergence for the velocity components at $t = 0.028$ s and $y = 0.1$.

From the graphs, it is possible to notice that the small dots representing $r_r = 5.0 \times 10^{-5}$ are perfectly centred inside the circles, which represent $r_r = 1.0 \times 10^{-4}$. On the other

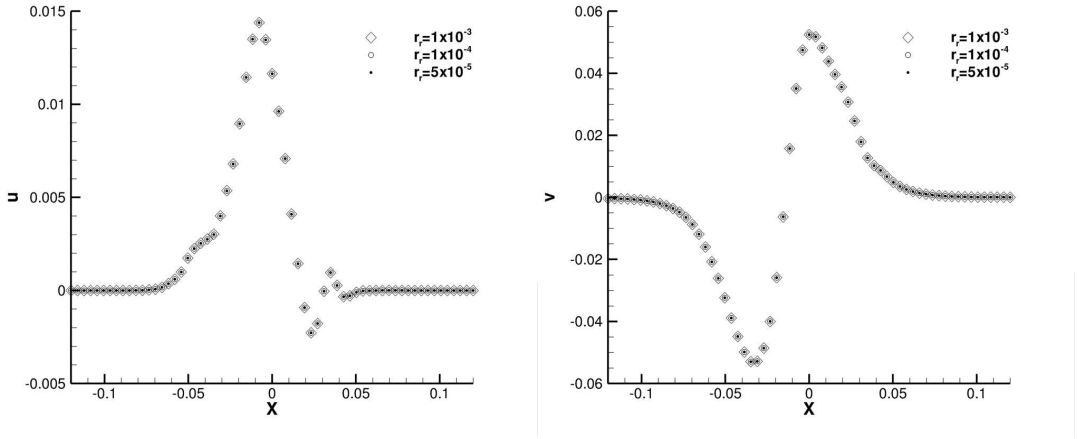

(a) u-velocity (b) y-velocity

FIGURE A.2: Pressure convergence for the velocity components at $t = 0.028$ s and $y = 0.2$.

hand, for $r_r = 1.0 \times 10^{-3}$, a slight off-set of the diamonds with respect to the dots and the circles is present, indicating that the iterative process has not converged yet. The conclusion which is possible to draw from the test, is that the pressure can be considered converged when $r_r = 1.0 \times 10^{-4}$. This is the value which was kept for running all the other simulations.

B

Grid-convergence test

The grid-convergence test of the incompressible solver is based on the Grid-Convergence-Index from the Richardson extrapolation Roache (1998):

$$\mathrm{GCI} = F_s \frac{|\epsilon|}{r^p - 1} \,, \tag{B.1}$$

where, $F_s = 3$, which results in a conservative approach in the estimation of the GCI, is a safety coefficient, $p = 2$ indicates the accuracy of the GCI computation process and $r = 2$ since the grids were created by a doubling process (G2 has the double number of cells along each edge compared to G1 and so on). The computation of the GCI has been done according to the length of the mixing zone a. The test was made for all the reconstruction schemes previously presented: M2, M3, M5, W5 and W9 and the results for each Riemann solver are presented in Tables B.1, B.2 and B.3. Here the GCI associated with the comparisons between G1-G2, G2-G3 and G3-G4 at $k\dot{a}_0 t = 10.0$, 15.0 and 20.0 is reported.
Looking at the values of the GCI, it is possible to notice how, as the grid is refined, the convergence of the grid is achieved. This is valid independently from either the scheme chosen for discretising the fluxes or the reconstruction at the cells interface. In fact, for all the cases, the quality of the results significantly improves between G1 and G2 and very good agreement is present between G3 and G4. The Riemann-solver which gives the best convergence of the grid is the one of Rusanov, where, between G3 and G4, the GCI is always less than 1%.

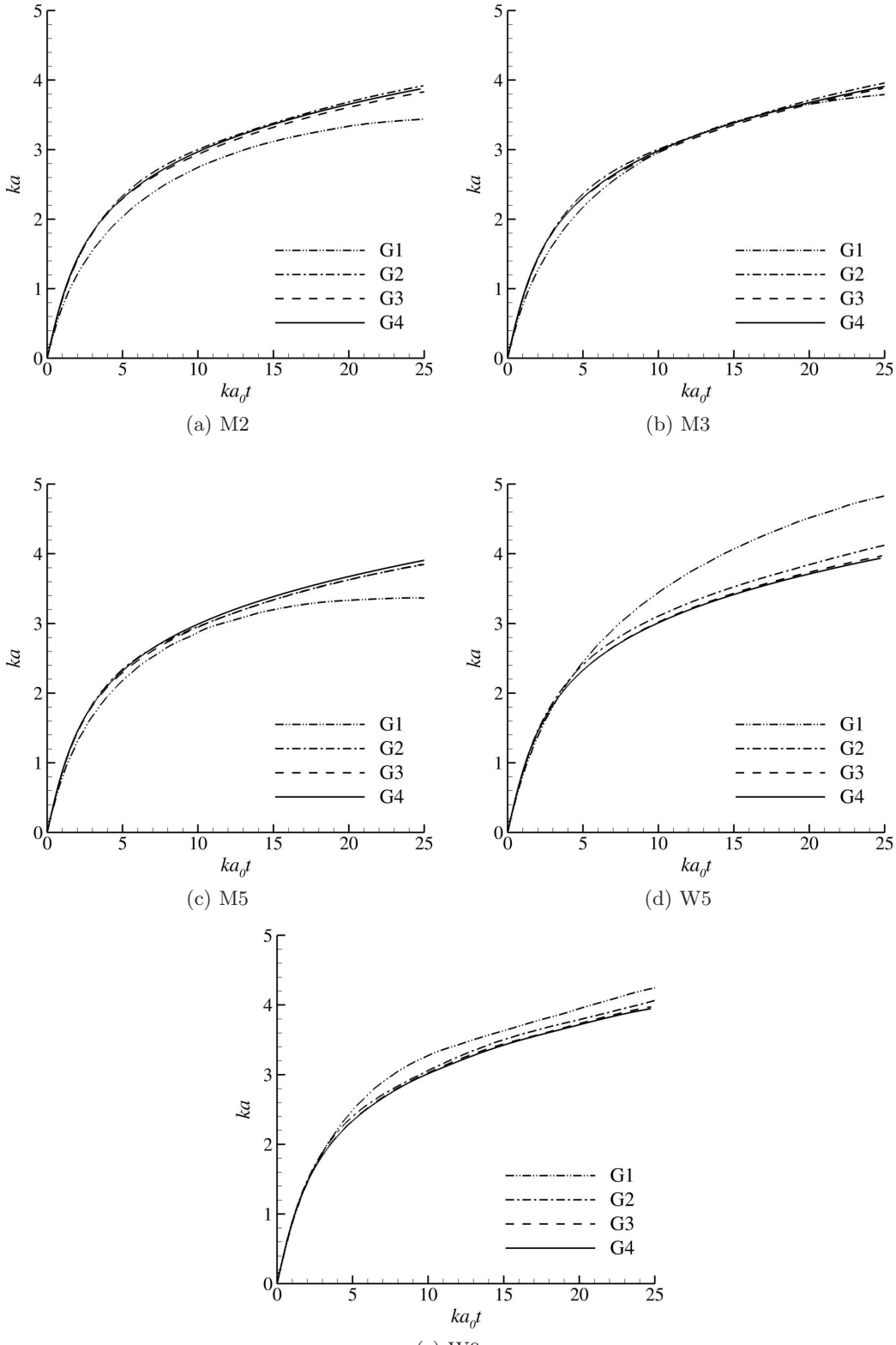

(a) M2 (b) M3

(c) M5 (d) W5

(e) W9

FIGURE B.1: Growth of the instability according to LF flux for grids G1, G2, G3, G4.

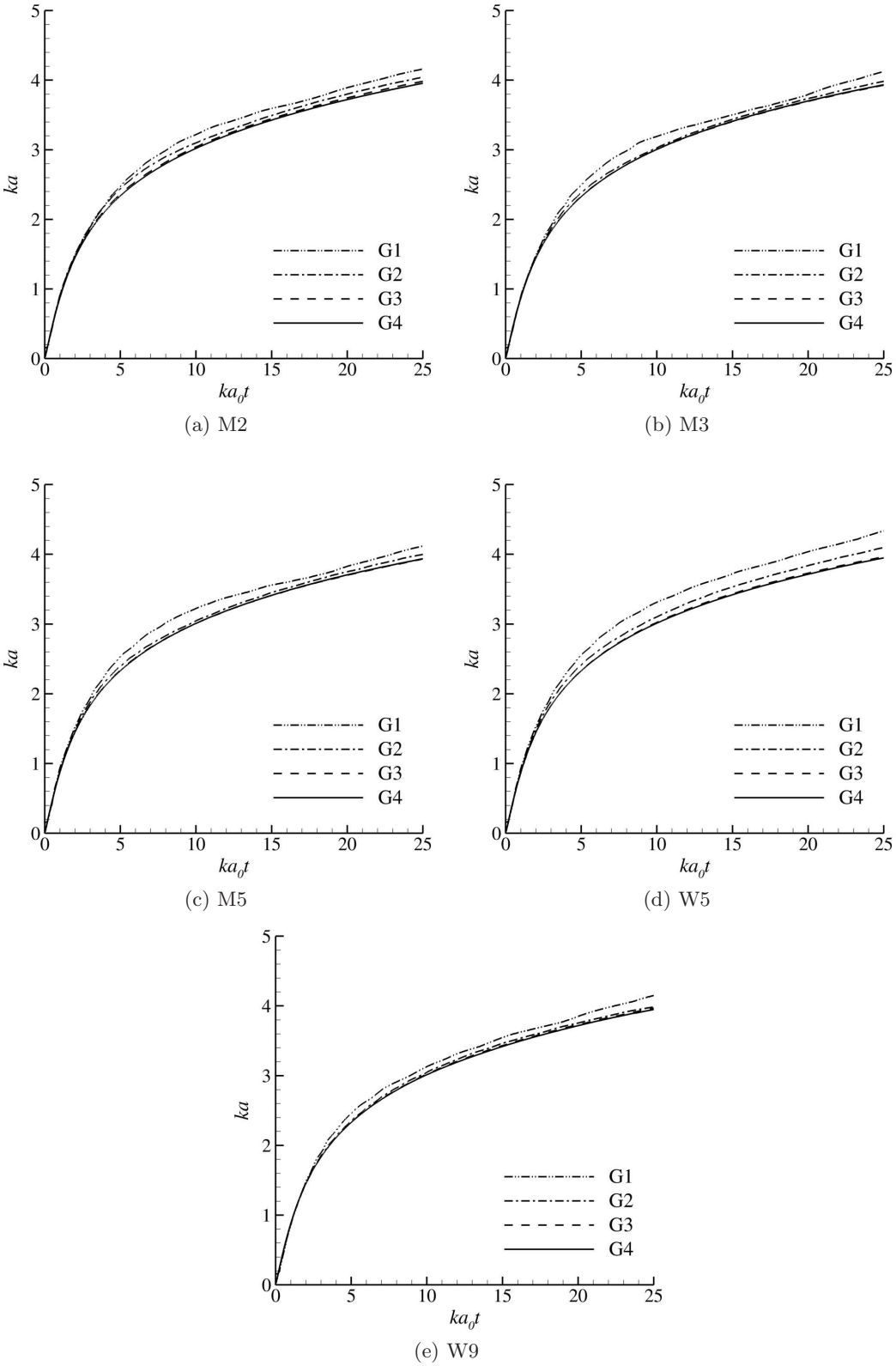

(a) M2 (b) M3

(c) M5 (d) W5

(e) W9

FIGURE B.2: Growth of the instability according to RU flux for grids G1, G2, G3, G4.

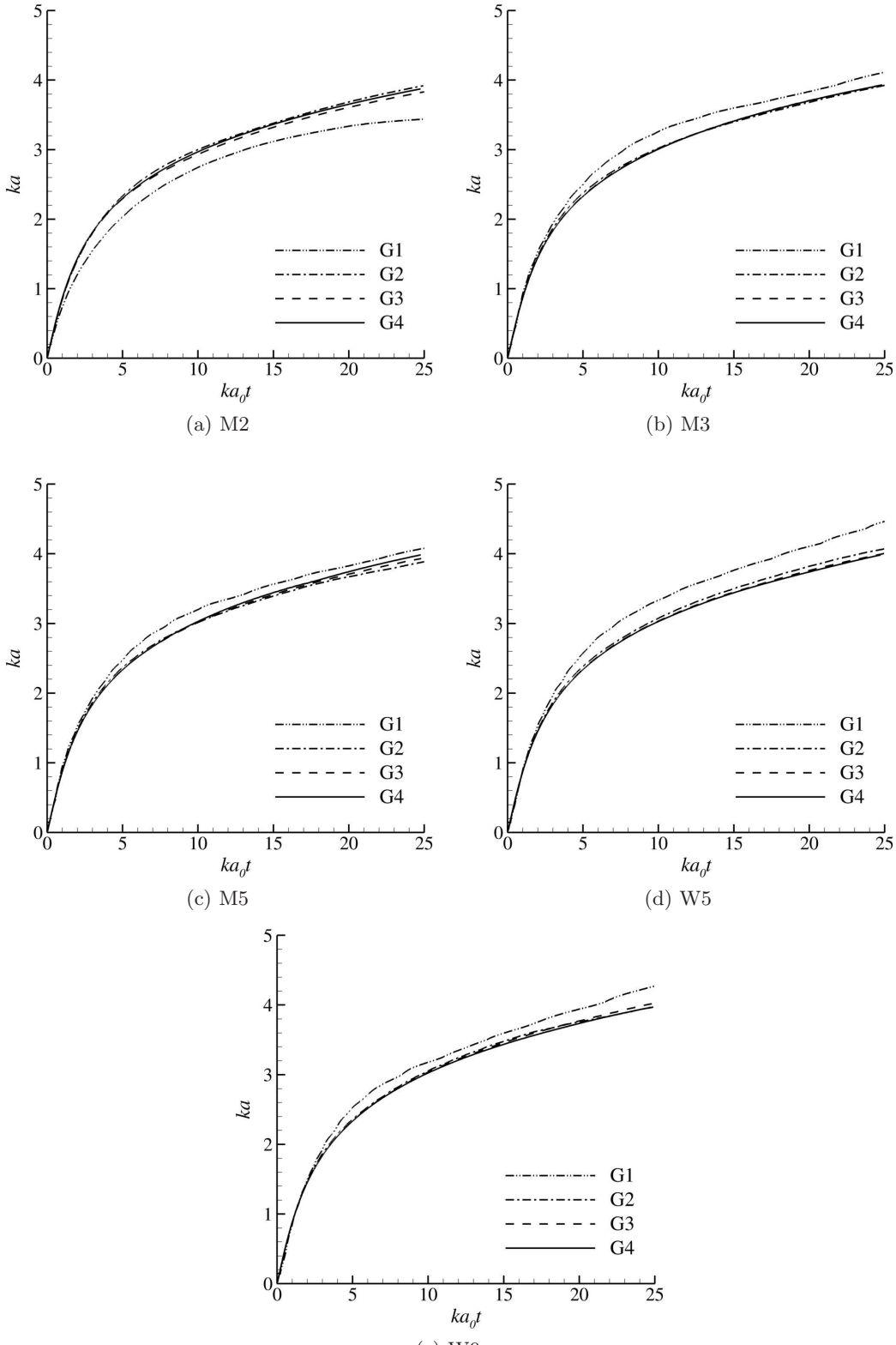

(a) M2 (b) M3

(c) M5 (d) W5

(e) W9

FIGURE B.3: Growth of the instability according to HLL flux for grids G1, G2, G3, G4.

Rec. scheme	Adim. time	GCI [%]		
		G1-G2	G2-G3	G3-G4
M2-VL	10.0	8.53	2.32	1.22
	15.0	7.75	1.77	1.27
	25.0	12.15	2.35	1.32
M3-KK	10.0	1.78	1.55	0.85
	15.0	1.35	0.87	0.78
	25.0	4.10	1.86	0.59
M5-KK	10.0	2.80	1.30	0.48
	15.0	4.22	1.03	0.40
	25.0	12.37	1.16	0.33
W5	10.0	10.92	2.85	0.35
	15.0	15.47	2.68	0.52
	25.0	17.22	3.62	0.78
W9	10.0	7.01	1.05	0.46
	15.0	3.70	1.81	0.46
	25.0	4.55	1.92	0.64

TABLE B.1: Grid Convergence Index for Lax-Friedrichs flux.

Rec. scheme	Adim. time	GCI [%]		
		G1-G2	G2-G3	G3-G4
M2-VL	10.0	2.66	0.93	0.25
	15.0	2.40	0.95	0.38
	25.0	4.10	0.73	0.22
M3-KK	10.0	5.42	0.77	0.01
	15.0	1.86	0.97	0.10
	25.0	3.49	1.39	0.13
M5-KK	10.0	5.79	1.21	0.02
	15.0	3.09	1.18	0.03
	25.0	2.98	1.62	0.05
W5	10.0	6.76	2.65	0.35
	15.0	5.40	2.88	0.25
	25.0	5.84	3.36	0.39
W9	10.0	2.66	0.93	0.25
	15.0	2.40	0.95	0.38
	25.0	4.10	0.73	0.22

TABLE B.2: Grid Convergence Index for Rusanov flux.

Rec. scheme	Adim. time	GCI [%]		
		G1-G2	G2-G3	G3-G4
M2-VL	10.0	8.53	2.32	1.22
	15.0	9.08	1.75	0.36
	25.0	8.24	0.20	0.02
M3-KK	10.0	7.93	1.60	0.20
	15.0	5.88	0.39	0.05
	25.0	4.78	0.35	0.07
M5-KK	10.0	4.68	1.51	0.57
	15.0	5.04	0.80	0.67
	25.0	5.01	1.37	1.12
W5	10.0	8.38	1.34	0.24
	15.0	7.54	1.49	0.23
	25.0	9.55	1.69	0.24
W9	10.0	4.05	0.55	0.45
	15.0	3.41	0.72	0.54
	25.0	7.41	1.30	1.23

TABLE B.3: Grid Convergence Index for HLL flux.